High Test Peroxide Decomposition Modelling in Catalyst Beds

Kapeel Darshana Samarawickrama

Master Thesis
Faculty of Aerospace Engineering
Department of Space Engineering

HIGH TEST PEROXIDE DECOMPOSITION MODELLING IN CATALYST BEDS

by

Kapeel Darshana Samarawickrama

In partial fulfilment of the requirements for the degree of
Master of Science in Aerospace Engineering
at the Delft University of Technology,
to be defended publicly on Wednesday 14th July 2021 at 9:00 AM.

Supervisor:	Ir. B.T.C. Zandbergen	
Thesis committee	Dr. J. Guo	TU Delft
	Ir. B.T.C. Zandbergen	TU Delft
	Ir. R. Noomen	TU Delft
	Ir. V.R. Huisman	Dawn Aerospace

This thesis is confidential and cannot be made public until 14th July 2023

TU Delft Delft University of Technology

CONTENTS

List of Figures

List of Tables

ABBREVIATIONS

HTP High Test Peroxide

NIST National Institute of Standards and Technology

ODE Odinary Differential Equation

PVC Polyvinyl Chloride

CFD Computational Fluid Dynamics

REACH Registration, Evaluation, Authorisation and Restriction of Chemicals

PREFACE

I would like to thank my thesis supervisor Ir. Barry Zandbegern for accepting to supervise an external research topic, for his patience and for continuous feedback over the course of this thesis. I'd like to thank Jian Guo, Ron Noomen, Jian Guo and Ralph Huisman for being a part of the thesis committee. My sincerest appreciate goes out to Dawn Aerospace particularly to Jeroen Wink, Tobias Knop, Robert Werner and Stefan Powell for giving me the opportunity to do a thesis within the company and giving opportunity to translate theoretical knowledge to practice. I am grateful for Dawn Aerospace for facilitating this thesis along with test campaign in which I got the opportunity to make use of the test facility in New Zealand. I would like to thank Stefan Powell for all the guidance and support during the test campaign in New Zealand. Additionally, I would like to thank Iain Finer and Jack Davies who worked on the test setup development. I also want to acknowledge Felix Lindemann, Rob Hermsen, Peter van den Berg for the fruitful discussions we had. Finally I would like to thank my family and friends for always being there for me.

Kapeel Darshana Samarawickrama
Delft, July 2021

SUMMARY

Dawn Aerospace is start up company that is developing a reusable sub-orbital spaceplane. The MK-II rocket powered spaceplane uses High Test Peroxide for its main engine and reaction control system. Catalyst beds are required to decompose High Test Peroxide (HTP) to steam and Oxygen. In order to investigate the decomposition of HTP in a pellet catalyst bed a numerical model was developed which is capable of predicting High Test Peroxide flow decomposition in catalyst beds. Thereby deduce the influence of operating parameters and design choices. The model developed is based on a two phase flow through the catalyst bed that is chemically reacting by undergoing decomposition. The flow is assumed homogeneous, adiabatic and continuous resulting in steady state model outputs. Fast equilibrium adsorption and finite rate desorption of Hydrogen Peroxide on to the catalyst surface is assumed in a single step. The decomposition is modelled using the Arrhenius relations. Additionally, the flow pressure losses are computed using Tallmadge relations (an extended Ergun relation) for two phase flow through packed beds. The model can predict the flow temperature distributions up to 98% reaction advancement. The model was verified by comparing it to existing model results, this showed good agreements in 7 of the 8 cases. The results showed consistently that the model predicted 98% of the decomposition progression is achieved in a shorter catalyst bed length than the catalyst bed lengths in an existing model (4 to 14 % shorter). The flow pressure losses of the models showed deviations compared to the existing models ranging from 5.55% to 12.18%. The differences in the flow temperature and flow pressures are discussed and related to the governing theories of the models.

In order to validate the model, experiments were performed. Catalyst pellets were made in catalysis laboratory of Faculty Applied Sciences in TU Delft. The manufactured catalyst was tested in an experimental setup at Dawn Aerospace's facility in Christchurch, New Zealand. The test data was processed, studied, and sampled for model validation. The test data were used in model validation and a good agreement was found between the test data and the simulated results. The simulated flow temperature and the measured temperature deviated from 0.41% to 1.93% of the adiabatic flow temperature. In all validation cases the model results showed that reaction was completed or exceeded 98% prior to reach L/D 3.09. This finding was further validated with test video footage. The flow pressure simulated was compared to that of the experimental results. The overall pressures showed good agreement with the experimental average, with pressure drop deviations less than 1% of the operating pressure. In all experiment cases the flow distribution predicted was within the measured pressure roughness.

Many simulations were performed and compared to investigate the impact of varying design choices and operational conditions. In all cases the flow development along the

catalyst bed length was assessed. In comparison to the simulations results it was found that an increase of operational parameters such as pressure promoted gas phase decomposition resulting in shorter bed length requirements. In the simulated case the length required for 98% decomposition progression was found to be 16.54 [mm] at 10 bar pressure and 5.69 [mm] at 30 [bar] pressure. Similarly, the influence of feed High Test Peroxide concentration was evaluated and finding showed increasing concentration to shortens the required bed length, with a difference of 3.34 [mm] between 80 % HTP and 100% HTP. The analysis of the simulated conditions showed that the increase of massflow inversely impacts the required catalyst bed length. With a bed loading of 200 $kgs^{-1}m^{-2}$ the required bed length was 11.76 [mm] and a bed length of 5.88 [mm] for a bed loading of 100 [$kgs^{-1}m^{-2}$]. This model serves as tool to identify the operational parameters and their impacts in catalyst beds. The Model outcomes demonstrating the effects of operational parameters and design choices on catalyst bed helps in understanding their interactions and can aid in catalyst bed design and optimisations processes.

LIST OF SYMBOLS

Latin Symbols:

A	Cross-sectional area	$[m^2]$
A_r	Arrhenius pre exponent	$[s^{-1}]$
C	Concentration	$[\,mol\,m^{-3}]$
C_c	Chisholm constant	$[-]$
C_p	Heat capacity	$[J\,mol^{-1}\,K]$
D_p	Pellet diameter	[m]
D_C	Chamber diameter	[m]
E_f	Activation energy	$[J\,mol^{-1}]$
f	Friction factor	$[Pa\,m^{-1}]$
G	mass flux	$[kg\,s^{-1}\,m^{-2}]$
h	Molar enthalpy	$[J\,mol^{-1}]$
$\hat{h}$	Flow species molar enthalpy	$[J\,mol^{-1}]$
h_f	Molar heat of formation	$[J\,mol^{-1}]$
I_{sp}	Specific impulse	[s]
K_1	Equilibrium constant	$[m^3\,mol^{-1}]$
k_a	Rate of adsorption	[-]
k_d	Rate of desorption	[-]
m	Mass	[kg]
$\dot{m}$	Mass flow rate	$[kg\,s^{-1}]$
M	Molar mass	$[kg\,mol^{-1}]$
N	Number of active sites	$[-]$
n	Number of moles	[mol]
n_s	Number data points	[mol]
$\dot{n}$	molar flow rate	$[mol\,s^{-1}]$
P	Pressure	[Pa]
P_s	Saturation pressure	[Pa]
p	Partial pressure	[Pa]
r	Radius	[m]
R	Specific gas constant	$[J\,mol^{-1}\,K^{-1}]$
Re	Reynolds number	[m]
S	Surface area	$[m^2]$
T	Flow temperature	[K]
V	Volume	$[m^3]$
v	Velocity	$[m\,s^{-1}]$
v_s	Superficial Velocity	$[m\,s^{-1}]$
$\dot{v}$	Volumetric flow rate	$[m^3\,s^{-1}]$
VF	Volumetric fraction	$[-]$
X	Mole fraction	$[-]$
x	Axial length	[m]
Y	Concentration as a ratio of weights	$[-]$

Greek Symbols:

β	Reaction Progress	[-]
ΔV	Change in Velocity	[$\mathrm{m\,s^{-1}}$]
ϵ	Evaporation fraction	[−]
ϵ_1	Evaporation fraction of Water	[−]
ϵ_2	Evaporation fraction of Hydrogen Peroxide	[−]
η	Passability in porous media	[m]
κ	Permeability in porous media	[$\mathrm{m^2}$]
μ	Dynamic Viscosity	[Pa s]
ρ	Density	[$\mathrm{kg\,m^{-3}}$]
σ	Deviation	[-]
θ	Relative Occupancy	[-]
Ψ	Two phase multiplier	[-]

Subscripts:

a	Adsorption
ad	Adiabatic
avg	Average
d	Desorption
g	gas
l	Liquid
m	mixture
M	Mass
max	Maximum
r	Reaction
s	Surface
SD	standard Deviation

1

INTRODUCTION

Recent interest in green propellants has paved the way for a revival of the use of concentrated Hydrogen Peroxide also known as High Test Peroxide (HTP) is a top propellant candidate with a long heritage ranging from launcher vehicles to space propulsion systems. This is primarily driven by the quest to replace Hydrazine with alternative propellants. In 2011 the European Commission added Hydrazine to a list of substances of very high concern in the Registration, Evaluation, Authorisation and Restriction of Chemicals (REACH) framework[1]. As a promising green propellant with a heritage in propulsive applications, HTP has been sought after as a cost effective solution. With the growing interest in the industry for green propellants, understanding the behaviour of High Test Peroxide in catalysed decomposition remains important. This holds true more so than ever, with development of novel catalysts.

Dawn Aerospace is a company based in the Netherlands and New Zealand, building the MK-II sub-orbital spaceplane and working on green space propulsion systems for satellites. MK-II is a rocket powered spaceplane that uses a HTP in its bi-propellant main engine and a monopropellant reaction control systems. The MK-II spaceplane main engine is a 2.5 kN bipropellant rocket engine using Hydrogen Peroxide and Kerosene. Prior to combustion of propellants in the engine, Hydrogen Peroxide is required to be decomposed (in a decomposition chamber). The decomposition process requires a catalyst. This process of decomposition has been demonstrated in rocket engines with the use of a heterogeneous catalysts. A heterogeneous catalyst differs in phase to that of the reactants, HTP heterogeneous catalyst is in solid phase. Heterogeneous catalysts such as pellet beds, stacked meshes or monolithic catalyst have an inherent advantage of re-usability unlike a homogeneous catalyst (liquid catalysts that are often consumed/exhausted in decomposition). For decomposition of HTP existing heterogeneous catalysts in form of catalyst beds have shown a wide range in geometries and the operational conditions. The geometry of the catalyst beds and the operational parameters have shown to interact in its performance [2] & [3]. The catalyst bed found in

literature, shows significant variation in basic geometrical parameters such as the catalyst bed length, diameter and operational conditions. Dawn Aerospace would like to investigate into catalytic decomposition of HTP in pellet catalyst bed. Considering the problem case and the academic research, this thesis work is focused on decomposition modelling of Hydrogen Peroxide in pellet catalyst beds. Pellet catalyst beds used for HTP decomposition are typically cylindrical volutes of packed pellets, shown in Figure 1.3. The pellets are made out of thermal resistant materials such as Alumina, with active catalyst material coated on the surface of the pellets.

The study presented in this thesis aims to investigate the advancement of the flow of HTP through catalyst beds along with the impacts on operational variables by means of a model. The results of the simulations are compared with experimental results to assess the accuracy of the model, this is done using a breadboard decomposition chamber developed by Dawn Aerospace. This work aligns well with the needs of Dawn Aerospace in the understanding and modelling of complex flow development of HTP decomposition in catalyst beds. The outcome of this work can be used in numerous aspects including for gaining insight into the flow development in a decomposition chamber, for evaluation of catalyst performance and thereby allocating design choices in the design process of decomposition chambers.

1.1. CATALYST BED

In the work presented in this thesis, the catalyst bed is composed a pellet bed used for decomposing HTP. The decomposition chamber (part of a monopropellant or bipropellant system) houses the catalyst bed inside it, which is typically used in propulsion applications. Some past applications of HTP catalyst beds includes the Mercury Redstone Rocket which consisted of a gas generator that used HTP with silicon carbide pellets with impregnated calcium Permanganate [4]. A representation of the Mercury Redstone Rocket gas generator is shown in Figure 1.1 [5]. Figure 1.2 shows a schematic of the Rocketdyne AR2-3 rocket engine with separate gas generator and decomposition chamber used in Lockheed NF-104A aircrafts [6]. More recent notable developments in the industry using HTP decomposition and heterogeneous catalysts includes a reaction control thruster developed by the Orbital Propulsion Center (in Lampoldshausen)[7] and a reaction control thruster developed by Technology For Innovation (T4I) in Padova, Italy[8].

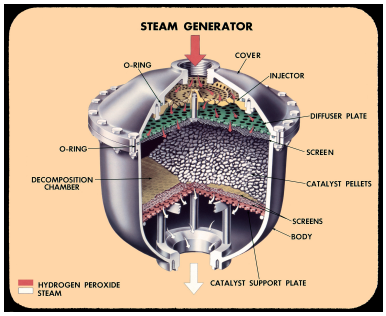

Figure 1.1: Cutaway schematic of the Mercury Redstone Rocket gas generator [5]

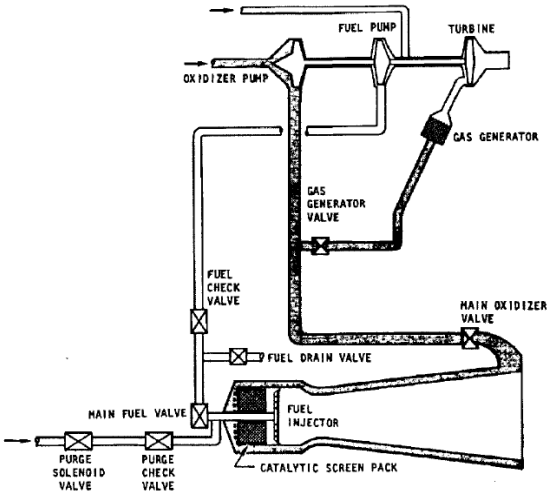

Figure 1.2: Schematic of the AR 2-3 engine depicting catalysts used in the engine cycle [6]

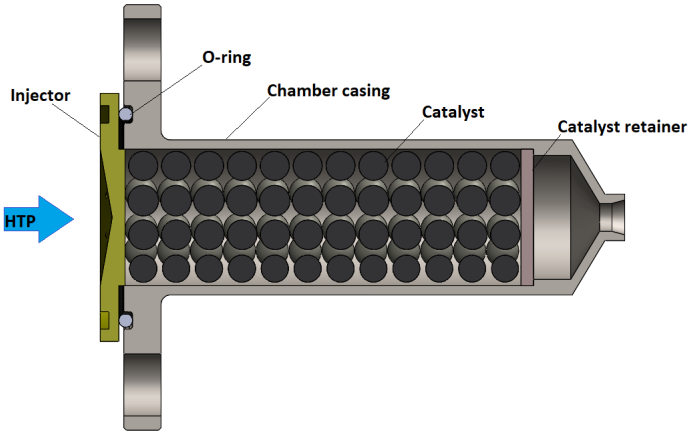

Figure 1.3: Cut out of decomposition chamber with spherical pellet bed developed by Dawn Aerospace

Figure 1.3 shows a decomposition chamber developed by Dawn Aerospace and used in the experimental work in this thesis. First, HTP enters the decomposition chamber via an injector where the Hydrogen Peroxide is distributed into the catalyst bed. As flow passes through the catalyst bed, it reacts with the catalyst to form steam and oxygen. The catalyst bed is held in place using a retainer. Finally the reacted exhaust gases exit the chamber.

In the catalyst bed Hydrogen Peroxide is decomposed to oxygen and steam shown by the following reaction;

$$2H_2O_2 \xrightarrow{\text{catalyst}} 2H_2O + O_2$$

Typical active species of the catalyst of HTP includes Silver, Platinum & Manganese Oxides. Silver catalysts are often used for low concentration HTP applications [9]. Platinum as a catalyst has the capability to withstand very high temperatures, enabling it for applications very high HTP concentration uses (90% +). However, the cost of Platinum is significantly higher, requires sophisticated coating methods and heat treatments. Manganese Oxides have been a versatile choice as catalyst with its ability to operate with low and high HTP concentrations and its low costs. In this work, experiments were performed using a Manganese Oxide catalyst. The simulations were performed with catalyst properties relevant to Manganese Oxides Mn_xO_y. The choice of this catalyst was a primary interest of Dawn Aerospace, due to its low cost and relative straight forward production process and availability of literature on past developments.

The performance of a catalyst bed is evaluated by the ability to decompose Hydrogen Peroxide. The thermal efficiency of a catalyst bed is a measure of the performance of a

catalyst bed, which is the ratio of measured flow temperature to the adiabatic decomposition temperature. The higher the temperature (closer to adiabatic temperature), the greater the level of decomposition that is achieved in the flow. Hence the catalyst bed temperature is the key parameter that is required to analyse the catalyst beds performance. The experiments performed in this thesis includes catalyst bed temperature measurements. However the performance of a catalyst bed can vary depending on concentration of HTP, operating pressure and massflow. In addition to the operational parameters, catalyst beds geometrical parameters such as diameter, length, and the pellet size influences its performance. The challenge is to know the impact of these variables and their interactions which will be addressed in this thesis.

1.2. RESEARCH NEED/MOTIVATION

Development of a catalyst bed for HTP decomposition is complicated due to the interaction of multiple parameters ranging from design choices and operational conditions. The catalyst bed geometry and the operational conditions such as the massflow and operating pressure adds to the complexity of the problem. Hence to develop a decomposition chamber or catalyst bed it requires many experiments to characterise the catalyst performance with respect to the catalyst bed geometry and operational parameters. Works of Pasini et al [10] identified the effects of operational conditions on flow temperature at the end of 6 [cm] catalyst bed. The performance of a catalyst bed is correlated to operational conditions, hence varying the catalyst operational conditions has an impact on the required size of a catalyst bed.

During the literature survey an extensive number of catalyst bed and their operational conditions were analysed, given in Table C.1. Table C.1 shows the varying range of catalyst beds have been developed. In the literature survey, attempts were made to form empirical relations of the geometrical parameters of the catalyst bed (length, diameter, aspect ratio, pellet diameter) to the operating conditions of the catalyst bed. This showed a varying range of conditions and geometries with no clear relations. These finding showed that there is a large design space, making the design choices more challenging.

1

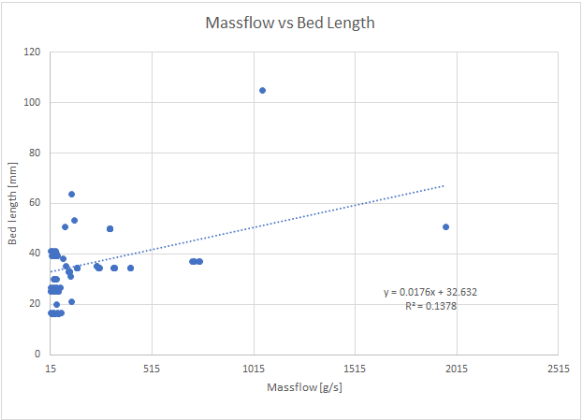

Figure 1.4: Massflow vs lengths of identified catalyst bed designs from TableC.1

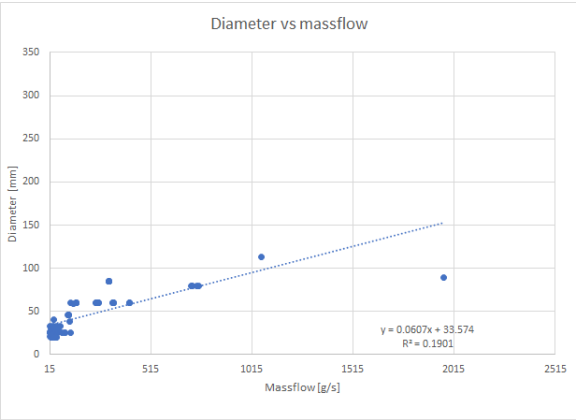

Figure 1.5: Massflow vs diameter of catalyst bed designs from TableC.1

Additionally, the type of catalyst has an impact on the performance. Typically for HTP decomposition, metals or metal oxides are used as a catalyst. With each having its own set of reaction properties, different catalysts react at different rates with HTP. Finally, the concentration of Hydrogen Peroxide used in the feed of the catalyst bed has an impact on the decomposition progress in the catalyst bed.

In the literature survey it was identified that the impact of the design choices and operational conditions on the performance, would require extensive experimental tests. Similar observations were made by Chiapetta et al [11], where past developments required an empirical approach. Runckel et al investigated [12] three decomposition chambers and seven different catalyst bed arrangements in an empirical approach for 98% HTP decomposition. The drawback of this approach include the inability to not know if cor-

rect choices are made, leading to changes in the test subject (catalyst bed) or operating conditions. Numerous tests in an iterative manner are required to evaluate performance and the design choices. If this empirical approach is selected, it would require experiments with different catalyst bed sizes and at various operational conditions before a suitable catalyst bed can be determined. This is a very costly process as test apparatus are required to be developed, tests need to be performed and data to be assessed. In addition to that time and labour are required to develop a test setup, test subjects and perform test campaigns.
This shows the importance of modelling such complicated problems. In a development process, a model helps to reduce cost, improve design choices, speed up the development process and improve performance. A model could be used to gain insight to the inner workings of the catalyst bed and identify the impact of the operational conditions. This would serve as tool to obtain flow development data in the catalysts bed with HTP and would allow one to obtain preliminary sizing dependent on the operative conditions. Such model can be used to understand the flow development in HTP catalyst beds and the impacts of operational conditions.

Previous modelling efforts in HTP decomposition were identified in the literature survey. Chiappetta et al[11] worked on a computational fluid dynamic model for a Silver screen catalyst bed using FLUENT software. An inbuilt function was used to model the pressure in porous media governed by Darcy's law [13]. However, Darcy's law is limited to liquid flow in porous media. The decomposition is modelled (only in liquid phase) using an Arrhenius rate equation with a linearly varying pre-exponent factor with the catalyst bed surface to volume ratio. However, in the model the flow species are modelled as fluids whose density is independent of the pressure and only dependent on temperature. Hence this approach is not able to investigate the impact of pressures on decomposition. Similarly, Corpening et al[14] modelled thermal decomposition using Arrhenius equation on a steady adiabatic flow with conservation of mass and energy. Their work was focused on aft-injection of liquid Hydrogen peroxide to the down stream of hot gases of a catalyst bed and deviates from decomposition in catalyst bed. Zhou & Hitt [15] modelled a one dimensional flow of HTP in a Micro Electro Mechanical Systems (MEMS) scale catalyst bed using Computational Fluid Dynamics (CFD) tool. The model is based on conservation of mass, energy, momentum and species. The model uses the local pressure and temperature of the flow, with this the flow phase for H_2O and H_2O_2 are determined. The H_2O and H_2O_2 were assumed to evaporate at the respective boiling points. The thermal losses were accounted in the model. Zhou & Hitt identified that the activation energy is an important parameter at the temperature at which thermal decomposition is rapid. Their work showed an inverse relation to bed length and mass flux. They identified that the absence of thermal decomposition in the upstream of the catalyst bed caused a deviation between the results from the simulations and the experiments. However, the critical length obtained from the model was not representative of the actual lengths needed for the catalytic bed.

Pasini et al[10] developed a model suitable for predicting the flow conditions in catalyst bed. The model was based on one dimensional axial flow in pellet based catalytic beds. The model is based on Arrhenius equations along with Langmuir Isotherm adsorption

and desorprtion kinetics for decomposition advancement. A steady and adiabatic flow is assumed and the Ergun equation is employed for pressure modelling in pellet based catalytic beds. Ergun equation is suitable for flows with Reynolds number typically below 1000 [16]. This approach yields two ordinary differential equations for reacting flow advancement in catalyst bed and pressure distribution. Pasini et al validated the model with experimental data. The validation was limited to a graphical representation of flow temperature at the downstream of the catalyst bed, within an operation pressure ranging up to 20 bar. Limitations in validation results include the lack of massflow data and accuracy of measured and simulated flow temperature data and their deviations. The model tuning parameters were not given in the works of Pasini et al limiting the scope of reproducing their work. Jung et al [17] replicated the model by Pasini et al model and performed a comparison of the model to their own experimental data. Jung et al states the tuning parameters used for their catalyst, this enables the comparison of the model results to the results of Jung et al in the verification process. Similarly Jung et al validated the simulated data against experimental data to show good agreements. Jung et al measured flow pressure and temperature at three locations of the catalyst bed. However the validity of the model was limited to the comparison of experimental results to the simulated results (only three test data points are shown in comparison figures in their validation process for each validated case). However, Jung et al showed that the approach taken by Pasini et al produce good results, with limited validation. However there is a fundamental deficiency in the modelling approach and that is the assumption that the flow composed of two species to evaporates at a single rate (liquid mixture only has a single evaporation fraction).

Pasini et al's model serves as interest of this thesis work, however some changes to the model were implement, this includes changing the modelling to include two evaporating liquids instead of a single evaporation liquid and changes to the pressure model to account two phase flow. Koopmans & Musker [18] validated a pressure model for flows with Reynolds number > 10^3, the pressure model they utilised was based on the works of Sorokin et al [19] and Tallmadge [20]. Sorokin et al used a two phase flow correlation enabling liquid, gas and two phase flow prediction, along with an extended form of the Ergun equation given by Tallmadge for a flow with high Reynolds number. This approach on pressure drop modelling will be incorporated in the model. Modelling approaches implemented in this work are later described in detail in this in Chapter 2. It was found during the literature survey, that the activity of a catalyst with HTP is strongly dependent on the type and the loading of active phase on the catalyst support. However, with the scope of this research and limitation in catalyst characterisation techniques, reference catalyst activity values for Manganese Oxides catalyst from literature will be used. The catalyst activity values for the model were obtained from works of Jung et al [17] and will be used in this work.

1.3. RESEARCH OBJECTIVE AND QUESTIONS

In the previous section, the problem of catalyst bed development was described. Particularly with lack of findings to support the influence of operational variables such as pressure and massflow on existing HTP catalyst bed geometries. From the literature sur-

vey performed it was identified that there is a need for an improved HTP decomposition model for catalyst beds. The importance of decomposition flow modelling of a catalyst bed is to bring insight about the flow development in the catalyst bed and to evaluate the impacts of variable conditions. Operational parameters such as pressure, massflow and HTP concentration has an influence on the flow development in catalyst beds. Hence it needs to be assessed to know the required bed length to achieve the desired decomposition. Considering these findings, the research objective was formulated below:

Research Objective:
Make recommendations on pellet based catalytic bed length for High Test Peroxide decomposition chambers by means of a High Test Peroxide decomposition model to determine the flow development in the catalyst bed.

The research objective is formulated such that flow development in a catalyst bed can be understood, impact of variables can be assessed and quantified in order realise the geometrical requirements of the catalyst bed. To achieve the research objective, research questions were formulated. The research questions are further sub-divided to more specific questions to be answered in the course of the thesis.

In order to attain the research objective stated above, literature related to catalytic decomposition of high test peroxide is reviewed and the research questions and sub questions are formulated as follows;

- **RQ-1** What are factors that influences the pellet based catalyst bed length required to achieve complete decomposition?

Conditions at which the catalyst bed operates impacts the performance of the catalyst bed, irrespective of the type of catalyst selected. These conditions include operating pressure, massflow and the concentration of Hydrogen Peroxide. These have an impact on how the flow develops in a catalyst bed. Effects of varying pressure as an independent variable shall be simulated with the model and the flow properties will be studied. This will enable the determination of the impact and the quantification of the pressure on the reaction progression in the catalyst bed. Increasing the massflow to the catalyst bed results in increase mass flux, this is also known as bed loading (G). Hence the increase of bed loading will result in changing the flow velocities and the penetration of HTP in the catalyst bed. The model shall be used to vary the bed loading as a single variable and assess the impact on the decomposition progress and catalyst bed length. Changing the HTP concentration results into a change in flow temperature during decomposition. In order to determine the impact of the feed concentration on flow development in the catalyst bed varying flow concentration of HTP shall be evaluated utilising the model. Hence varying these factors will result in a different distribution of decomposition along the catalyst bed. The research question is divided to three sub questions such that impact of these variables can be assessed individually.

- **RQ-1.1** What is the effect of increasing the bed-loading on the catalyst bed length required for complete decomposition?

- **RQ-1.2** What is the effect of changing HTP feed concentration on the catalyst bed length ?

- **RQ-1.3** What is the effect of increasing operating pressure on required catalyst length ?

• **RQ-2** Can the required length of a pellet based catalyst bed be determined by using a model ?

In order to answer the second research question, a model is developed and used to simulate a variation of operating conditions of a catalyst bed. The results were used to gain insight to flow development in catalyst beds. The simulated cases were compared with other existing model results to verify the model. In addition, experiments were performed and the experimental data was used to compare to the simulation results to validate the model. The research question is sub divided to three sub questions such that model result analysis, verification and validation are addressed;

- **RQ-2.1** Can the model represent an actual test case ?

- **RQ-2.2** Can the model predict flow properties along a pellet based catalytic bed?

- **RQ-2.3** Can the model be used for sizing a catalyst bed ?

The figure 1.6 shows how the research questions are addressed in the thesis. Firstly, the model will be development and the simulations will be performed. Secondly, the first research question and the associated sub-question will be researched. Thirdly, research question and its sub questions will be researched along with model verification and validation. Finally the objective will be met based on the outcomes of the first and second research questions, using the results to conclude on the effectiveness of such tool and its advantages and disadvantages.

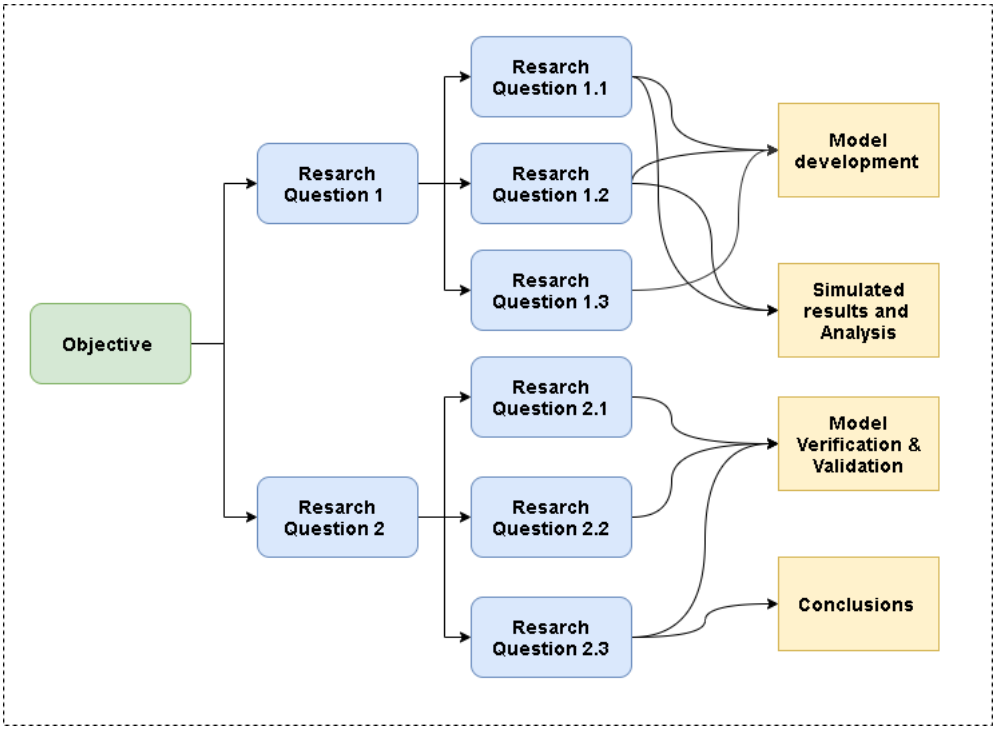

Figure 1.6: Thesis research question overview

1.4. THESIS STRUCTURE

The thesis structure is based on the approach taken to answer the thesis questions. This work consists of eight Chapters. Chapter 2 shows the description and steps taken to develop the model. In Chapter 3 model verification is reported, the results from literature are compared to that simulated by this model. The chapters 4 & 5 describes the experimental setup and the test results obtained are discussed. Test results are compared to the simulated results to validate the model in Chapter 7. The stimulated results on varying operational conditions are discussed in Chapter 7. Finally, the conclusions and recommendations on the work will be given in Chapter 8

2

DECOMPOSITION MODEL

In this chapter model development, implementation and application of the model are described. The purpose of the model is to predict HTP flow development in catalyst bed and investigate the effect of variables in decomposition of HTP in decomposition chamber. From the results of the model, the impact of variables can be known, with better understanding of process it is expected to give insight to the effects of key design parameters of the decomposition chamber. This chapter is divided to five section, where the first three sections are on model development, the fourth section described the implementation of the developed model and the final section describes the application of the model.

In order to bring clarity to the workings of the model and its implementation, the model is divided to two segments. The two branches are known as the $reactionmodel$ and the $pressuremodel$. The reaction model and pressure models interact to complete the modelling process. The reaction model accounts for the chemically decomposing two phase flow of HTP. The reaction model is based on an similar approach to that given by Pasini et al [10] on HTP decomposition modelling used for catalyst reactor parametric design used in thrusters. Some fundamental changes are made in modelling of the flow, as a flow composed of H_2O_2 & H_2O with different saturation properties instead of single evaporating fluid.

The pressure model in the other hand accounts for viscous losses of the flow in catalyst bed. By coupling the reaction model and pressure model the results can be used to unravel the answer to the research questions. The pressure model is based uses the approach given by Sorokin [19], this approach was validated by Koopmans et al [18] in predicting pressure distributions in HTP catalyst bed thrusters.

2.1. REACTION MODEL

The flow species are composed of Hydrogen Peroxide, Water and Oxygen. Depending on the progress of reaction and the respective pressure and temperature the state of the species is determined to be liquid or gas. The flow through out the catalyst bed is treated as homogeneous distributed.

The flow rate is expressed as $\dot{m}$, this is a measure of flowing mass per unit time given in units $\mathrm{kg\,s^{-1}}$. The flow rate can be expressed alternative in terms of moles, then the flow rate is referred to as the molar flow-rate when expressed in moles. The molar flow rate can be derived using the relation 2.1 where n is the number of moles and M is the molar mass of species. The molar flow rate $\dot{n}$ is given in equation 2.2

$$n = \frac{m}{M} \qquad [\mathrm{mol}] \tag{2.1}$$

$$\dot{n} = \frac{\dot{m}}{M} \qquad [\mathrm{mol\,s^{-1}}] \tag{2.2}$$

The HTP flowing into the catalyst bed has a massflow rate given in equation 2.3 and the molar flow rate is given in equation 2.4, they both are expressed in terms of inlet flow composition. Going from equation 2.3 to equation 2.4 the massflow terms of the species is divided with respective molar mass. Note at the inlet conditions, it is assumed that there is only H_2O_2 and H_2O flowing into the catalyst bed.

$$\dot{m} = \dot{m}_{H_2O_2} + \dot{m}_{H_2O} \qquad [\mathrm{kg\,s^{-1}}] \tag{2.3}$$

$$\dot{n} = \dot{n}_{H_2O_2} + \dot{n}_{H_2O} \qquad [\mathrm{mole/s}] \tag{2.4}$$

The concentration of HTP is given with respect to the weight ratio of Hydrogen Peroxide to weight of the solution. The concentration of the solution Y is given in terms of weight of Hydrogen peroxide $W_{H_2O_2}$ and weight of water W_{H_2O} in the solution.

$$Y = \frac{W_{H_2O_2}}{W_{H_2O_2} + W_{H_2O}} \tag{2.5}$$

The initial conditions given by i, this is the condition at which the flow is introduced to the catalytic bed. Hence the initial concentration of the flow can be give in terms $Y(i)$. In order to determine the initial concentration $Y(i)$ it needs to be measured from the solution, in the case of a model this serves as the model input. As the flow progress through the catalytic bed the reaction advances from the starting state 0 to a completed state 1. At the starting state the HTP is flowing in to the catalyst bed (feed), upon entering to the catalyst bed the flow is exposed to catalyst and begins to react. When the reaction

process is completed all Hydrogen peroxide have decomposed to H_2O_2 & O_2. The flow reaction progression or advancement in the catalytic bed will be denoted by β, where β is 0 at inlet and advances to 1 as the reaction is completed.

In the reacting flow, the species molar flow rate can be given in terms of the reaction advancement as follows;

$$\dot{n}(\beta) = \dot{n}(\beta)_{H_2O_2} + \dot{n}(\beta)_{H_2O} + \dot{n}(\beta)_{O_2} \tag{2.6}$$

The initial molar rates $n(i)$ of the flow at the start needs to taken in to account for completeness. Then the molar flow rate for an evolving flow can be given as follows for H_2O_2, H_2O,

$$\dot{n}(\beta)_{H_2O_2} = \dot{n}(i)_{H_2O_2} - \beta \times \dot{n}(i)_{H_2O_2} \tag{2.7}$$

$$\dot{n}(\beta)_{H_2O} = \dot{n}(i)_{H_2O} + \beta \times \dot{n}(i)_{H_2O_2} \tag{2.8}$$

$$\dot{n}(\beta)_{O_2} = \dot{n}(i)_{O_2} + \frac{1}{2}\beta \times \dot{n}(i)_{H_2O_2} \tag{2.9}$$

The initial flow consists of HTP which is composed of H_2O_2 & H_2O hence the molar flow rate of Oxygen at start is 0. Hence, when implementing this in the equation 2.9 can be re-written as follows ;

$$\dot{n}(\beta)_{O_2} = \frac{1}{2}\beta \times \dot{n}(i)_{H_2O_2} \tag{2.10}$$

The inlet molar flow rate (initial condition) at which when HTP is introduced in the decomposition chamber is denoted by $\dot{n}(i)$. At the initial state the concentration of the HTP of the solution is denoted by $Y(i)$. The equations 2.7, 2.8 & 2.10 can be expressed as in terms of the initial concentration and the massflow as follows;

$$\dot{n}(\beta)_{H_2O_2} = \left(1-\beta\right)\frac{Y(i)\dot{m}}{M_{H_2O_2}} \tag{2.11}$$

$$\dot{n}(\beta)_{H_2O} = \frac{(1-Y(i))\dot{m}}{M_{H_2O}} + \left(\beta\right)\frac{Y(i)\dot{m}}{M_{H_2O_2}} \tag{2.12}$$

$$\dot{n}(\beta)_{O_2} = \left(\frac{1}{2}\beta\right)\frac{Y(i)\dot{m}}{M_{H_2O_2}} \tag{2.13}$$

The equations 2.11, 2.12 & 2.13 can be used to determine the molar flow rate at any point of the reaction advancement. Hence the flow species can be established by these equations at any given progression of the reaction (valid for reaction progression ranging from 0 to 1).

2

2.1.1. FLOW PHASE TRANSITION

In order to establish the flow phase transition, the approach taken by Pasini et al by using Daltons law of partial pressure is followed. However some changes to the approach of Pasini et al are implemented in this work by identifying the H_2O and H_2O_2 as two evaporating fluids. Whereas Pasini et al, identified the H_2O and H_2O to evaporate as a single evaporating fluid. In order to determine the state of the species in the catalyst bed, evaporation of the liquid phase needs to be accounted for. The evaporation of the liquids are a consequence of decomposition of Hydrogen Peroxide. As the Hydrogen Peroxide decomposes, the energy released from this exothermic decomposition causes the temperature to increase and the fluids to evaporate. Once the bulk fluid temperature reaches the boiling points of its composed species the fluid begins to undergo phase transition from liquid to gas. This results in a two phase flow composed of liquid and gas. The phase transition is given by evaporation fraction ϵ, where the flow is fully liquid at $\epsilon = 0$ and flow is transformed to gas at $\epsilon = 1$.

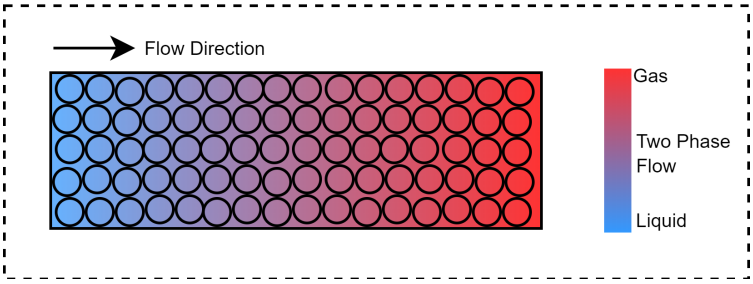

Figure 2.1: Flow transition in a catalytic bed

Using Dalton's law of partial pressure, the pressure P of the gas mixture is denoted using the partial pressure of the composition gases as shown in equation 2.14.

$$p = p_{O_2} + p_{H_2O_2} + p_{H_2O} \tag{2.14}$$

The partial pressure of the gases are given as a product of number of molar fraction of the gas times the pressure of the gas mix. The evaporation fraction ϵ needs to be accounted for the evaporated liquid in the gas mix.

$$p_{O_2} = P \frac{\dot{n_{O_2}}}{\dot{n}_{O_2} + \epsilon(\dot{n}_{H_2O_2} + \dot{n}_{H_2O})} \tag{2.15}$$

In the gaseous H_2O_2 and H_2O partial pressures are denoted as $p_{H_2O_2}$&p_{H_2O} shown in equations 2.16 & 2.17, where $p_s(T)$ is the temperature dependent saturation pressure.

$$p_{H_2O_2} = P_{s-H_2O_2}(t)\frac{\dot{n}_{H_2O_2}}{\dot{n}_{H_2O_2} + \dot{n}_{H_2O}} \tag{2.16}$$

$$p_{H_2O} = P_{s-H_2O}(t)\frac{\dot{n}_{H_2O}}{\dot{n}_{H_2O_2} + \dot{n}_{H_2O}} \tag{2.17}$$

Combining the equations 2.15, 2.16, 2.17 & 2.14 it is possible to express Dalton's law in terms two variables such as temperature and evaporation fractions. The substitutions lead the following ;

$$P = P\frac{\dot{n}_{O_2}}{\dot{n}_{O_2} + \epsilon(\dot{n}_{H_2O_2} + \dot{n}_{H_2O})} + \frac{P_{s-H_2O}(t)\dot{n}_{H_2O} + P_{s-H_2O_2}(t)\dot{n}_{H_2O_2}}{\dot{n}_{H_2O_2} + \dot{n}_{H_2O}} \tag{2.18}$$

$$\left(1 - \frac{\dot{n}_{O_2}}{\dot{n}_{O_2} + \epsilon(\dot{n}_{H_2O_2} + \dot{n}_{H_2O})}\right)P = \frac{p_{s-H_2O}(t)\dot{n}_{H_2O} + p_{s-H_2O_2}(t)\dot{n}_{H_2O_2}}{\dot{n}_{H_2O_2} + \dot{n}_{H_2O}} \tag{2.19}$$

From the right hand side of the equation 2.19 it can be seen that the sum of partial pressure of H_2O & H_2O_2 can be denoted as the pressure due to the vapours of the respective gases and their mole fractions. The vapour pressure is a function of temperature and the local flow composition in the catalytic bed ($p_v(t,\beta)$). The two cases where the evaporation is complete is when $\epsilon = 1$ and at any point the liquid fraction is $1-\epsilon$. The fundamental issue with this approach is that it assumes the liquid mixture composed of Hydrogen Peroxide and water vaporises at the same rate as the reaction progressed. Implementing equation 2.19 and 2.30 as shown by [10] in the model resulted in oscillatory behaviour. The cause for the oscillatory behaviour was solving the energy balance 2.30 along with the partial pressure equation 2.19. The oscillations begin to occur as lowest saturation temperature is met, that is the saturation temperature of water. This results in oscillating evaporation fraction (ϵ) and temperature T. Hence the approach given by Pasini et al [10] was re-evaluated.

By looking at the saturation curves of Hydrogen Peroxide and water in figure 2.2 it can be seen that water vaporises before hydrogen peroxide. This is due to the difference in their saturation pressures. To adjust for this, the approach of using two evaporation fraction was adopted. Hence the flow is assessed as two fluid mediums of H_2O & H_2O_2 with their respective properties.

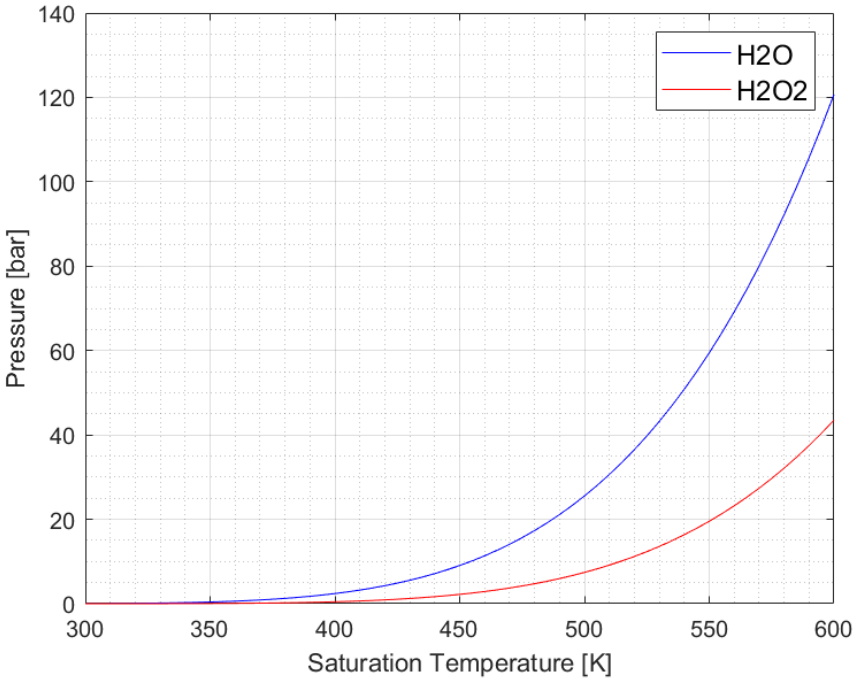

Figure 2.2: Saturation pressure and temperature of Hydrogen Peroxide and water

Pressure $[bar]$	**H_2O Saturation temperature** $[K]$	**H_2O_2 Saturation temperature** $[K]$
10	453.1956	513.0525
30	507.3617	574.0351
60	548.8976	620.7779
100	583.9867	660.2533
130	603.7005	682.4267

Table 2.1: Saturation temperatures of liquid H_2O_2 and H_2O at varying pressures

The evaporation fraction needs to be analysed for the two fluids separately. When modelling the expression 2.19 proved erroneous. Therefore two new expressions were derived using Dalton's law and Raoult's law. Equating the partial pressure of the species to vapour pressure of the species times the mole fraction of the mixture. The fundamental assumption that permits the derivation assumes that the vapour pressure is equal to the saturation pressure, that means the liquid is continuously evaporating at a given temperature to give a certain fraction of vapour.
The two new expression are shown as 2.23 & 2.24 by accounting two evaporating frac-

tions for H_2O & H_2O_2 as ϵ_1 & ϵ_2 respectively. 2.23 & 2.24 are denoted in terms of temperature dependent saturation functions. The saturation functions are obtained by the works of Frolov & Kuznetsov [21], the saturation functions for H_2O & H_2O_2 are given in equations 2.20 and 2.21 with the values tabulated in Table 2.2

$$P_{s_{H_2O}} = \left(\left(\frac{T}{\alpha_{H_2O}}\right)^{1/8} - A_{H_2O}\right)^8 \tag{2.20}$$

$$P_{s_{H_2O_2}} = \left(\left(\frac{T}{\alpha_{H_2O}}\right)^{1/8} - A_{H_2O_2}\right)^8 \tag{2.21}$$

Parameter	Value
A_{H_2O}	12.4575
$A_{H_2O_2}$	12.5302
α_{H_2O}	3.4679×10^{-7}
$\alpha_{H_2O_2}$	3.7642×10^{-7}

Table 2.2: Parameters for saturation conditions of H_2O & H_2O_2

The two evaporation fractions ϵ_1 & ϵ_1 are introduced to denote the evaporation of H_2O & H_2O_2.In order to solve for the evaporation fraction it is assumed that the partial pressure of a species of the flow is equivalent to the saturation pressure times the molar fraction of the species form shown in 2.23 & 2.24. The expressions 2.23 & 2.24 are further simplified 2.25 & 2.26. These equations along with expressions for saturation pressures 2.20 & 2.21 are used to determine the state of the species.

$$\left(1 - \frac{\dot{n}_{O_2}}{\dot{n}_{O_2} + \epsilon_2 \dot{n}_{H_2O_2} + \epsilon_1 \dot{n}_{H_2O}}\right) P = \frac{P_{sH_2O}(t)\dot{n}_{H_2O} + P_{s_{H_2O_2}}(t)\dot{n}_{H_2O_2}}{\dot{n}_{H_2O_2} + \dot{n}_{H_2O}} \tag{2.22}$$

$$\frac{P\epsilon_1 \dot{n}_{H_2O}}{\epsilon_1 \dot{n}_{H_2O} + \epsilon_2 \dot{n}_{H_2O_2} + \dot{n}_{O_2}} = \frac{P_{s_{H_2O}}(T)\dot{n}_{H_2O}}{\dot{n}_{H_2O_2} + \dot{n}_{H_2O}} \tag{2.23}$$

$$\frac{P\epsilon_2 \dot{n}_{H_2O_2}}{\epsilon_1 \dot{n}_{H_2O} + \epsilon_2 \dot{n}_{H_2O_2} + \dot{n}_{O_2}} = \frac{P_{s_{H_2O_2}}(T)\dot{n}_{H_2O_2}}{\dot{n}_{H_2O_2} + \dot{n}_{H_2O}} \tag{2.24}$$

$$\epsilon_1 \left(\frac{\dot{n}_{H_2O_2} + \dot{n}_{H_2O}}{P_{s_{H_2O}}(T)/P} - \dot{n}_{H_2O}\right) = \epsilon_2 \dot{n}_{H_2O_2} + \dot{n}_{O_2} \tag{2.25}$$

$$\epsilon_2 \left(\frac{\dot{n}_{H_2O_2} + \dot{n}_{H_2O}}{P_{s_{H_2O_2}}(T)/P} - \dot{n}_{H_2O_2}\right) = \epsilon_1 \dot{n}_{H_2O} + \dot{n}_{O_2} \tag{2.26}$$

2.1.2. ENTHALPY BALANCE

The enthalpy is denoted by the species, the state of the species and their temperature. The primary assumption that holds the energy balance true, is that the flow is assumed to be adiabatic. The flow is considered adiabatic with negligible viscous losses. The assumption is formulated with adiabatic energy equation as follows;

$$\oint_S \rho h.dS = 0 \tag{2.27}$$

$$\rho v \frac{dh}{dx} = o => h = constant \tag{2.28}$$

The enthalpy balance of the flow can be expressed in terms evaporation fractions (ϵ_1 % ϵ_2) and temperature T where the molar enthalpy of a species is denoted as $\hat{h}$. The enthalpy of each species is given in terms of heat of formation h_f and the product of temperature and specific heat C_p, which is denoted with a subscript H_2O_2, H_2O or O_2 for the respective species. At the inlet to catalyst bed the enthalpy can be calculated for liquid H_2O and H_2O_2 denoted by the subscript i in the enthalpy balance equations 2.30 & 2.31. The enthalpies of H_2O, H_2O_2 and O_2 is given by $\hat{h}$ shown in equation 2.33, 2.34 & 2.35 respectively. The equation 2.30 shows the enthalpy balance for a single evaporation medium, however it was described in section 2.1.1 that the evaporation of two fluid medium needs to be considered.

The energy balance for a unified flow used by Pasini et al is shown in equation 2.30. Implementing evaporating flow of two fluids with distinct evaporating conditions, with the range of $\epsilon = o$ to $\epsilon = 1$ where the flow goes from liquid to gas is given by expression2.31. The left hand side of the enthalpy equation shows the enthalpy at inlet conditions denoted by subscript i of the catalyst bed, the right hands side of the equation can be used to equate the enthalpy at any given point of the flow in the catalyst bed denoted by subscript n.

$$h_i = h_n \tag{2.29}$$

$$\begin{aligned}\left(\dot{n}_{H_2O} \hat{h_{H_2O}} + \dot{n}_{H_2O_2} \hat{h_{H_2O_2}}\right)_i = \left(\dot{n}_{O_2} \hat{h_{O_2}}(t) + \epsilon \left(\dot{n}_{H_2O} \hat{h_{H_2O}}(t) + \dot{n}_{H_2O_2} \hat{h_{H_2O_2}}(t)\right)_g\right)_n + \\ \left((1-\epsilon)\left(\dot{n}_{H_2O} \hat{h_{H_2O}}(t) + \dot{n}_{H_2O_2} \hat{h_{H_2O_2}}(t)\right)_l\right)_n\end{aligned} \tag{2.30}$$

Revised energy balance implement with two evaporation fractions used in of this thesis;

$$\begin{aligned}\left(\dot{n}_{H_2O} \hat{h_{H_2O}} + \dot{n}_{H_2O_2} \hat{h_{H_2O_2}}\right)_i = \left(\dot{n}_{O_2} \hat{h_{O_2}}(t) + \epsilon_1 \left(\dot{n}_{H_2O} \hat{h_{H_2O}}(t)\right)_g + \epsilon_2 \left(\dot{n}_{H_2O_2} \hat{h_{H_2O_2}}(t)\right)_g\right)_n + \\ \left((1-\epsilon_1)\left(\dot{n}_{H_2O} \hat{h_{H_2O}}(t)\right) + (1-\epsilon_2)\left(+\dot{n}_{H_2O_2} \hat{h_{H_2O_2}}(t)\right)_l\right)_n\end{aligned} \tag{2.31}$$

The molar enthalpy in the flow is given by $\hat{h}$

$$\hat{h} = h_f + \Delta h \tag{2.32}$$

The change in enthalpy is denoted by Δh, the internal energy used in the model is the integral form with temperature dependent constant specific heat C_p ,

$$\hat{h_{H_2O}} = h_{f_{H_2O}} + \int_{T_o}^{T} C_{p_{H_2O}}(t)\,dt \qquad [\mathrm{J\,mol^{-1}}] \tag{2.33}$$

$$\hat{h_{H_2O_2}} = h_{f_{H_2O_2}} + \int_{T_o}^{T} C_{p_{H_2O_2}}(t)\,dt \qquad [\mathrm{J\,mol^{-1}}] \tag{2.34}$$

$$\hat{h_{O_2}} = h_{f_{O_2}} + \int_{T_o}^{T} C_{p_{O_2}}(t)\,dt \qquad [\mathrm{J\,mol^{-1}}] \tag{2.35}$$

The heats of formation values are obtained from the Chemistry WebBook database of National Institute of Standards and Technology (NIST) [22]. The heats of formation at standard conditions are used in the models with values as shown in the table 2.3. Note that only required reference heat of formation values are tabulate, liquid oxygen is not considered because the operative conditions does not facilitate the formation of liquid oxygen (only gaseous oxygen).

Species	Heats of formation	Units
H2O (l)	-285.83	$\mathrm{kJ\,mol^{-1}}$
H2O (g)	-241.83	$\mathrm{kJ\,mol^{-1}}$
H2O2 (l)	-193.15	$\mathrm{kJ\,mol^{-1}}$
H2O2 (g)	-136.11	$\mathrm{kJ\,mol^{-1}}$
O2 (g)	0	$\mathrm{kJ\,mol^{-1}}$

Table 2.3: heat of formation values

The specific heat capacities for liquid H_2O and gaseous H_2O_2, O_2 & H_2O_2 are given in polynomial form using the Shomate equation 2.36 [22]. Where t_x is the temperature t in [K] divided by 1000. The coefficients for the respective species are tabulated in tables A.1 to A.5

$$C_p = A + Bt_x + C{t_x}^2 + D{t_x}^3 + \frac{E}{{t_x}^2} \left\{ t_x = \frac{T}{1000} \right. \qquad [\mathrm{J\,mol^{-1}\,K^{-1}}] \tag{2.36}$$

For liquid H_2O_2 the specific heat capacity is obtained using the following form [23];

$$C_p = A + BT + CT^2 + DT^3 \qquad [\mathrm{J\,mol^{-1}\,K^{-1}}] \tag{2.37}$$

The coefficients are tabulated in the appendix in table A.6. With the assumption of ideal gas a constant specific heat is used in solving the energy balance.

The enthalpy balance equation 2.31 is used to identify the fractions of evaporation (gas fractions) as a function of reaction progression β and temperature T. After evaporation is complete (dry out point is reached), the flow is purely gaseous and the enthalpy balance can be solved for the flow temperature with $\epsilon_1 = 1, \epsilon_2 = 1$ and the local flow composition.

2.1.3. VOLUMETRIC FLOW RATE & CONCENTRATION

The volumetric flow rate is the rate at which the volume of a fluids flows through the catalyst bed. The volumetric flow rate can be expressed in liquid volumetric flow rate $\dot{V}_l$ and gaseous volumetric flow rate $\dot{V}_g$ in equations 2.38 & 2.39. The operator that determine volumetric flow between the two phases (gas and liquid) is the evaporation fraction. As the flow evolves through the catalyst bed, the volumetric flow at any point of the reaction can be expressed in terms of the molar flow rates and the density of the species.

$$\dot{V}_l = (1-\epsilon_2)\frac{\dot{n}_{H_2O_2} M_{H_2O_2}}{\rho_{H_2O_2}} + (1-\epsilon_1)\frac{\dot{n}_{H_2O} M_{H_2O}}{\rho_{H_2O}} \qquad [\mathrm{m^3\,s^{-1}}] \tag{2.38}$$

$$\dot{V}_g = \frac{Rt}{p}\left(\dot{n}_{O_2} + \epsilon_1 \dot{n}_{H_2O} + \epsilon_2 \dot{n}_{H_2O_2}\right) \qquad [\mathrm{m^3\,s^{-1}}] \tag{2.39}$$

The volumetric flow for liquid is given in equation 2.38 and the volumetric flow for gas is given in equation 2.39. In order to determine the liquid volumetric flow, the density of liquid H_2O & H_2O_2 are computed at every point in the reaction as a function of temperature using the equations 2.49 & 2.48. Furthermore the volume fraction is defined as the ratio of phase volumetric flow rate to the total volumetric flow rate, shown in 2.40 and 2.41 for gaseous and liquid phases.

$$VF_g = \frac{V_g}{V_l + V_g} \qquad [\mathrm{m^3\,s^{-1}}] \tag{2.40}$$

$$VF_l = \frac{V_l}{V_l + V_g} \qquad [\mathrm{m^3\,s^{-1}}] \tag{2.41}$$

The volumetric flow rate can be used to calculate the superficial velocity of the flow. For liquid and gas the superficial velocities are denoted by v_{s_g} and v_{s_l} in equations 2.42 & 2.43 with A as cross sectional area of the catalyst bed.

$$v_{s_g} = \frac{V_g}{A} \qquad [\mathrm{m\,s^{-1}}] \tag{2.42}$$

$$v_{s_l} = \frac{V_l}{A} \qquad [\mathrm{m\,s^{-1}}] \tag{2.43}$$

The concentration of flow can be expressed in terms of molar flow rate and volumetric flow. The concentration is defined as the number of moles per unit volume, with units $\mathrm{mol\,m^{-3}}$. Concentration of the flow species is denoted by C with the subscript H_2O_2, H_2O & O_2 for the respective flow species which are shown in 2.44, 2.45 & 2.46.

$$C_{H_2O_2} = \frac{\dot{n}_{H_2O_2}}{\dot{V}_l + \dot{V}_g} \qquad [\mathrm{mol\,m^{-3}}] \tag{2.44}$$

$$C_{H_2O} = \frac{\dot{n}_{H_2O}}{\dot{V}_l + \dot{V}_g} \qquad [\mathrm{mol\,m^{-3}}] \tag{2.45}$$

$$C_{O_2} = \frac{\dot{n}_{O_2}}{\dot{V}_l + \dot{V}_g} \qquad [\mathrm{mol\,m^{-3}}] \tag{2.46}$$

2.1.4. FLOW DENSITY AND VISCOSITY

The density of the flow in the catalyst bed is determined by the number of moles of the species, respective molar weight and the volume of the flow. In an evolving flow the density at any given point in the catalyst bed can be denoted in terms of molar flow rate and the volumetric flow, given in the expression 2.47. The molar flow rate of species are functions of the reaction progression (β) given in equations 2.7 to 2.9

$$\rho = \frac{\dot{n}_{H_2O_2} M_{H_2O_2} + \dot{n}_{H_2O} M_{H_2O} + \dot{n}_{O_2} M_{O_2}}{\dot{V}_l + \dot{V}_g} \qquad [\mathrm{kg\,m^{-3}}] \tag{2.47}$$

The density of liquid H_2O_2 and liquid H_2O are given as functions of temperature. The expression for H_2O_2 is given by [24] shown in equation 2.48, where $t_H$is the liquid temperature in [K]

$$\rho_{H_2O_2} = 1579 + 0.0784\,t_w - 0.00197\,{t_H}^2 \qquad [\mathrm{kg\,m^{-3}}] \tag{2.48}$$

The water density is given by Kell formulation [25], where t_w is the liquid temperature in [°C] .

$$\begin{aligned}\rho_{H_2O} = (&999.83952 + 16.945176\,t_w - 7.9870401 \times 10^{-3}\,t_w^2 - 46.170461 \times 10^{-6}\,t_w^3 \\ &-105.56302 \times 10^{-9}\,t_w^4 - 280.54253 \times 10^{-12}\,t_w^5)/\left(1 + 16.897850 \times 10^{-3}\,t_w\right)\end{aligned} \qquad [\mathrm{kg\,m^{-3}}] \tag{2.49}$$

Flow viscosity is an important parameter of the flow characteristics such as the Reynolds number of the flow, which can be used to distinguish the flow type and determine the pressure drop across the catalytic bed. The implementation of viscosity in the pressure drop model is shown in section 2.3. The flow consists of multi species (H_2O_2, H_2O & O_2) and in two states (liquid and gas). Since the available viscosity of Hydrogen peroxide - Water solution are limited to high temperature ranges, individual viscosity of Water and Hydrogen Peroxide are calculated in the model and the blended viscosity of the mix is calculated using a simpler relation given by Bloomfield & Dewan [26] shown in equation 2.50.

The liquid viscosity is calculated by for the different species using following relations ;

$$ln(\mu_{mix_l}) = X_{H_2O_2} ln(\mu_{H_2O_2}) + X_{H_2O} ln(\mu_{H_2O}) \tag{2.50}$$

Where $\mu_{mix(l)}$ is the liquid mixture viscosity, $X_{H_2O_2(l)}$ & $X_{H_2O(l)}$ are the liquid mole fractions of Hydrogen peroxide and Water respectively. The viscosity of the Hydrogen Peroxide is denoted by $\mu_{H_2O_2(l)}$ and the viscosity of the water denoted by $\mu_{H_2O(l)}$. The viscosity functions implemented in the model for liquid species are given for Hydrogen peroxide in equation 2.51 and Water in equation 2.52.

$$\mu_{h_2o_2(l)} = 10^{(A+B/T+CT+DT^2)} \times 10^{-7} \qquad \text{[Pas]} \tag{2.51}$$

The above regression relation is obtained for viscosity of liquid Hydrogen Peroxide valid for temperature range from 273 K to 728 K with the following regression coefficients [23];

- $A = -1.6150$
- $B = 5.0380 \times 10^2$
- $C = 3.5010 \times 10^-4$
- $D = -1.1680 \times 10^-6$

For viscosity of liquid Water is shown in equation 2.52 valid for temperature range from 273 K to 643 K with regression coefficients as follows [27];

$$\mu = A10^{B/(T-C)} \qquad \text{[Pas]} \tag{2.52}$$

- $A = 2.414 \times 10 - 5$
- $B = 247.8$
- $C = 140$

Similarly for gaseous phase of the viscosity of each gas is calculated and then the mixture viscosity is calculated using Graham's viscosity model [28];

$$\mu_{mix_g} = X_{H_2O_g}\mu_{H_2O_g} + X_{H_2O_{2g}}\mu_{H_2O_{2g}} + X_{O_{2g}}\mu_{O_{2g}} \tag{2.53}$$

$X_{H_2O_{2g}}$, $X_{H_2O_g}$ & $X_{O_{2g}}$ are the gaseous mole fractions of Hydrogen peroxide, water and Oxygen. The mole fraction X_i of any given species can be used to denote gas or liquid mole fractions using expressions 2.54 & 2.55.

$$X_g = \epsilon X_i \tag{2.54}$$

$$X_l = (1-\epsilon)X_i \tag{2.55}$$

The viscosity of gaseous Oxygen valid in the temperature range from 150 K to 1500 K is given by equation 2.56 [23].

$$\mu = (A + BT + CT^2) \times 10^{-7} \qquad \text{[Pas]} \tag{2.56}$$

- $A = 44.224$
- $B = 0.562$
- $C = -1.13 \times 10^{-4}$

Viscosity of gaseous Water is given in 2.57 valid for temperature range 150 K to 1500 K [23]

$$\mu = (A + BT + CT^2) \times 10^{-7} \qquad \text{[Pas]} \tag{2.57}$$

The regressive coefficients used for gaseous water;

- $A = -36.826$
- $B = 0.429$
- $C = -1.62 \times 10^{-}5$

Viscosity of gaseous Hydrogen Peroxide is given by equation 2.58 valid for temperature range 373 K to 600 K with ±2% accuracy [29]

$$\mu = (134 + 0.35(T - 373) - 14) \times 10^{-7} \qquad \text{[Pas]} \tag{2.58}$$

The above given relations for viscosity of each species in the flow are implemented in the model. The viscosity relations are used to calculate the viscosity of evolving flow at bulk fluid temperatures. Once the viscosity of species are calculated then they are combined to identify the viscosity of the gas phase and the liquid phase of the flow. The viscosity

values calculated are implemented in the pressure drop model to predict pressure losses in flow through catalytic beds.

2.2. REACTION KINETICS

The reaction model is developed to capture the reaction kinetics in the model. The flow is assumed to have a constant flow rate and the mass flux along the decomposition chamber is constant. The governing theories used in the model is continuity of the flow, defined by the following equation;

$$\oint_s \rho v.dS = 0 \tag{2.59}$$

$$\frac{\rho v}{dx} = o \tag{2.60}$$

Integrating 2.59 yields the following;

$$\rho v = G \equiv constant \tag{2.61}$$

$$v = \frac{G}{\rho} \tag{2.62}$$

The massflow rate is established to be constant in a fixed cross section catalyst bed with a constant mass flux 'G'. The mass flux in catalyst bed is also known as catalyst bed-loading. With a homogeneous feed concentration of HTP, the mixture continuity can be established with flow density density ρ and flow velocity v. The mixture continuity relation can be used with the decomposition chamber cross-sectional area to calculate the mass flux of the decomposition chamber 2.63

$$G = \frac{\dot{m}}{A} \qquad [\mathrm{kg/sm^2}] \tag{2.63}$$

The reaction model follows the approach used by Pasini et al, accounting for fast equilibrium adsorption and first order finite rate desorption for H_2O_2 decomposition on the catalyst surface in one step. The catalytic decomposition process on the surface of a catalyst can be described adsorption and desorption of species on the catalytic surface. This shows that the adsorbed products on to the catalyst surface decomposes and are desorbed. The molecules of H_2O_2 adsorb to the solid catalyst surface with the rate constants of adsorption k_a and similarly desorption takes place with a rate constant k_d. The reaction rate constant is denoted by k_r. For H_2O_2, this process is shown as follows ;

$$H_2O_2 + S \underset{k_d}{\overset{k_a}{\rightleftharpoons}} S{-}H_2O_2 \xrightarrow{k_r} H_2O + \tfrac{1}{2}O_2$$

The adsorption and desorption of H_2O_2 on the catalyst surface is assumed to be in equilibrium, hence the rate of adsorption equals the rate of desorption and it is described by Langmuir isotherm [30] as follows;

$$k_a C_s N(1-\theta) \rightleftharpoons k_d N\theta$$

$$k_a C_s N(1-\theta) = k_d N\theta \tag{2.64}$$

Using Langmuir isotherm it is assumed that the rate adsorption is limited to a single adsorption layer, the surface of the catalyst is homogeneous. In the equation 2.2 C_s is the molar concentration on the surface of the catalyst, N is the number of active sites on the catalyst surface and θ is the relative occupancy/ fractional occupancy (this can be seen as the fraction of the surface covered by has molecules). Solving equation 2.2 for relative occupancy it can be written as follows;

$$\theta = \frac{K_1 C_s}{1 + K_1 C_s} \tag{2.65}$$

The equilibrium constant is given as $K_1 = k_a/k_d$. The equilibrium adsorption and first order rate of desorption can be assumed in one step, this yields that $k_r << k_d$. Hence using expression for relative occupancy 2.65 and the Arrhenius equation, the reaction rate can be expressed as follows ;

$$\dot{r} = k_r N\theta = A_r e^{\left(\frac{-E_r}{RT}\right)} N \frac{K_1 C_s}{1 + K_1 C_s} \tag{2.66}$$

Equation 2.66 can be used to calculate the rate of reaction $\dot{r}$, the term E_r is the activation energy and A_r is the Arrhenius pre-exponent. In the implementation of the Langmuir isotherm, it is assumed that the Hydrogen Peroxide concentration on the catalyst surface is the same as the concentration of the flow at a given point. In the model, rate of reaction needs to be applied to obtain the reaction progress at each step of the flow. Hence the specie continuity expression 2.67 is used. The continuity equation for the flow species can be denoted as follows ;

$$\oint_S C_i v dS = \int_V (u_i'' - u_i')\dot{r} dV => \frac{d(C_i v)}{dx} \equiv v\frac{dC_i}{dx} = (u_i'' - u_i')\dot{r} \tag{2.67}$$

Were u_i'' & u_i' are stoichiometric coefficients of the products and reactants at a point of reaction denoted by subscript i. The change in the flow composition is given by equation 2.68

$$dC = \frac{d\dot{n}_i}{V_l + V_g} = \frac{(u_i'' - u_i')}{V_l + V_g} d\beta \tag{2.68}$$

Hence the evolving flow in a catalyst bed can be expressed in terms of the rate of reaction progress per unit length using 2.67 and 2.68. The equation 2.69 is an Odinary Differential Equation (ODE) with initial value with condition $\beta(0) = 0$, this can be solved to identify the length of the flow catalyst bed with respect to the reaction progress.

$$\frac{d\beta}{dx} = \frac{V_l + V_g}{v} A_r e^{\left(\frac{-E_r}{RT}\right)} N \frac{K_1 C_s}{1 + K_1 C_s} \tag{2.69}$$

The Arrhenius pre-exponent denoted by A_r is proportional to the specific surface a_s (catalyst surface per unit volume). The relation between Arhenius pre exponent and the catalyst specific surface is given equation 2.70 by Jung et al [17]. The specific surface area shown in equation 2.71 [16], this relation was used by Jung et al to allocate the Arrhenius pre-exponent. The void fraction ξ of the catalyst is given by equation 2.83

$$A_r = a_s A_{specific} \tag{2.70}$$

$$a_s = \frac{6(1-\xi)}{D_p} \tag{2.71}$$

2.3. PRESSURE MODEL

In order to predict the pressure variation along the catalyst bed a pressure model is implemented. The pressure model is used to capture the drop in pressure along the catalyst bed due to viscous losses. The pressure model uses the flow properties of the reacting flow in the catalyst bed to predict the pressure losses. The pressure drop model is based on an extended form of Ergun equation which models the pressure drop over porous media. The extended Ergun equation proposed by Tallmadge [20] valid for greater Reynolds range ($0.1 < Re < 10^5$), will be used in this work rather than Ergun equation which is valid for a lower range of Reynolds number ($0.1 < Re < 10^3$) as shown by Tallmadge. Use of the extended Ergun equation in HTP pellet catalyst beds to measure the pressure drop of a two phase flow was demonstrated by Koopmans et al[31] and this approach is used in this work. The friction factor f (also known as Darcy friction factor) for the Ergun equation 2.72 and extended Ergun equation 2.73 are given as follows;

$$f = \frac{150}{N_{Re}} + \frac{7}{4} \tag{2.72}$$

$$f = \frac{150}{N_{Re}} + \frac{4.2}{N_{Re}{}^{1/6}} \tag{2.73}$$

$$N_{Re} = \frac{D_p G}{\mu(1-\xi)} \tag{2.74}$$

Hence the complete extended Ergun equation given by Tallmadge can be written as follows;

$$\frac{\Delta P}{L} = \left(\frac{150}{N_{Re}} + \frac{4.2}{{N_{Re}}^{1/6}}\right)\frac{1-\xi}{(\xi)^3}\frac{G^2}{\rho D_p} \tag{2.75}$$

The pressure drop can be calculated using equation 2.75 for a single phase flow. However in decomposition chamber the HTP flow evolves from liquid at inlet conditions to two phase flow (liquid and gas) and finally a gas phase. Sorokin [19] showed pressure drop calculations of a two phase flow in pebble beds using Lockhart & Martinelli [32] approach which uses of the Chisholm constant [33] to correlate the two phases of the flow. In order determine the pressure drop of the two phase flow the same approach shown by Sorokin is adopted in this work. The pressure drop given by Lockhart & Martinelli [32] gives pressure drop of two phase flow as function of single phase (either gas or liquid) and a two phase parameter Ψ. The relation given by Lockhart & Martinelli for pressure drop in a packed bed is as follows;

$$\frac{\Delta P}{L} = \left(\frac{\Delta P}{L}\right)_{\alpha} {\Psi_{\alpha}}^2 \tag{2.76}$$

In equation 2.76 the term α is the state of the flow (either liquid or gas). The term Ψ is the two phase parameter, this is denoted as a function dependent on Lockhart & Martinelli parameter X. The Lockhart & Martinelli parameter is ratio of the liquid to gas pressure drop.

$$X^2 = \left(\frac{\Delta P}{L}\right)_l / \left(\frac{\Delta P}{L}\right)_g \tag{2.77}$$

The relation for the Lockhart & Martinelli parameter X and the two phase multiplier Ψ for packed bed is related by the Chisholm constant given in equation 2.78 & 2.79 for liquid and gas respectively[33].

$${\Psi_l}^2 = 1 + \frac{C_c}{X} + \frac{1}{X^2} \tag{2.78}$$

$${\Psi_g}^2 = 1 + C_c X + X^2 \tag{2.79}$$

The Chisholm constant given by a ratio of permeability and passability of an homogeneous packed beds was obtained from Sorokin [19]. The Chisholm constant value defines the type of two phase flow in packed a bed. Chisholm constant values and flow types are tabulated in the table A.7.

$$C_c = \left(\frac{\eta\sigma\rho}{\kappa G\mu D_P}\right)^{0.3} \tag{2.80}$$

2

The permeability κ & passability η of a homogeneous bed given by Crone et al [34] to match Ergun equation, in this model κ & η are adapted to match the extended Ergun equation.

$$\kappa = \frac{150}{{D_p}^2}\frac{(1-\xi)^2}{(\xi)^3} \tag{2.81}$$

$$\eta = \frac{4.2}{{D_p}^{\frac{7}{6}}}\frac{(1-\xi)^{\frac{7}{6}}}{(\xi)^3} \tag{2.82}$$

The permeability and the passability of the catalyst bed is dependent on two characteristics of the catalyst bed, these are thew size of the pellets which is a function of the pellet diameter D_p and the void fraction ξ of the catalyst bed. The void fraction of the bed is the free volume available for the flow. The void fraction is strongly dependent on the size and shape of the pellets used and the internal diameter of the decomposition chamber. The average void fraction in packed bed can be approximated by the relation 2.83 given by Bey & Eigenberger [35] as a function of chamber diameter D_c and pellet diameter D_p

$$\xi = 0.375 + 0.34\frac{D_p}{D_c} \tag{2.83}$$

The relation for void fraction given by equation 2.83 is strictly for spherical pellets.

2.4. MODEL IMPLEMENTATION

The model was implemented using Matlab (version R2018a). The model implemented is depicted with a simulation flow diagram 2.4. This gives s schematic overview of the simulation process performed and the interaction of key parameters in the model. First the condition are established in the model, these include operating parameters (pressure and massflow) and inlet conditions of HTP to the catalyst bed (concentration & feed temperature). The equations of the reaction model and the pressure model were implemented in an iterative manner to find solutions for local pressure, temperature and concentration of the flow. The flow moves in the direction from injector to the end of the catalyst bed as depicted in figure 2.1, this is modelled until the catalytic reaction is complete. A single model iteration, is a point of the reaction where the resulting temperature is identified along with development of the species and their respective states. Afterwards the pressure losses are calculated. In order to do this the model is discretized to elements going from start of the reaction to end of reaction. This is know as reaction progression parameter or the reaction advancement parameter β, the application of β is shown in equations 2.6 to 2.13. The model is discretized linearly with reaction progression from 0 to 1. By using trial and error, the discretization to 100 elements was selected

on the basis of time required for computation and the accuracy of the model results. The figure 2.3 depicts the reaction along the catalyst bed, it was found at higher levels of discretization the bend length required is higher to achieve 100% decomposition. However in order achieve 98% decomposition progress the required bed length converge to a single value irrespective of the discretization, which is shown in table 2.4. When the model is discretized with smaller windows (higher numbers) the impact of HTP concentration and the rate of reaction causes the required bed length for decomposition to be higher. In case of infinitely large discretization, means i the reacting flow as number of moles of H_2O_2 approaches 0 the catalyst bed length would be infinitely long. Hence considering a 98% reaction progress is sufficient as the error is 0.15% and the time taken per simulation to generate flow conditions, a level 100 discretization was considered sufficient.

Discretizations	**Time**	**Length at 98% β**	**Length at 100% β [mm]**
100	17.63 [mins]	32.75	41.93
1000	146.39 [mins]	32.79	55.73
10000	70.72 [hrs]	32.80	69.6

Table 2.4: Model results dependent on discretization

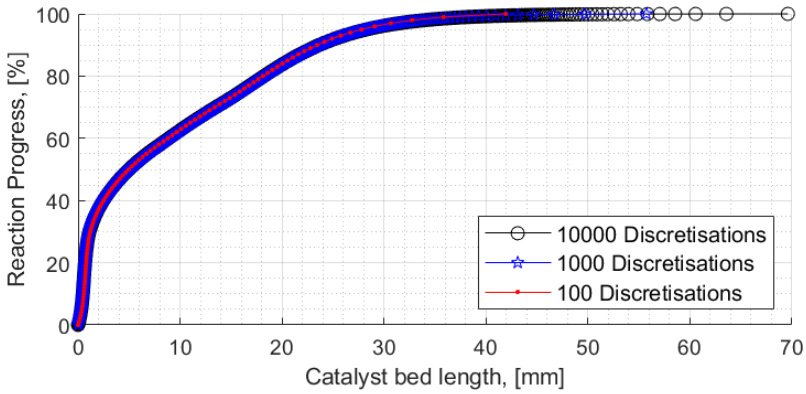

Figure 2.3: Reaction progression along the catalyst bed length and impact of discretization

At the start of the model, the inlet conditions are defined. These inlet conditions includes concentration of HTP used, temperature of the inlet flow, inlet pressure and the massflow rate. First the reaction in the catalyst bed is modelled as a product of molar flow rate and the variation of the molar flow rate is given with equations 2.12, 2.13, & 2.11. Once the molar flow rate is established, then the state of the flow is identified this is done with coupling equations 2.25 & 2.26 with the enthalpy balance equation 2.31. The flow in the catalyst bed is dissected to multiple cases as follows;

1. Pre-boiling region (from inlet till saturation conditions are met)

2. Water boiling region (Where saturation conditions of H_2O are met)

3. Hydrogen Peroxide evaporation region (Where saturation conditions of H_2O_2 are met)

4. Complete gas phase region

In the pre-boiling region equations 2.25 & 2.26 are solved to identify the evaporation fractions of Hydrogen Peroxide and Water. The evaporation fractions are used to calculate the temperature. The iterative process continues till the saturation conditions of Water is met. When the water saturation conditions are met, the newly evolving H_2O from the reaction is assumed to evolve as gas. A fraction of gaseous molar flow rate of H_2O evolved can be determined using β as level of discretization, given in the equation below;

$$\dot{n}_{H_2O_g}(\beta) = \dot{n}_{H_2O_l}(\beta) - \dot{n}_{H_2O_l}(\beta - 1)$$

$$\epsilon_2 \left(\frac{\dot{n}_{H_2O_2} + \dot{n}_{H_2O_l}}{P_{s_{H_2O_2}}(T)/P} - \dot{n}_{H_2O_2} \right) = \epsilon_1 \dot{n}_{H_2O_l} + \dot{n}_{O_2} + \dot{n}_{H_2O_g} \tag{2.84}$$

In the water boiling region the equation 2.26 is rewritten as equation 2.84. Then equation 2.84 is solved with Enthalpy balance to identify the evaporation fractions. Once the evaporation fraction of H_2O reaches 1 then the boiling of water is determined complete. Then the vaporisation process of H_2O_2 is left, in this phase the equation 2.26 is solved with the enthalpy balance with condition $\epsilon_1 = 1$, the equations are solved for the evaporation fraction and the temperature. Once all the H_2O_2 is evaporated ($\epsilon_2 = 1$), then the enthalpy balance can be solved strictly in gas phase to identify the flow temperature.
With each iteration the reaction advances, depending on the flow conditions, the temperature and state (gas/liquid fractions) of the flow species are identified. With these known parameters properties of the flow can be determined, these include the heat capacities 2.36 & 2.37, volumetric flow 2.38 & 2.39 and flow densities are calculated. Using the volumetric flux the concentration of the flow is computed using the volumetric flow rate and equations 2.45, 2.44 & 2.46. At this stage the differential equation 2.66 can be solved to identify the axial position (x) of the catalyst pack with respect to the reaction progression, this is done by numerically integrating the ODE. The solution results in a reaction distribution along the catalyst bed which then can be used to determine the characteristics of the flow (such as species, their state and temperature).

The properties of the evolving flow calculated in the reaction model are used in the pressure model to determine the pressure distribution. The pressure model is implemented to identify the pressure distribution along the catalyst bed. The pressure model first determines if the flow is liquid, gas or both (two phase). Depending on the state of the flow appropriate equations are implemented, for a single phase equation 2.75 is implemented. Pressure drop due to the gas only flow and liquid only flow are computed using

equation 2.75, this is used to determine the two phase multiplier. For the extended Ergun equation to be used, flow properties from the reaction model are required. These include the volumetric flux, superficial velocities and the flow viscosity, with these properties the flow characteristics such as the Reynolds number are identified. However for the two phase flow, equation 2.76 to 2.82 are implemented. Lockhart & Martinelli parameter is determined by using the relation given in equation 2.77. Then the flow permeability and passability are determined with equation 2.81 & 2.82. These two parameters are then used in the equation 2.80 to compute Chisholm constant, the type of flow is determined by using the Chisholm constant. Then the two phase multiplier is calculated using the Chisholm constant and the Lockhart & Martinelli parameter, afterwards the pressure distribution can be calculated using the two phase pressure relation 2.76. The extended Ergun equation used in the pressure model is an ODE with initial condition $P(0) = P_i$. In order to solve for the pressure distribution the equations are numerically integrated over the bounds of the axial position obtained from the reaction model.

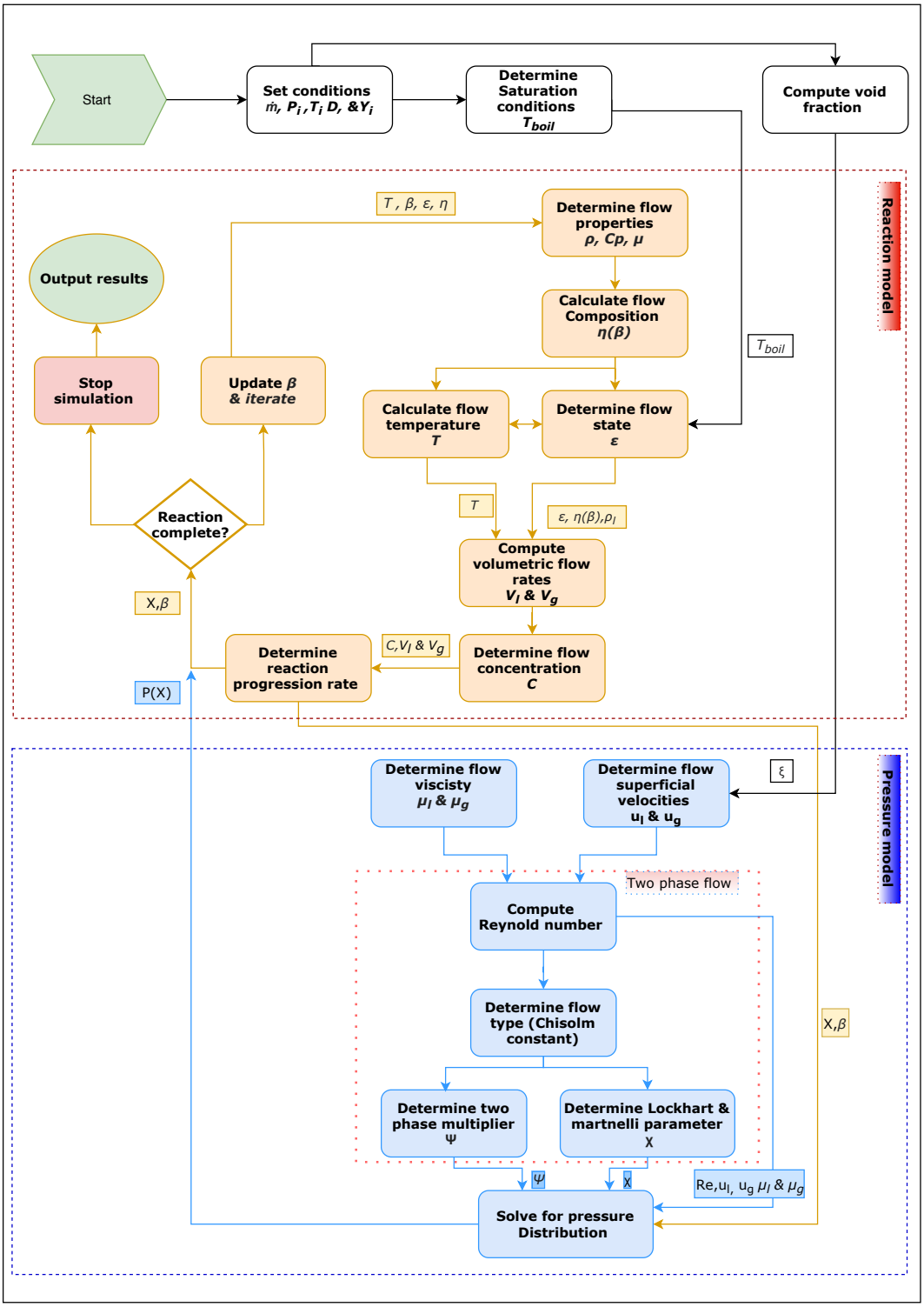

Figure 2.4: Model flow diagram

2.5. MODEL APPLICATION

The purpose of this model is to predict the HTP flow development through the catalyst bed and thereby determine the required catalyst bed length. However the application of the model is not limited to determining flow development or catalyst bed length, it can serve as essential tool or a step in design process of catalyst bed. The model results are described in chapter 7, this shows the capability of the model to simulate results for input variables and capture the impact on these variables and their interactions. This enables to generate estimates for catalyst bed sizing and the operating conditions. In the literature survey a design process for catalyst bed was developed depicted in figure C.3. This design process was developed to give a rational approach in designing a catalyst bed by considering the limiting factors understood during the literature survey. During this thesis the design process was evaluated in order to apply the model in the process, shown in Figure 2.5. Applying the model can help to translate the requirements to finalising catalyst bed sizing parameters or operational parameters. This enables to realise the design space by considering limiting factors and showing interactions between choices of the model input parameters.

The first step to establish the operational needs, given by the requirements of the catalyst bed. Parameters derived from the requirements may include HTP concentration, massflow, operating pressures, type of catalyst and the catalyst bed diameter. These are primary driving requirements of the design space, as far as catalyst bed functionality is concerned. In the first segment of the process model inputs from requirements are identified.The second segment of the process is defined by the model. The model translate the input to outputs, which can be used to distinguish whether the requirements are feasible with selected initial parameters. Some of the model outputs include the flow properties such as temperatures, species and velocities, required catalyst bed length and the pressure drop. If the requirements are met then the model outputs can be used to finalise catalyst sizing or operational variables. However in case where model outputs cannot satisfy the requirements, then the requirements need to be iterated till the feasible design space is realised. An example of this case would be, if the model output pressure drop over catalyst bed is too high, then appropriate requirements contributing to this effect shall be reiterated, until a desirable outcome is realised.

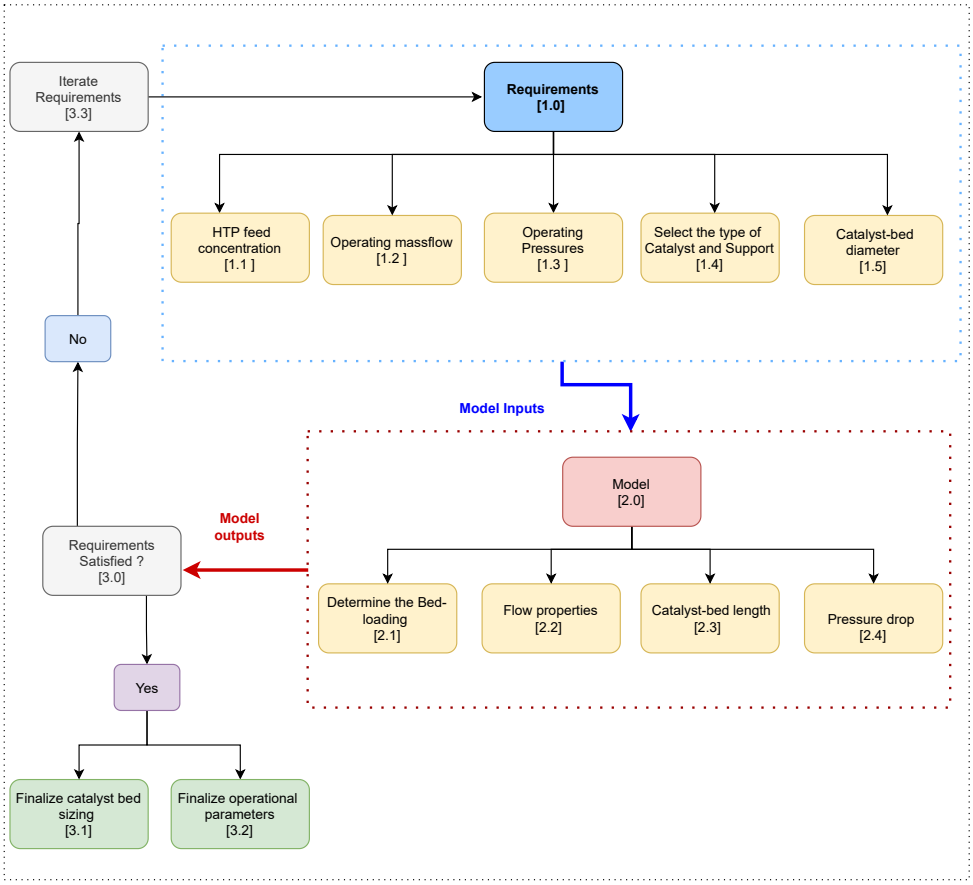

Figure 2.5: Design process showing the steps need to be taken to size a catalyst-bed

This model can be used as a tool to gain insight to how the flow develops in catalyst bed. This enables understanding to how a given type of catalyst or operating conditions have an impact on the flow properties along the catalyst bed. With the flow development known, the required catalyst bed length is identified. The model can be used to predict flow properties such as temperature distribution along the catalyst bed and pressure drop that can be used for performance optimisation. In addition to the design process the model has multiple applications, and some of the key applications of the model include any process that required modelling of HTP decomposition. Such processes in propulsion may include mono propellant thrusters, bi propellant thrusters or gas generators for turbines. However some other industries that the model or some aspects of the model such as reacting flow through catalytic pellet beds can be used may include chemical and nuclear industries.

3

MODEL VERIFICATION

In this chapter the model is verified with existing models. First, results from Pasini et al are reproduced by simulating their input conditions using the developed model. Model tuning was performed to match results to that of Pasini et al. Due to the limitation of the data, only a graphical comparison was performed. However this enables to demonstrate that the model functions as intended. Jung et al reproduced works of Pasini et al and validated it with their own experiments, the simulation results of Jung et al are used to verify the model developed. Comparisons are performed to quantify the differences between model results of Jung et al and with the implemented changes in this model.

3.1. MODEL COMPARISON

First the model results were generated to match the given case in works of Pasini et al. The purpose of this is to demonstrate that the model functions as expected and capable of demonstrating the expected trends. However some input parameters were first needed to be determined, this enables to match the model data generated with relevant catalytic parameters for the kinetics of the model. Once the relevant parameters are obtained a simulation case was performed in the developed model. The parameters implemented in the first simulation run are summarised in table 3.2. Here on 'case 3' refers to the simulation performed with input criteria summarised in table 3.2.

Tuning level	**K_1**	**a_{s}**	**{A_f} * {N_s}**
1	0.001	6.1367e+03	4.0870e+04
2	0.0001	6.1367e+03	2.9444e+05
3	0.00001	6.1367e+03	2.8253e+06
4	0.000001	6.1367e+03	2.8167e+07

Table 3.1: Tuning Parameters

In order to perform a comparative graphical analysis with the case 3 model results and the results of Pasini et al, the reaction progression, temperature and pressure distribution were plotted. The original graphical results by Pasini et al used in this analysis are given in the Appendix in Figures B.3, B.4 & B.5. The Figures B.3, B.4 & B.5 were digitised using WebPlotDigitizer [36]. Due to scaling of the given figures and large data points and overlapping of data points in Figures B.3, B.4 & B.5, exact data points could not be determined, instead a single data point can only be read as a range. For instance at catalyst bed length 20 mm the temperature range is from 415 [K] to 536[K] can be read from the digitised data. The entire data range was captured for reaction progression, temperature and pressure distribution. The digitised data were then plotted with the model data for a graphical analysis, shown in Figures 3.4, 3.6 & 3.7. It can be seen that this model results have been propagated till the reaction is complete, however data from Pasini et al is only available until a bed length of 60 [mm].

3.1.1. TUNING

Since the model tuning parameters used by Pasini et al were not given in their work, except for the activation energy, numerous tuning parameters were evaluated. The simulations were checked for varying adsorption equilibrium constant from 0.01 to 0.000001 and maintaining the required Arrhenius pre-exponent with supporting parameters such as the number of active sites per unit volume N_s, to match the reference reaction progress of 94.8 % at a catalyst bed length of 60 [mm]. The effect of tuning parameters on the reaction progression distribution along the catalyst bed are shown in the Figure 3.1. Along with this the concentrations distribution was compared with the reference figures. Comparing the model results it supports that Pasini et al used a adsorption equilibrium values ranging from 0.001 [$m^3\,mol^{-1}$] to 0.000001 [$m^3\,mol^{-1}$], these parameters are sensible with the assumption of fast adsorption and finite rate desorption. The parameters listed in table 3.1 were compared to find appropriate fit in terms of flow reaction progression and concentration. The resulting concentration distribution of the flow at each tuning values are shown in figure 3.2 & 3.3.

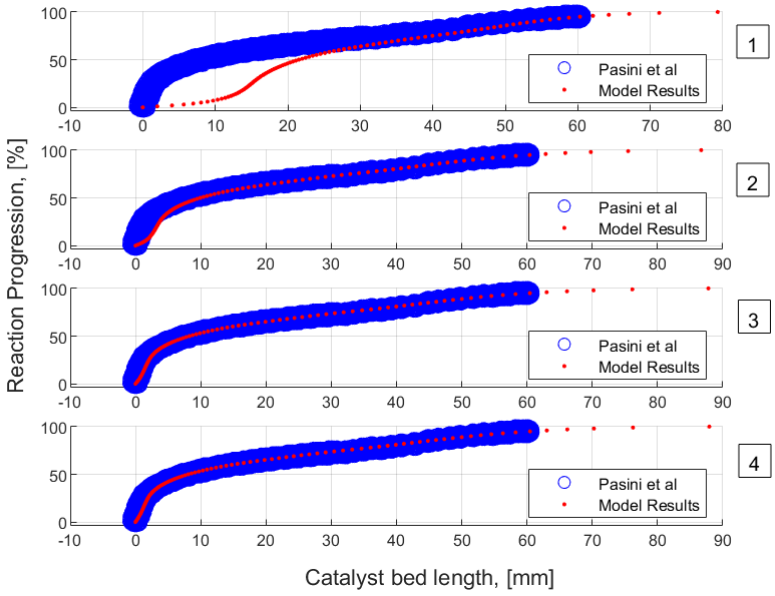

Figure 3.1: Reaction progression distribution at each tuning level from 1 to 4 (top to bottom)

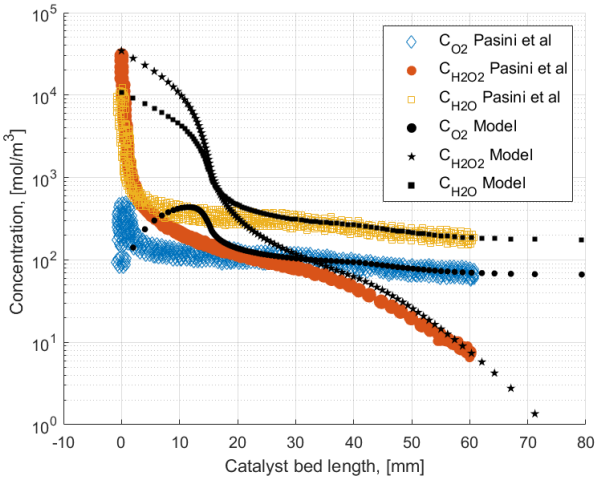

(a) Concentration profiles for case 3 with tuning level 1

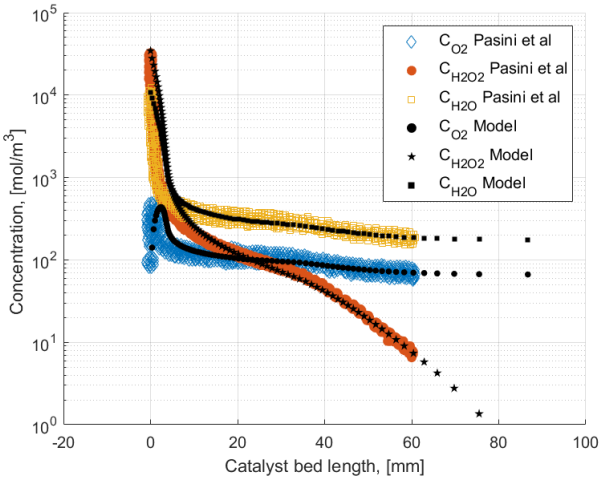

(b) Concentration profiles tuning level 2

Figure 3.2: Flow species concentration profiles for case 3 with tuning level 1 (a) & 2 (b)

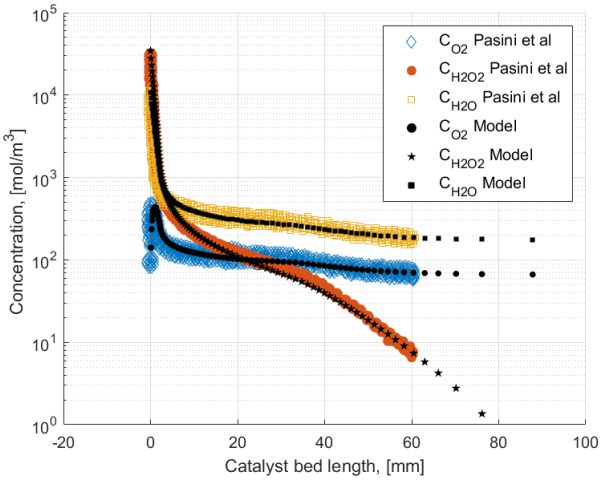

(a) Concentration profiles for case 3 with tuning level 3

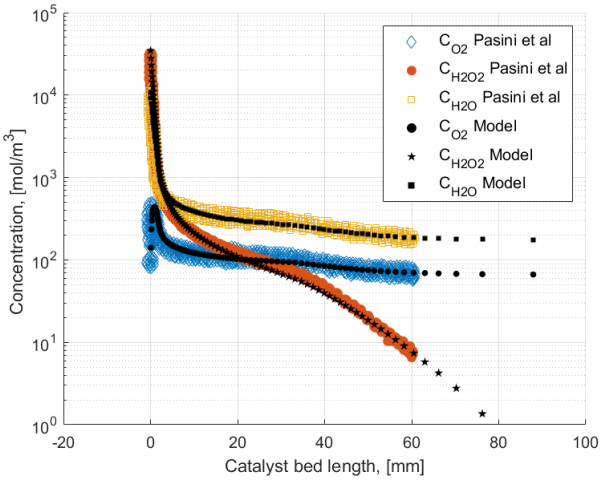

(b) Concentration profiles for case 3 with tuning level 4

Figure 3.3: Flow species concentration profiles for case 3 with tuning level 3 (a) & 4 (b)

By digitising the literature results and comparing them with the simulation results it was possible to try variations on tuning parameters till good agreement in overall trends were seen. The adsorption equilibrium value, number of active sites and the Arrhenius pre-exponent showed an appropriate match to Pasini et al results are given in tuning level 3. As seen from the graphical analysis given in Figure 3.1 to 3.3, the results by Pasini et al are not specific enough to assess any deviation with regards to flow characteristics, but sufficient to show model agreements in terms of reaction progression and concentration trends along the bed length. Hence for comparison of the simulated data, tuning level 3

is used.

3.1.2. MODEL TUNING AND COMPARISON

It was mentioned in the works of Pasini et al that at a chamber of design of $L = 60mm$, the reaction progression β was 94.8% with a chamber temperature of 830 [K]. After performing extensive simulations with different tuning parameters to reproduce Pasini et al modelled conditions (shown in table 3.2), it was realised the best way forward was to match the reaction progress with mentioned temperature. After performing the simulation at feed temperature 298, 291, 288, 287, 286, 283 & 273 [K] with 85.7 % HTP, it was identified that feed temperature of 286.15 [K] produced closest matching result of 832 [K] at 94.8% reaction progression. Once the feed temperature was selected, the tuning parameters were matched to have 94.8% reaction progressions at 60 [mm] bed length, as this was the only given data point. The simulations were performed with tuning level 3 values listed in table 3.1

Using Bey Eigenberger relation 2.83 an average void fraction of 0.3863 was computed based on chamber diameter and pellet diameter. The two phase pressure distribution was analysed and a pressure drop of 0.647 [bar] was realised at a catalyst bed length of 60 [mm]. This is deviation 0.14 [bar] from Pasini et al modelled results and 0.03 bar from their experimental results. The flow maximum Reynolds number was below 1000, values are still within the bounds of validity of the Ergun equation [20]. It is important to emphasise that this simulation was performed at lower mass flux rates and adapting the Tallmadge equation in the pressure drop model is meant for higher flow Reynolds number range. The simulated results show a better agreement to the given experimental data of Pasini et al. Therefore difference in pressure drop of case 3 model results and that of Pasini et al can be reasoned to the difference in the Darcy friction factor between the Ergun equation (used by Pasini et al) and the Tallmadge equation (Used in this model). The use of Lockhart-Martenlli-Chisholm relations in the two phase flow, adapts the flow pressure gradient according to the local flow composition of the catalyst bed and the type of the flow. The two phase flow type results in a viscous-turbulent interaction. In order assess the difference between the pressure models, the Tallmadge equation along with two phase flow adaption are reproduced in Figure 3.7 for the flow conditions mentioned in table 3.2

	Experimental Results by Pasini et al [10]	Model Results by Pasini et al [10]	Model Results case 3
Propellant	85.7% HTP	85.7% HTP	85.7% HTP
Pellet diameter	0.6 [mm]	0.6 [mm]	0.6 [mm]
Bed diameter	18 [mm]	18 [mm]	18 [mm]
Bed Length	60 [mm]	60 [mm]	-
Inlet temperature	Unknown	Unknown	286.15 [K]
Operational Pressure	17.65 bar	17.65 bar	17.65 bar
Mass flow rate	4.84 [gs^{-1}]	4.84 [gs^{-1}]	4.84 [gs^{-1}]
Catalyst	FC-LR-87 (Pt-Al2O3)	FC-LR-87 (Pt-Al2O3)	FC-LR-87 (Pt-Al2O3)
Bed loading	19.02 [kg/sm^2]	19.02 [kg/sm^2]	19.02 [kg/sm^2]
Reaction advancement	-	94.8% (L=60mm)	94.8 % (L=60mm)
Temperature (L=60mm)	831 [K]	830 [K]	832 [K]
Pressure loss	0.65 bar	0.63 bar	0.647 bar

Table 3.2: Comparison table of data generated from the model and data from Pasini et al

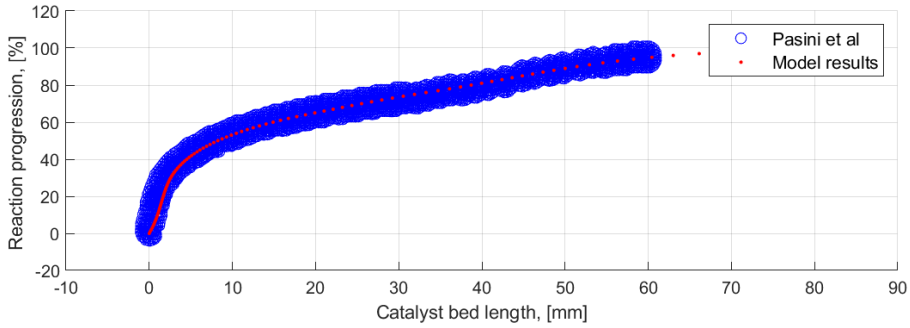

Figure 3.4: Comparison of reaction progression results over the catalyst bed length (case 3)

In Figure 3.4 the reaction progression over the catalyst bed length is shown, the model data shows to have an overall similar trend as the data from Pasini et al. However it is notable that there is a difference from the literature data at least until the first 5 [mm] into the catalyst bed. This deviation can be seen in the flow concentration distribution in Figure 3.5. This initial deviation from literature data can be primarily explained by the fact that the Pasini et al model is based on using a single evaporation fraction for both Hydrogen Peroxide and Water. In the literature data it can be seen that the saturation conditions for the homogeneous evaporation was in between 415 [K] to 536 [K] (average to 475.2 [K]). In this model the saturation temperatures at the pressure (18.3 [bar]) is 481.40 [K] for Water and 544.81 [K] for Hydrogen Peroxide. Hence assuming a unified evaporation with a saturation temperature of 475.2 [K] it would yield a greater gas fraction than identified by the model. As a result of higher gas fraction due to vaporisation, this will result in a lager volumetric flow rate than computed by this model, hence the overall Hydrogen Peroxide concentration [$mol\,m^{-3}$] will be lower. Therefore

the results form Pasini et al show a lower concentration of Hydrogen Peroxide than the simulated results. The gas fractions of the simulated flow are shown in the Appendix B Figures B.6 & B.7. The evaporation profile in Figure B.7 shows that H_2O evaporation completes at 19 [mm] and H_2O_2 evaporation completes at 34.7 [mm]. Another deviation that is notable in the 19 to 34 [mm] of length into the catalyst bed, the deviations can be seen in Figures 3.4 & 3.5. Since the gas fraction of Pasini et al's work is not given, it is not possible to identify the exact location of the catalyst bed where evaporation starts and dry out conditions are met. The deviation between the model and the Pasini et al results can be reasoned to the difference of flow evaporation between the two models. The model results capture the mechanism after dry out condition of H_2O is met, it shows that the flow temperature rises as H_2O_2 progress to decomposes. At 19.91 [mm] of catalyst bed length, the dry out conditions of H_2O is reached and all the H_2O is in gaseous state. There on the H_2O_2 progresses to decompose resulting in a flow temperature rise, when the reaction has progressed to 34.7 [mm] catalyst bed length (the majority of the H_2O_2 has reacted, up to 77% reaction progression) the flow dry out condition of H_2O_2 is reached (this point onward, the flow is purely gaseous). The rise in temperature between 19 to 34.7 [mm] of bed length causes the volumetric flow rate to be greater than that of Pasini et al, due to the relation shown in equations 2.38 & 2.39. Hence Pasini et al's results in higher concentration than yielded by the model results (the concentration of the flow is inversely proportional to the volume of the flow). Further down the catalyst bed the results converge as expected in the gas phases. The primary difference between this model and works of Pasini et al are in the two phase region, this can be reasoned due to difference in approach of modelling the flow gas fractions in the two phase region.

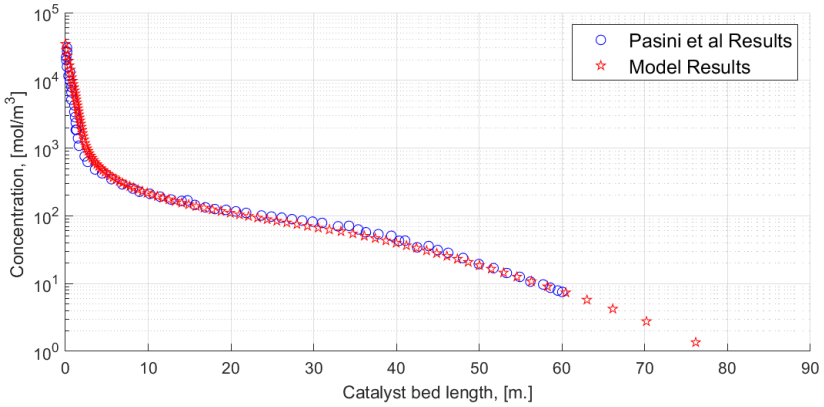

Figure 3.5: Comparison of Hydrogen Peroxide concentrations over the catalyst bed length (case 3)

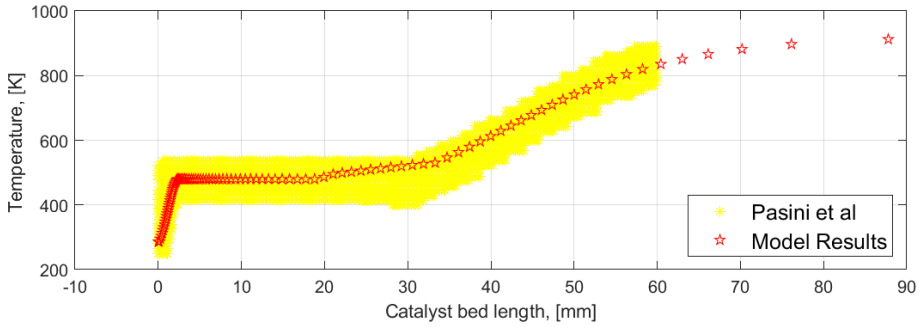

Figure 3.6: Comparison of temperature results over the catalyst bed length (case 3)

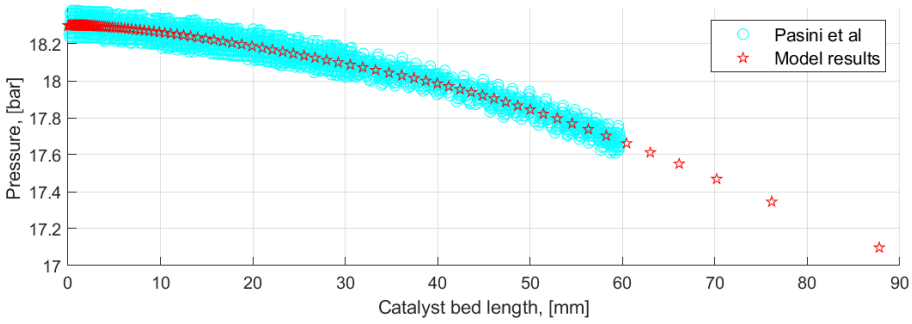

Figure 3.7: Comparison of pressure distribution results over the catalyst bed length (case 3)

The pressure distribution over the catalyst bed is shown in Figure 3.7, the pressure distributions shows good agreement between the model generated results and the results Pasini et al. The literature results was based on the Ergun equation for a single phase flow. The model results are based on a Tallmadge relation (extended Ergun equation) with two phase flow correlations. Due to the scaling of the literature data plots, the exact data points of the distribution cannot be read accurately, however it is notable that there are slight deviations in pressure distribution in the data sets. In the two phase region of the catalyst bed ($L < 34.7$ mm), the model shows a lower pressure drop. The majority contribution of the overall pressure drop is in the gas phase region. The pressure losses are given in the Table B.1. Since the pressure losses were explicitly mentioned in literature (both simulated and experimental values), the deviations of pressure losses with respect to experimental values and Pasini et al's model are calculated and tabulated. The model generated results has a 2.61% (3.08% - 0.467%) better agreement to the given experimental result than that of Pasini et al model. Looking at the reaction profile and concentration profile in Figures 3.4 & 3.5, it is evident that overall flow characteristics between this model and Pasini et al's model are different in the two phase region. Similarly the pressure distributions show deviations in the two phase region. The model shows less steep gradient on the pressure distribution curve in the two phase region (for

all $L < 34.7$).The pressure loss is shown in Figure 3.8. The pressure loss due to two phase flow experienced up to catalyst bed length of 34.7 [mm] is 0.256 [bar] (this is 40% of the total predicted pressure loss of 0.66 [bar]). Predominant contribution to the pressure losses is from the gas only phase region which is 0.374 [bar] (this comes to 59.36% of the pressure losses). However as seen from figure 3.8 for a longer catalyst bed than 60 [mm], the gas phase contribution to the pressure losses becomes more prominent.

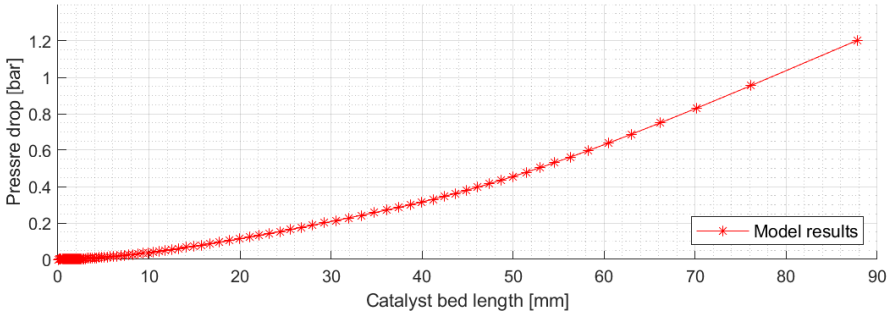

Figure 3.8: Pressure loss over the catalyst bed length (case 3)

Irrespective of the good agreement in pressure distribution and pressure drop between the modelled case 3 results and results of Pasini et al, the flow properties such as the gas fraction and temperature does show deviation, particularly in the two phase regions. This can be due to the fundamental assumption, that is the difference of modelling the flow with a single evaporating fluid rather than two evaporating fluids. Since Pasini et al applied the Ergun relation in their work, using the case 3 inputs, the pressure drop was compared between the two phase Tallmadge relation to Ergun equation (without two phase correlations) this is shown in figure 3.9. However the results yielded from this attempt was (18.46% higher than experimental result) 22.22% higher than their simulated results. The Ergun equation predicts a much higher pressure drop over the catalyst bed 0.77 [bar] at 60 [mm]. The same observations were made between the Ergun relation and Tallmadge relations (Ergun relation producing a higher pressure drop than Tallmadge relation in packed beds) by Koopmans et al [18] and Brunner et al [37]. Hence it is evident that the difference in propagated flow properties contribute to the deviation of Pasini et al results to the results of this work.

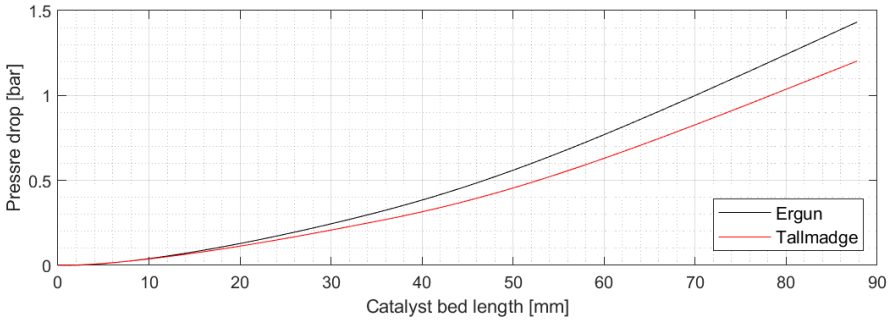

Figure 3.9: Pressure loss comparison between simulated Tallmadge relation and Ergun relation for (case 3)

With the lack of exact tuning parameters, model input conditions (feed temperature) and readable results by Pasini et al limits the verification process. Therefore, the model verification in this case was limited to a graphical comparison, this show that the model produce similar results and trends. But its not possible to assess exact deviation between the two model results. The pressure drop predicted by this model in this single case has a good agreement with Pasini et al's results (also agrees well with experimental data with 3 % difference). However, further verification of the model is required to assess the differences and identify is these differences are acceptable.

3.2. FURTHER MODEL COMPARISON

In order to further verify the model data is compared to the works of Jung et al. The simulations by Jung et al demonstrated the temperature and pressure distributions over the catalytic bed for varying input conditions. This data enables further level of verification by quantifying the difference between the two models.

Jung et al performed simulations based on Manganese Oxide(s) Mn_xO_y catalyst. The properties of the catalyst geometry and the conditions of the HTP are tabulated in Table 3.3. The inlet conditions for the simulations such as the inlet pressure and the inlet temperature is taken from the results given by Jung et al. The inlet temperature of 296.15 K is set for the simulations and the pressure is varied depending on the simulation case. The shape of the catalyst is not explicitly stated by Jung et al, but size is stated as ranging from 1.18 to 2 [mm]. However for this analysis its assumed that the shape is spherical (based on the Ergun pressure drop model used by Jung et al) with average pellet diameter of 1.59 [mm]. Their work states the catalyst properties used in simulations, the values are tabulated in Table 3.3. Some parameters given by Jung et al lacks the units, these are missing for the adsorption equilibrium constant and the number active sites per unit volume. These parameter values were given as $K_1 = 1$ & $N_s = 1$. Though the units are not stated in the works of Jung et al, there is a possibility that their work used reaction progression gradient with respect to [mm] instead of [m], this would yield units [$\mathrm{mol\,s^{-1}\,mm^{-1}}$]. Similarly the concentration calculated in [mole/l] instead of units [$\mathrm{mol\,m^{-3}}$] therefore the adsorption equilibrium constant is possibly given in [$\mathrm{l\,mol^{-1}}$] instead of [$\mathrm{m^3\,mol^{-1}}$]. By

performing numerous simulation with varying tuning parameters given Jung et al (since units were not given), it was concluded that the parameters given were disproportionate and the units were revised for aforementioned parameters. This resulted in $K_1 = 0.001$ [$m^3\,mol^{-1}$] and $N_s = 1000$ [m^{-3}], which gives good agreements with the results of Jung et al. The parameters used in model setting are tabulated in Table 3.3, these parameters were fixed for the simulation of case 4, 5, 7, 8 and 10. For cases 9 & 11 the pellet diameter used was different and listed in 3.4. Case 6 was the only situation where the tuning parameters did show agreement. The simulation cases are summarised in table 3.4 with relevant input parameters.

Parameter	Unit	Value
E_{f2}	[$J\,mol^{-1}$]	15000
K	[$m^3\,mol^{-1}$]	0.001
N_s	[m^{-3}]	1000
$A_{specific}$	-	21.9934

Table 3.3: Parameters used for model setting

	HTP	Massflow [g/s]	Inlet Pressure [bar]	Inlet Temperature [K]	Catalyst pellet diameter [mm]	Catalyst bed diameter [mm]
Case 4 (standard)	90 %	67	25.3	296	1.59	29
Case 5	90 %	33.5	14	296	1.59	29
Case 6	90 %	93.8	31.8	296	1.59	29
Case 7	80%	67	19.8	296	1.59	29
Case 8	95 %	67	28	296	1.59	29
Case 9	90 %	67	18.5	296	2.59	29
Case 10	90 %	67	30.8	296	1.095	29
Case 11	90 %	67	12.7	296	1.59	45.8

Table 3.4: Simulated cases and their input parameters

The simulated cases are compared with the results of Jung et al, these results include model generated and experimental results of pressure distribution along the catalyst bed and temperature distributions. The results of the aforementioned cases are shown in Figures 3.10 and 3.11. The primary difference between the model results and the results of Jung et al, is that their results are propagated up until the end of the catalytic bed whilst the model results simulated until the reaction is complete. In each case, the inlet conditions are varied in HTP concentration, massflow, pressure or pellet diameter. Case 4 is defined as the standard/control case and other cases from 5 to 11 haeve at least one change in the aforementioned variables when compared to case 4. The Figures 3.10a to Figure 3.11d depict temperature distribution of the flow over the length of the catalyst bed simulated by the model along with the results of Jung et al.

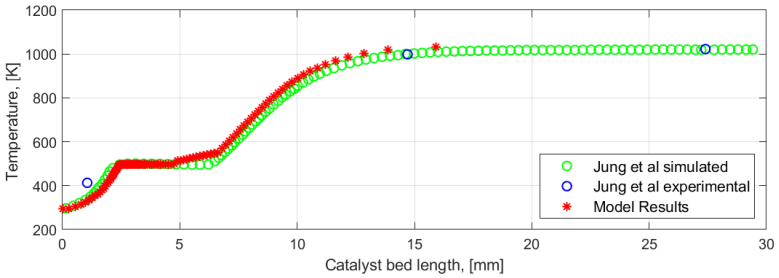

(a) Temperature distribution over the catalyst bed (case 4)

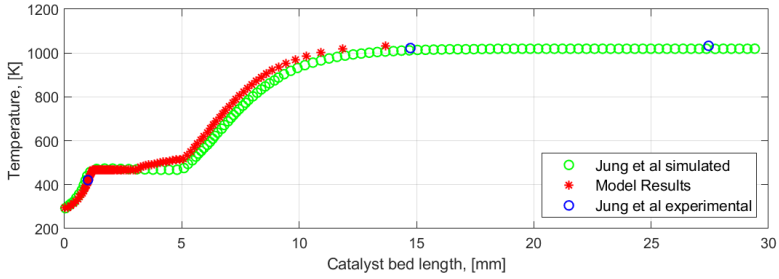

(b) Temperature distribution over the catalyst bed (case 5)

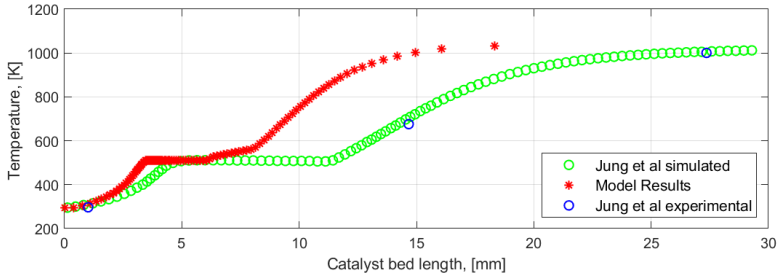

(c) Temperature distribution over the catalyst bed (case 6)

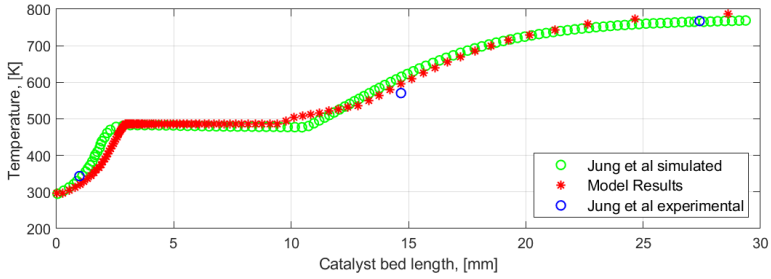

(d) Temperature distribution over the catalyst bed (case 7)

Figure 3.10: Flow temperature over the catalyst bed for case 4 to 7

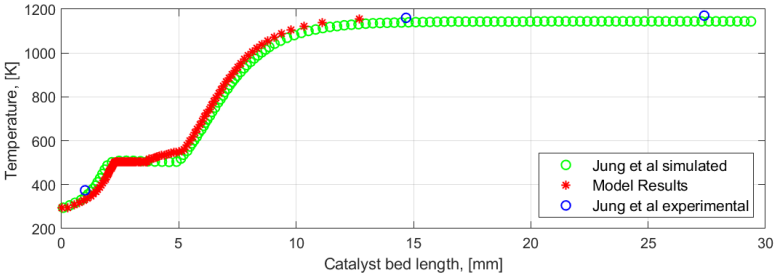

(a) Temperature distribution over the catalyst bed (case 8)

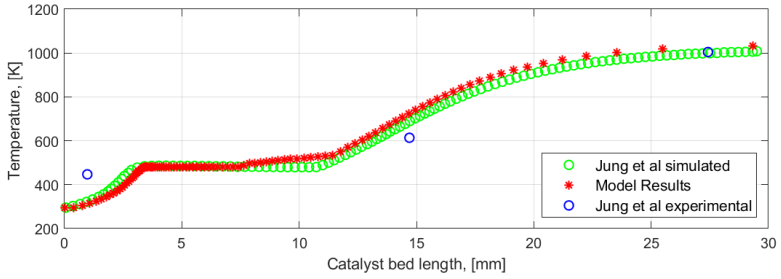

(b) Temperature distribution over the catalyst bed (case 9)

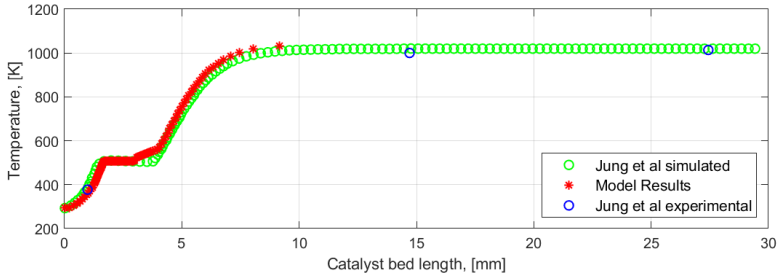

(c) Temperature distribution over the catalyst bed (case 10)

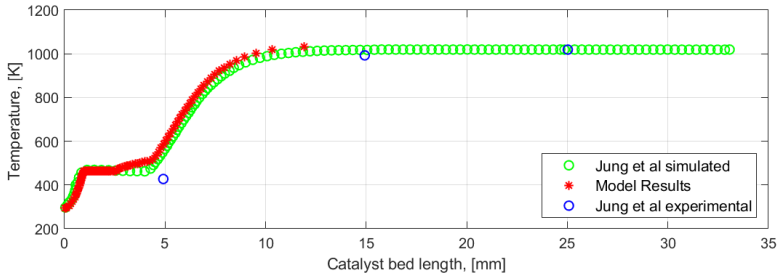

(d) Temperature distribution over the catalyst bed (case 11)

Figure 3.11: Flow temperature over the catalyst bed for case 8 to 11

In the standard case 4, the simulation results show relative good agreement with the re-

sults of Jung et al. The notable primary difference when compared to Jung et al results is the heating of flow after the dry point of H_2O is reached. In the model dry out point of H_{20} is reached at a catalyst bed length of 4.7 [mm] and H_2O_2 dry out point is reached at 6.6 [mm]. Jung et al model results show a flow dry out point of 6.2 [mm]. This results in a 6% error when compared to the H_2O_2 dry out point of the model. This error is compared with the total design length of Jung et al catalyst bed (29 [mm]) and results in a error of 1.38%. However the impact of assuming H_2O_2 & H_2O to have a single evaporation profile can be seen in the results Jung et al. From the model results it can be seen that after dry out of H_2O the flow increases in temperature until H_2O_2 is evaporated, this increment in temperature cause reaction to progress faster than shown by Jung et al. The model generated results shows that 98% of the reaction is completed at length 12.86 [mm], Jung et al results reach 98% reaction completion at a catalyst bed length 14.55 [mm]. Due to the difference of the adiabatic temperatures between the two models, 98% reaction progression temperature for the model is at 1002 kelvin and for Jung et al, its estimated at 999.6 [K]. The difference in the two model requires greater length for Jung et al's model compared with respect to the results of this model with a bed length discrepancy of 11.61% to reach 98% of reaction progress. This difference when compared to the length of the Jung et al experimental catalyst bed (29 [mm]) using equation 3.2 results in 6.55% . The lower adiabatic temperature shown by Jung et al results are recurring in all cases from 4 to 11, therefore this affect is addressed later in this section, with an overview given in Table 3.5.

$$\sigma_L = \frac{L_{model} - L_{Jungetal}}{L_{Jungetal}} \times 100 \tag{3.1}$$

$$\sigma_{exp} = \frac{L_{model} - L_{Jungetal}}{L_{experimental}} \times 100 \tag{3.2}$$

Unlike the other comparison cases, case 6 shows significant deviation. In Figure 3.10c the simulated results show a faster decomposition than the results of Jung et al. The exact cause of the discrepancy is not known. After thoroughly investigating all cases it was not possible to find the cause of such deviation. However it can be seen with the tuning parameters given in Table 3.3 match well with all other cases except for case 6. It is possible that Jung et al provided case 6 data with different tuning provided the input conditions are true as given. Hence the tuning parameters were used to adapt and the case 6 was re-simulated and results shown in Figure 3.12.

In the model generated results the saturation condition of H_2O is met at 3.5 [mm] and Jung et al's results meets saturation condition at 5.3 [mm], this results in a 34% deviation compared to Jung et al results. In an attempt to produce matching results the tuning parameters A_f or N_S is reduced by 34% (reducing either of the two parameters has the same effect as the product of these values are implemented in the reaction rate equation), this produce good agreements with Jung et al results as shown in figures 3.12.After adjusting the tuning on case 6, temperature distribution in Figure 3.12 is used to determine the difference in between the model results and Jung et al simulated results. The model results shows that 98% of the reaction is achieved at a catalyst bed length of 22.63 [mm], Jung

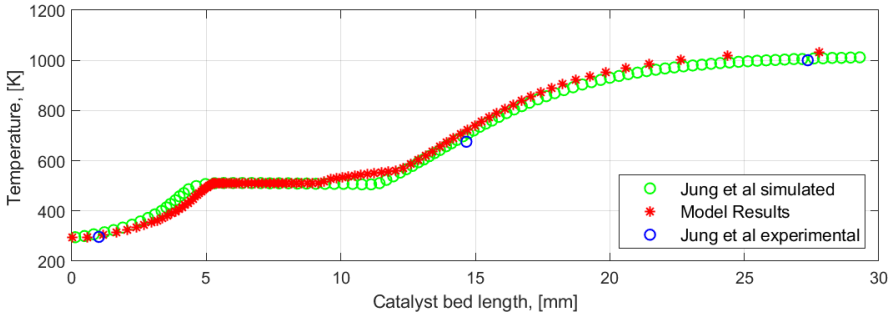

Figure 3.12: Temperature distribution over the catalyst bed (case 6 with revised tuning)

et al results reach 98% reaction progress at a catalyst bed length 25.60 [mm]. Due to the difference of the adiabatic temperatures between the two models, 98% reaction progression temperature for the model is at 1002 kelvin and for Jung et al, its estimated at 999.6 [K] The difference in the two model requires greater length for Jung et al's model compared compared to the results of this model (11.60%). This difference when evaluated to the length of the Jung et al catalyst bed (29 [mm]) results in 10.44% difference.

The catalyst bed length required to achieve 98% decomposition completion for all cases are tabulated in table 3.5, this includes results from the model and Jung et al along with deviation between them. Hence the length required to achieve 98% reaction progression is consistently smaller than that predicted by Jung et al. The model consistently showed in all cases that the length required for decomposition is less than that that predicted by Jung et al.

	$\beta = 98\%$ **Model** $[mm]$	$\beta = 98\%$ **Jung et al** $[mm]$	**Deviation** σ_{exp} **[%]**	**Deviation** σ_L **[%]**
Case 4	12.86	14.55	6.55%	11.61%
Case 5	10.93	12.85	6..62%	14.94%
Case 6 (corrected)	22.63	25.60	10.44%	11.60%
Case 7	22.63	23.61	3.34%	4.15%
Case 8	11.12	11.73	2.07%	5.08%
Case 9	23.54	27.30	12.97%	13.77%
Case 10	7.46	8.36	3.10%	10.36%
Case 11	9.51	10.74	3.72%	11.45%

Table 3.5: Results comparison table

In the comparison between the results it can be seen, the difference in results are primarily due to the difference in evaporation of the fluid flow. Works of Jung et al considers H_2O and H_2O_2 as single evaporating fluid, same as in the works of Pasini et al, this shows a unified saturation condition for both fluids (a horizontal plateau in the temper-

ature distribution). In this work, H_2O and H_2O_2 in the flow were considered as two fluids with their own saturation conditions. Hence after complete phase transition of H_2O, the temperature rises, at this point of the reaction majority of the H_2O_2 has decomposed and the remaining H_2O_2 vaporises at a faster rate as energy from the reaction is utilised to change phase and increase temperature. This increase in flow temperature causes the reaction rate to be higher than that of Jung et al. Hence the results of this work shows that complete decomposition is achieved at a shorter bed length than that predicted by Jung et al. Good agreements of the results are shown in Figures 3.10 & 3.11 except case 6. The model consistently shows that shorter bed length than predicted by Jung et al with deviations ranging from 5.08% to 14.94%.

Case	T_{ad} **Model** K	T_{ad} **Jung et al** K	Δ T_{ad} K	**Difference WRT** T_{ad} **Model**
4	1033	1019	14	1.355 %
5	1033	1019	14	1.355 %
7	787.3	768.9 (max achieved)	18.4	2.337%
8	1156	1144	12	1.055 %

Table 3.6: Adiabatic temperatures achieve by model compared with Jung et al

The adiabatic temperature reached in this model is slightly higher than that of Jung et al, this difference is recurring in all the cases. The adiabatic temperatures reached by the model are tabulated along with values of Jung et el in Table 3.6 for the cases with different feed HTP concentrations (cases 4,5,6,9,10 & 11 have the same HTP concentrations). The cause of the difference can be reasoned due to the specific heat values of the species that are used to calculate the enthalpy. Another reason could be the inlet temperature used by Jung et al is lower than in used in this model. From the data given by Jung et al it can be seen that the inlet flow temperature to be in the range of 293 to 296. Simulation was performed using case 4 conditions with inlet temperature of 293 [K] this resulted in adiabatic temperature of 1029 [K], at 296 [K] feed temperature the adiabatic temperature reached is 1033 [K]. Hence primary contribution to the difference between the two model can be related to the specific heat values, in this model the specific heat values of the species are evaluated based on the species, its state and temperature shown in equation 2.37. The resulting enthalpy determine using an integral form 2.34. A probable cause for the difference could be related to the difference in species specific heat values. Considering Jung et al has not provided the specific heat relations or any enthalpy relations used for the species, it limits the capability to further assess this discrepancy. However it is possible that a constant specific heat value for each species was employed in their work, instead of a value dependent on the flow conditions.

Similarly for all the cases the flow pressure distribution are shown in Figure 3.13 & 3.14. The flow pressures from the model prior to extending the flow to complete catalyst bed length are given in the Appendix Figures B.9 & B.10.

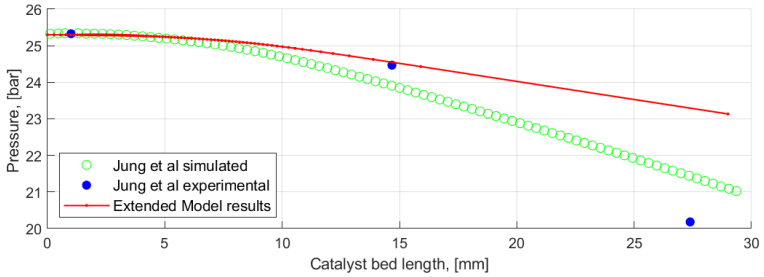

(a) Pressure distribution over the catalyst bed (case 4 extended to catalyst bed length of 29 [mm])

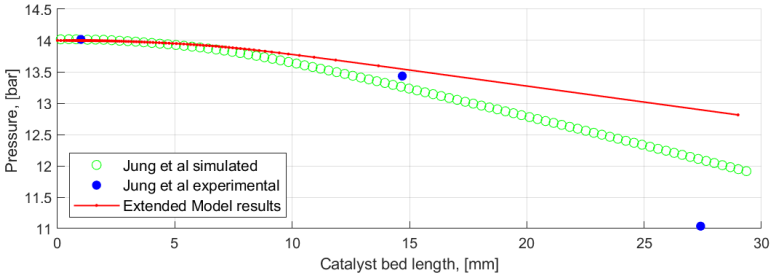

(b) Pressure distribution over the catalyst bed (case 4 extended to catalyst bed length of 29 [mm])

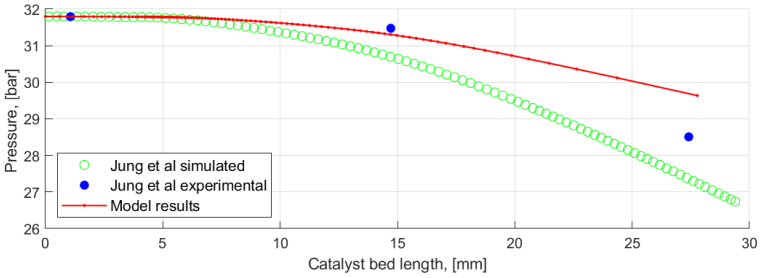

(c) Pressure distribution over the catalyst bed (case 6 with revised tuning

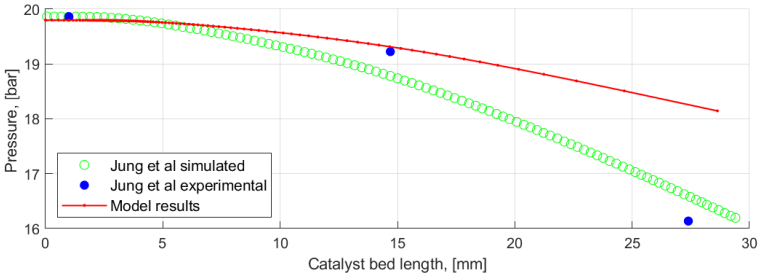

(d) Pressure distribution over the catalyst bed (case 7)

Figure 3.13: Pressure distribution over the catalyst bed for case 4 to 7

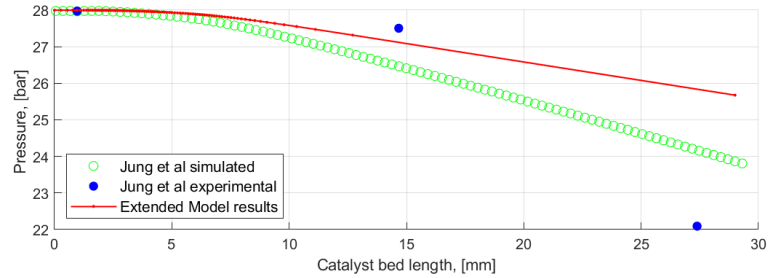

(a) Pressure distribution over the catalyst bed (case 8 extended to catalyst bed length of 29 [mm])

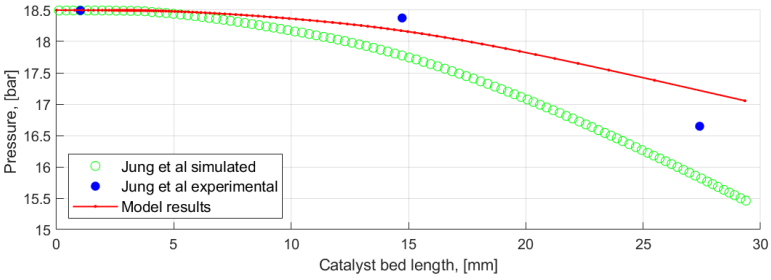

(b) Pressure distribution over the catalyst bed (case 9)

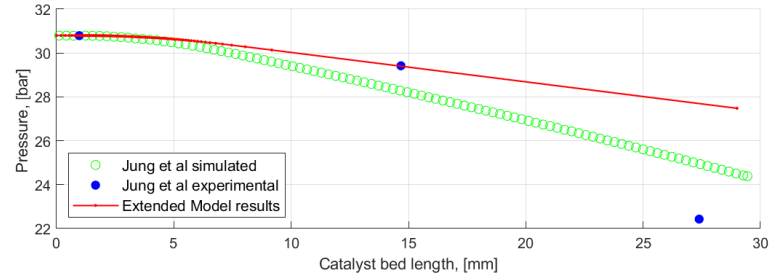

(c) Pressure distribution over the catalyst bed (case 10 extended)

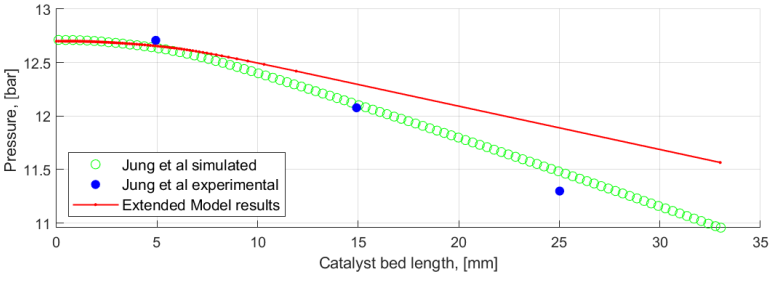

(d) Pressure distribution over the catalyst bed (case 11 extended)

Figure 3.14: Flow temperature over the catalyst bed for case 8 to 11

The pressure distribution of case 4 as shown in Figure 3.15 is only till 15.9 [mm] of the

length of the catalyst bed resulting in a pressure drop of 0.83 [bar], in this region the results of this model match experimental results of Jung et al better. Jung et al records a higher pressure drop of 1.64 [bar] at bed length of 15.9 [mm]. These results are expected as Jung et al used the Ergun relations, as shown in Figure 3.9, which predicts a higher pressure drop than this model. However the model results have good agreement for 2 out of 3 data points of Jung et al's experimental results. The flow Reynolds number exceed 10000 between 2.6 [mm] and 7.5[mm] after which the Reynolds number approaches 6000. Towards the end of the catalyst pack there is a significant deviation in pressure drop between the predicted and the experimental data. Key pressure values that enable comparisons of the two models are tabulated in table 3.7. The pressure distribution is extended using adiabatic flow conditions is depicted in Figure 3.16, in which the pressure distribution is extended to 29 [mm] of the catalyst bed length. The pressure deviation between the model and the results of Jung et al is calculated based on equation 3.3 and is shown in figure 3.17. Compared to the extended pressure curve, it can be seen from table 3.7 Jung et al simulated results match closely with their experimental results.

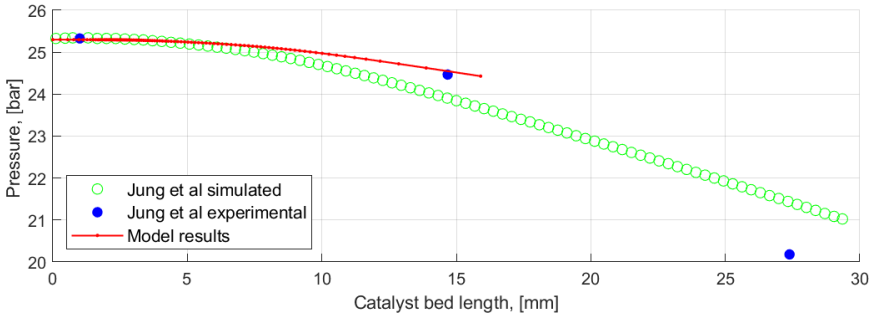

Figure 3.15: Pressure distribution over the catalyst bed (case 4)

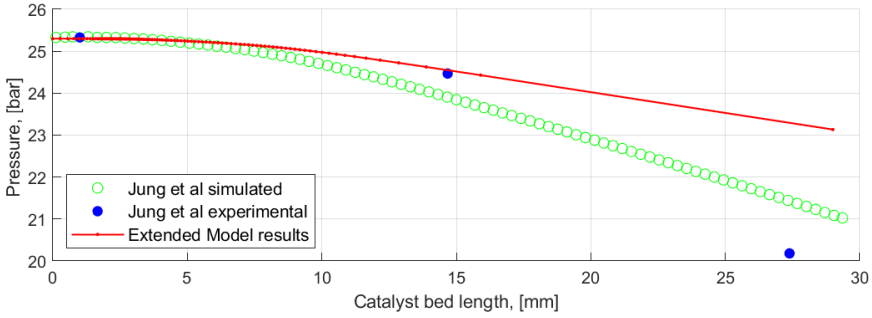

Figure 3.16: Pressure distribution over the catalyst bed (case 4 extended to catalyst bed length of 29 [mm])

$$\sigma_p = \frac{P_{model} - P_{Jungetal}}{P_{Jungetal}} \times 100 \tag{3.3}$$

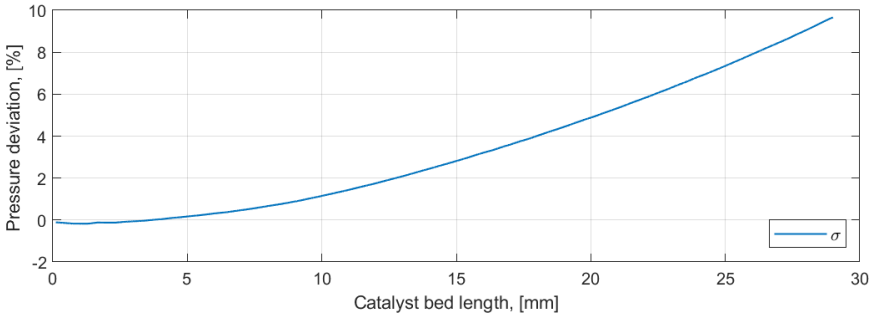

Figure 3.17: Pressure deviation between model results and Jung et al simulated results (case 4 extended to catalyst bed length of 29 [mm])

The overall pressure drop percentage with respect to the feed pressure was calculated. The model results have overall 8.58% pressure drop at end of the catalyst bed while Jung et al results shows an overall 17.0% pressure drop at end of the catalyst bed. These assessments shows that the Ergun relations used for pressure drop used by Jung et al predicts a more overall better agreements, however in up to 15 [mm] of the catalyst bed length the model results show better agreement with Jung et al experimental results. Hence the adiabatic extension shown in figure 3.16, does not adequately represent the pressure drop in this case. In addition to the deviation between the Ergun and Tallmadge relations, there is a difference in adiabatic temperatures, between the this model and work of Jung et al.

Catalyst bed Location [mm]	**Model** [bar]	**Jung et al simulated** [bar]	**Jung et al experimental** [bar]
1.13	25.3	25.34	25.33
14.68	24.55	23.91	24.47
27.4	23.29	21.44	20.18
29	23.13 (Extened)	21.09	-

Table 3.7: Key pressure values (case 4)

In all cases it can be seen that the model consistently predicts a lower overall pressure drop than that of Jung et al. The differences of the two models are given in Figures 3.13 to 3.14. The deviation of the pressure distribution between the model and Jung et al results are shown in Figures B.11 to B.18 in Appendix B. Similarly the pressure reading are

tabulated in Tables B.2 to B.9 in Appendix B. The pressure drop over the catalyst bed and deviation between the two models are tabulated in table 3.8. In all cases from 4 to 10, the first two experimental data points by Jung et al agrees with this model data, this is possibly due to higher Reynolds number of the flow along with the use of the two phase correlation implemented in this model which is not implemented in the works Jung et al. In case 11 particularly, the flow Reynolds number is lower than other cases, due to the lower massflow and shows higher deviation. Hence a better agreement is expected with Ergun equations used by Jung et al. It can be clearly seen that the overall pressure drop predicted by the model is less than that of the predicted by Jung et al. It was also established that the flow temperature between the two model show deviations, hence the flow properties contributing to the pressure distribution shows deviations. The pressure deviations between the two models ranges from 5.55% to 12.18% in all 8 compared cases with an average deviation of 8.82%. In all cases the deviations between the two models are significant as the flow approaches the end of the catalyst bed shown in Figures 3.17 to B.18. This is expected due to difference in friction factors implemented in the two models (with this model implementing Tallmadge approach and Jung et al using Ergun relations). From this analysis it can be seen consistently, that the model produces a lower pressure drop over the catalyst bed than that of Jung et al. Hence the difference between the two models were identified and the difference in pressure distributions of the two models were quantified. From the verification process it was seen that the results between the two models matched by showing a similar trend but showed differences in the magnitude of pressure differences. Contributing to this affect, the water saturation location and the dry out locations are reached earlier in Jung et al results than predicted by the model. This means that the gas development occurs slightly earlier and adds to the overall pressure drop.

	ΔP_{model} $[bar]$	$\Delta P_{jungetal}$ $[bar]$	σ_p [%]
Case 4	2.17	4.21	9.66%
Case 5	1.19	2.05	7.23%
Case 6	2.98	4.92	9.68%
Case 7	1.62	3.6	11.62%
Case 8	2.32	4.14	7.59%
Case 9	1.47	2.97	10.01%
Case 10	3.32	6.28	12.18%
Case 11	1.13	1.74	5.55%

Table 3.8: Overall pressure drop and flow pressure difference of the two models

3.3. VERIFICATION OVERVIEW

In order to verify the model, the model was compared to model results of Pasini et al and Jung et al. In both comparison cases the model shows good agreement. In order to verify the results with that of Pasini et al the model was tuned to identify the unknowns.

The tuned parameters were used along with the given inputs, to simulate and compare the results. Due to quality of the data given by Pasini et al the flow temperature, concentration and pressure were compared graphically showing good agreements and similar trends. However to further validate the model, it was compared with the results of Jung et al. A total of 8 cases were compared with 7 of the cases showing good agreement. In the compared cases the catalyst bed length required for 98% reaction progressions showed consistently that model required a shorter bed length ranging from 4.15% to 14.94% shorter length than that of Jung et al. The difference in the two models was reasoned due to the variation of flow evaporation implemented. Similarly the adiabatic temperatures reached by the two models were compared for cases with varying feed concentration, this show that the model produced adiabatic temperatures (1.06% - 2.34%) higher than that of Jung et al. This shows that the specific heat values used in the two models are possibly different. The pressure distribution between the model and Jung et al when compared showed that the differences in pressure drop between models ranged from 5.55% to 12.18%. Considering the required magnitude of deviation of the catalyst bed (0.61 [mm] to 3.76 [mm]) and the magnitude difference in pressure drop (0.61 [bar] 2.96[bar]) between the model results and Jung et al. It is sufficient to conclude that the model produces consistent results and shows the expected trends. However, considering the provided experimental pressure data by Jung et al is three data points per case, and it deviates in accuracy between experimental and simulated data. Hence requires this work to be validated to identify the accuracy of this model.

4

TEST PLAN & SETUP

This chapter describes the test objective and how the objectives are met with a test plan along with a description of the test setup used to realise the goals. The work is then followed by section on propellant handling describing the measures that needs to be followed when handling HTP. Finally, the procedures used for catalyst preparation are given.

4.1. TEST OBJECTIVE

The test setup was developed and the test were performed in the facility of Dawn Aerospace in Christchurch, New Zealand. The development of the test setup was secondary to application of the test setup in the work of thesis. The objective of the test campaign was to use the test setup and perform experiments to obtain flow pressures and temperatures in the catalyst bed to fulfil model validation.

The objective was met by setting test goals, the test goals were derived by identifying the mutual requirements of the thesis research questions and the company requirements of the decomposition chamber. The test goals were also set with reflection on the research questions to identify the effects test variables on the performance of the decomposition chamber. The test goals are formulated as follows;

1. Test the system at variable bed loading conditions
2. Test system at variable pressures
3. Determine the pressure distribution
4. Determine the temperature distribution
5. Repeat test for validation

Based on the test goals and test setup the test matrix was developed to attain goals. With the design of the test setup and test operations the first two goals were achieved. This was done by having a fixed choke at the catalyst bed exit and keep operating pressure constant for the test, and successively increase the operating pressure. Therefore increasing the system operating pressure would result in an increase bed-loading. The third and fourth test goal was achieved by placement of 3 pressure sensors and 3 thermocouple sensor at the entry, mid point and end of the catalyst bed.

4.2. TEST MATRIX

The test matrix shows the test and minimum required duration for the test to be performed. The tests were selected to be performed at three pressure levels of 60 [bar], 90 [bar] and 110 [bar]. The three pressure levels are selected to capture the impact of pressure on flow temperature and the flow development in the catalyst bed. Operating pressures of 60 [bar] and above were selected considering the lack of data in that pressure region, often for pressures up to 30 [bar] and below was demonstrated by Jung et al and the data was used in Chapter 3. Due to the maximum operating pressure constraint of the system, pressures above 120 [bar] would exceed the safety standards. Additionally, these three pressure levels served as interest for Dawn Aerospace. With the variation of operating pressure the massflow induced varies, hence this permit to capture the impact of flow rate variation along with pressure. However the massflow is not independent test variable with the current test setup. The decomposition chamber, the catalyst bed and the test setup remained unchanged through out the test campaign. Finally, each test is repeated at each pressure level. The test are repeated in order to address the reliability of the data, and show that the test are reproducible. A minimum test duration of 10 seconds is selected, this is to allow temperatures of the flow to be measured as it settles (surpassing thermal transients). The duration is selected based on Experience within Dawn Aerospace with this catalyst. Similarly literature on Manganese oxide based catalyst was reviewed to identify the time required steady thermal equilibrium of the flow in the catalyst bed, works of Heo et al[38] shows a steady temperature is reached within two seconds into the test.

Test	Feed Pressure	Test Duration Required
1	60 [bar]	10 [s]
2	60 [bar]	10 [s]
3	90 [bar]	10 [s]
4	90 [bar]	10 [s]
5	110 [bar]	10 [s]
6	110 [bar]	10 [s]

4.3. EXPERIMENTAL SETUP

The location of the of all test instrumentation is shown in the schematic 4.2. The schematic depicts Nitrogen pressurant tank used with a regulator to pressurise the HTP propellant tank. The propellant tank, once pressurised permits propellant flow to the decompo-

sition chamber through the main valve. The location of sensors in the catalyst bed are shown in Figure 4.1. The primary sensors used for capturing the data is tabulated in table 4.2. For temperature measurements RS Pro K-type thermocouples were utilised and for pressure measurements ifm electronic PT5412 pressure sensors were used. The sensors used are tabulate in Table 4.2. The test setup is shown in Figure 4.3 depicting the decomposition chamber, feed system and the HTP tank.

	Sensor	Operational Range	Accuracy
Pressure	ifm PT5412 [39]	0 to 160 bar	±0.05%
Temperature	RS PRO type K [40]	$-50 to + 1200$°C	$-40 < t < +375$°C = ±1.5°C $+375$°C $< t < +1000$°C = ±0.004[t]

Table 4.1: Test setup sensors

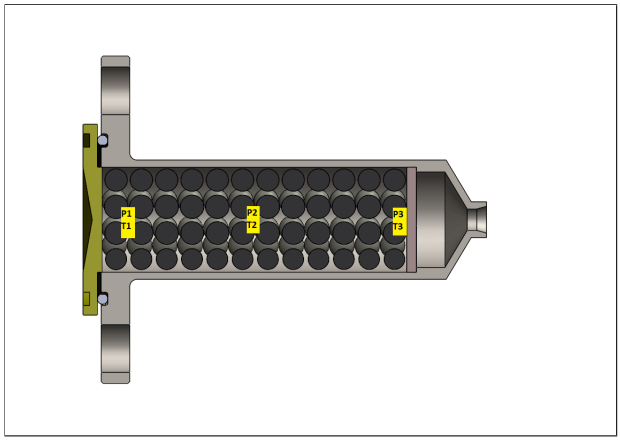

Figure 4.1: cross sectional view of the the decomposition chamber with sensor locations

Sensor	Description	Location	Measuring unit
P_1	Catalyst bed inlet region pressure	0.455 L/D	[bar]
P_2	Catalyst bed mid region pressure	1.818 L/D	[bar]
P_3	Catalyst bed outlet region pressure	3.091 L/D	[bar]
P_t	Tank Pressure	Feed system	[bar]
T_1	Catalyst bed inlet region temperature	0.455 L/D	[K]
T_2	Catalyst bed mid region temperature	1.818 L/D	[K]
T_3	Catalyst bed outlet region temperature	3.091 L/D	[K]

Table 4.2: Test setup sensor placement

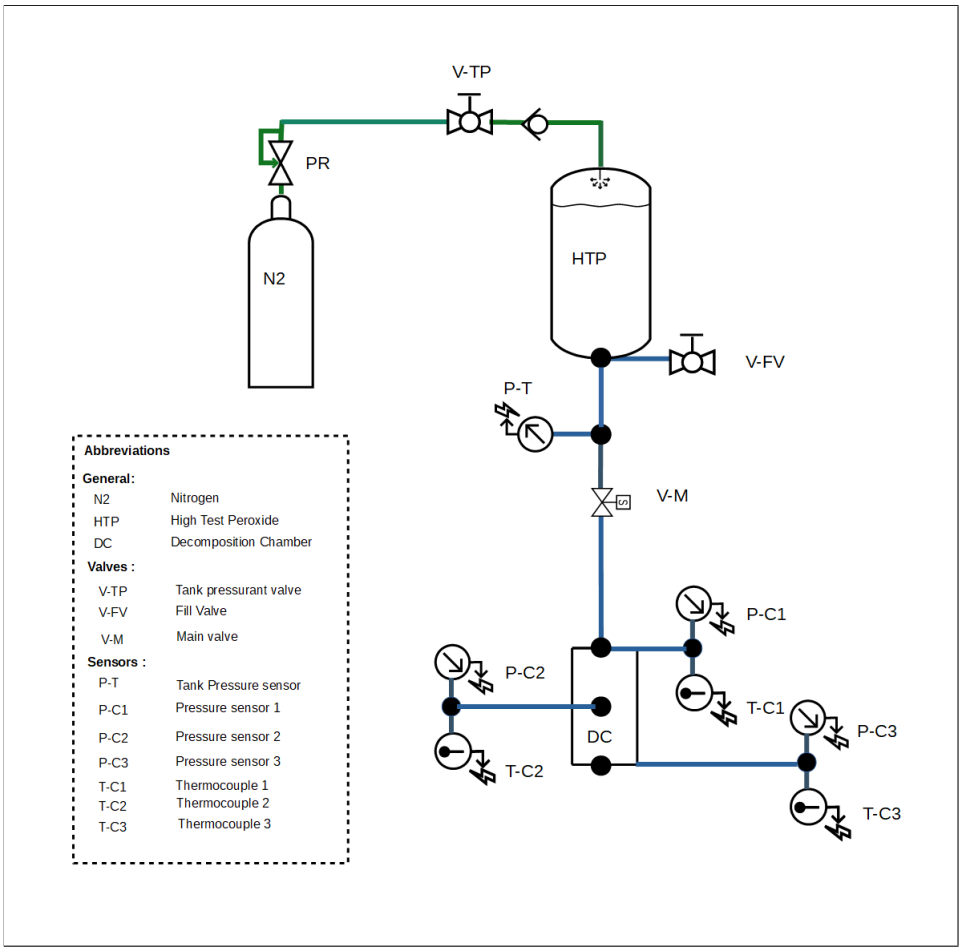

Figure 4.2: Schematic showing the test setup

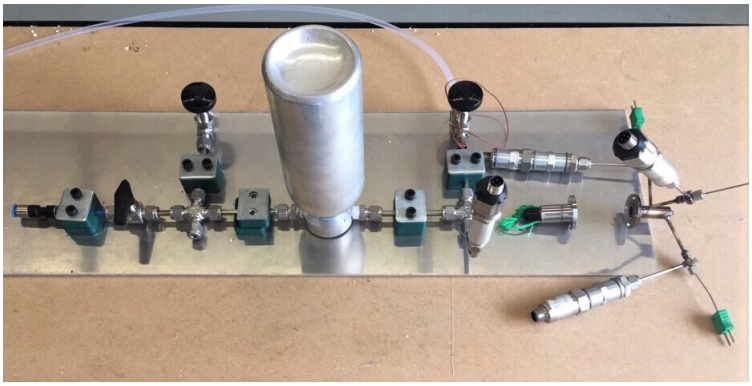

Figure 4.3: test setup showing feed system and the decomposition chamber

4.4. PROPELLANT HANDLING

This section describes some of the fundamental measures followed at Dawn Aerospace test facility, when working with High Test Peroxide. However, a good source for general safety and handling advice on Hydrogen Peroxide is given by Ventrua and Durant [41]. HTP is a strong oxidiser and corrosive in nature, hence required to be handled with extra care. HTP is a strong oxidiser classified as a hazardous material class 5.1 oxidising agent and a class 8 corrosive agent. When handling HTP extreme care is taken and any direct contact must be avoided at all costs [41]. All material that comes in contact HTP is required to be compatible with HTP and handled with proper procedure, typical procedures are briefly explained below. Incompatible material such as organic material are known to catch fire [41].

When working with HTP it is important to have adequate neutralising capacity of water. In case of a spill or contact, it is required to neutralised with water, with adequate amounts of water, HTP can be diluted and resulting flames can be extinguished. Any equipment that has been in contact with HTP is required to be placed in a designated place and rinsed with surplus of water and dried. Attention needs to be paid when using water to neutralise HTP, due to colourless nature of HTP it can be easily be mistaken as water. Hence any unknown colourless spills must be treated as HTP spills and neutralised with water and dried.

A dedicated storage and loading facility is very important when dealing with such propellant. A storage facility storing HTP are required to have certain standards imposed by a government agency. Some storage standards vary depending on the quantity of HTP stored. Storage standards include a isolated storage facility, spill drains, air ventilation, neutralising capability and monitored access. Along with the storage requirement, appropriate safety facilities such as safety shower, eye wash, source of water and personal protective equipment are mandatory.

A fundamental requirement when handling HTP, is that it is handled by two or more

individuals and never alone. This is simply to permit a person to handle peroxide while the other assists with handling and safety procedures. Prior to working with propellant, appropriate personnel protective equipment are worn, this includes Polyvinyl Chloride (PVC) based equipment.

1. PVC apron or suits
2. PVC boots
3. PVC gloves
4. Face shield/ Visor
5. Safety glasses

When working with small quantities of HTP less than 2 kg, then HTP is stored in small closed container places on tray to serve as a drip/catchment tray stored in a cool place. From the small containers required quantities of HTP was extracted to beakers. Once the desired volume of HTP is in the beaker, density measurement is performed in a volumetric flask. The temperature of the HTP is measured and the quantity is weighed. All of the measurements were recorded to calculate density and concentration of the HTP.

In order to load the propellant to the tank, loading procedures are followed. Prior to propellant loading, the area is observed for hazards (any trip hazards or slippery surface), and placing the all extinguish and neutralising equipment in the designated locations. Once the safety measure are in order, the vacuum pump is turned on and an vacuum is created in the tank. After lowering tank pressure the vacuum pump is turned off and the vacuum valve is closed, HTP beaker is brought to the test bench and the feed line is inserted to the beaker. Once the feed line is placed in the beaker the feed valve is opened and the HTP is drawn in to the tank. When all of the HTP is drawn into the tank, the feed lined is emptied by permitting the tank to suck in air. Afterwards the fill valve is closed and the fill line is submerged in a water bath to neutralise any traces of HTP. The HTP beaker is measured prior to rinsing to know the loaded value of HTP.

4.5. CATALYST PREPARATION

Catalyst was prepared in the catalysis lab in the faculty Applied Science in Delft University of technology. The procedures of preparation Manganese Oxide catalyst bed are given as below. Similar MnO_2 catalyst preparation techniques have been successfully demonstrated with operational catalyst bed [2] The catalyst was made using alumina (Al_2O_3) support with spherical shape of 1 mm in diameter, shown in figure 4.4a. The alumina support was washed with demineralized water and dried overnight to remove contaminants and dust caused by pellet attrition. The drop impregnation technique was used to coat the alumina catalyst support with the solution. The alumina catalyst support was first impregnated with 40% Sodium Permanganate solution by Sigma Aldrich. The required quantities of impregnation solution was prepared by estimating the required quantity to fill the pore volume of Alumina. In order to perform impregnation,

estimates of Sodium Permanganate precursor solution prepared based on Alumina pore volume of 0.8 [$cm^3\,g^{-1}$]. With target loading of 13% of MnO_2. Figure 4.4b shows alumina pellets being impregnated with Sodium Permanganate precursor.

Once the precursor is loaded, the alumina pellets were dried for 12 hours in an oven at 80 °C. After dying the impregnated pellets shown in Figure 4.4c with a purple colour. The dried alumina was then calcined in oxidising condition in a Neytech Vulcan electric bench top furnace shown in Figure 4.4d. Calcination was performed for 4 hours at 500 °C. The programmable furnace was setup with a 10 °C per minute ramp up and dwell time of 500 °C for four hours and then ramp down was set at 50 °C per minute. The calcined pellets are shown in figure 4.4e. Finally the calcined pellets are washed with demineralized water to remove traces of sodium compounds and dried at 80 °C for 12 hours. Once the pellets are dried, it is ready to be used as a catalyst for HTP decomposition.

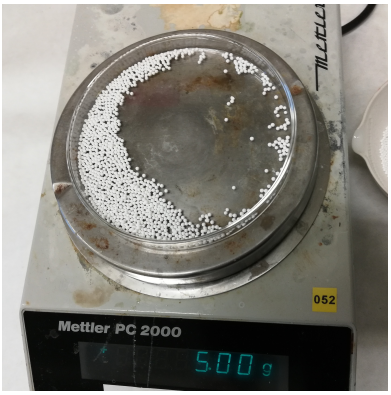

(a) Sample of Alumina pellets prior to impregnation

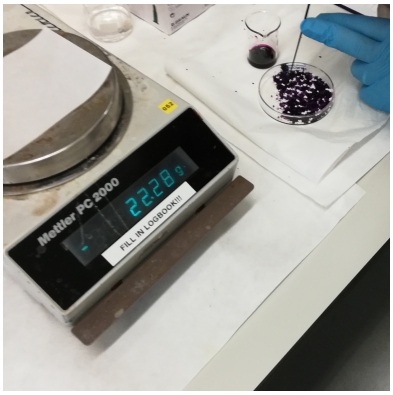

(b) Sample of Alumina pellets being drop impregnated with Sodium Permanganate solution

(c) Sample of impregnated Alumina dried prior to calcination

(d) Alumina pellets in the Furnace for calcination

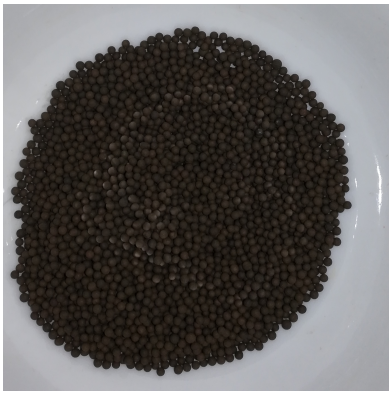

(e) Prepared catalyst after calcination

Figure 4.4: Catalyst preparation

5

EXPERIMENTAL RESULTS

In this chapter experimental results are given and discusses. The results includes measured pressure and temperature data. The results are shown for 6 tests with varying operating pressures and mass flows as described in the test matrix. The test data is then discussed and accordingly data is sampled for simulation model comparison.

5.1. EXPERIMENTAL DATA

The test were performed in Dawn Aerospace test facility in Christchurch New Zealand. The six tests that was described in the previous Chapter were performed and the data recorded. From all experiments performed the data gathered are shown in Figures 5.2 to 5.3. The data recorded consists pressure and temperature with four pressure sensors and three thermocouples. The experiments are repeated in two pressure conditions, to obtain two sets of data at each conditions. Dialling in the exact feed pressure for repeating experiments on the pressure regulator was difficult particularly operating to higher pressures. Hence pressure regulator was set to closest attainable pressure to the desired pressures. The tests E19 and E20 exceeds in test duration than initially intended, this is because it was requested by Dawn Aerospace to couple the last two test till with endurance test testing of the catalyst bed till the HTP tank was emptied. This decision favoured the test outcome, in test E19 prolonged test enabled relative steady feed pressure. In test E20 the pressurant tank was replaced with a new filled one to avoid pressure transient due to sudden expulsion. In addition the prolonged test provided more insight in temperature fluctuations in the catalyst bed. The data from all experiments performed with the variable feed pressures are shown from Figures 5.2a to 5.2f and Figures 5.3a to 5.3f. The test data corresponding to the sensors P_t, P_1, P_2, P_3 measuring pressure and T_1, T_2, T_3 measuring temperature are given in Figures 5.2a to 5.2f and Figures 5.3a to 5.3f, the sensor location in the test setup are tabulated in Table 4.2. These experimental results shows pressures and temperature measured during the decomposition of HTP. The settings of experiments are summarised in table 5.1. Figure 5.1 shows the catalyst

bed during operations, glowing red hot during a test.

Test	Initial feed pressure	Test duration
E13	59.02 [bar]	10 [s]
E14	58.70 [bar]	10 [s]
E15	89.80 [bar]	10 [s]
E16	89.01 [bar]	10 [s]
E19	119.2 [bar]	46.4 [s]
E20	114.8 [bar]	36.5 [s]

Table 5.1: Experimental settings

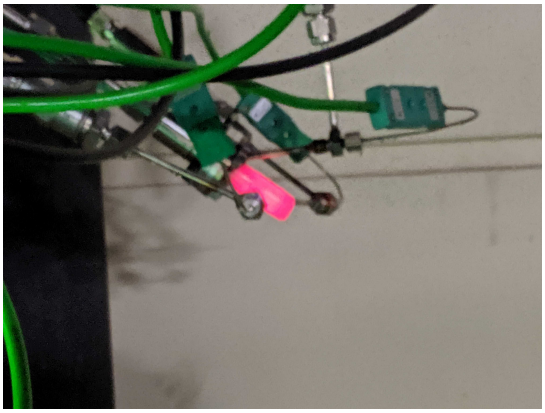

Figure 5.1: Operational decomposition chamber glowing red hot during testing

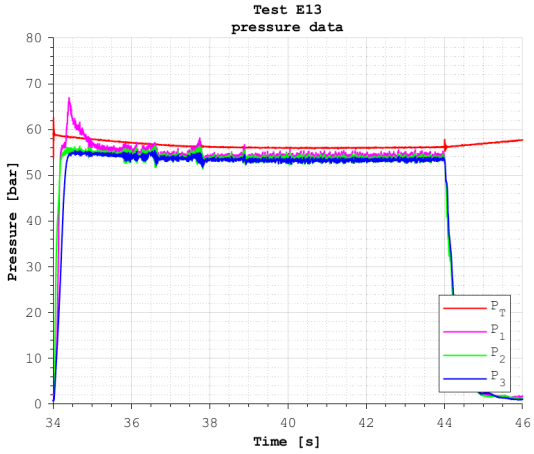

(a) Pressure data (Test E13)

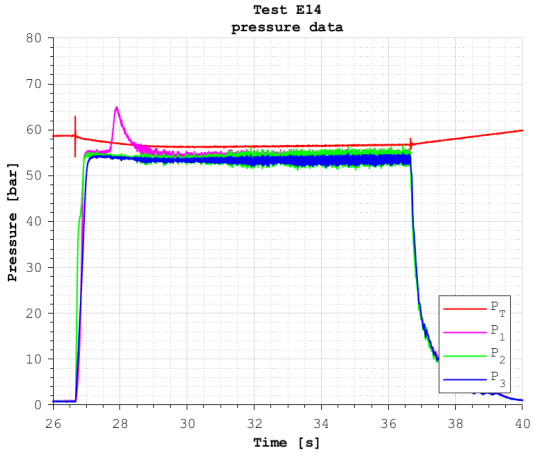

(b) Pressure data (Test E14)

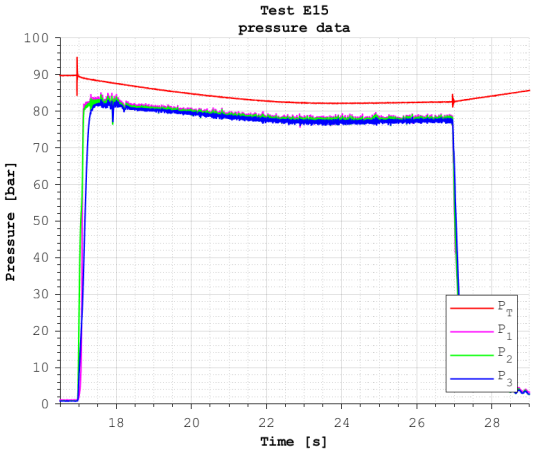

(c) Pressure data (Test E15)

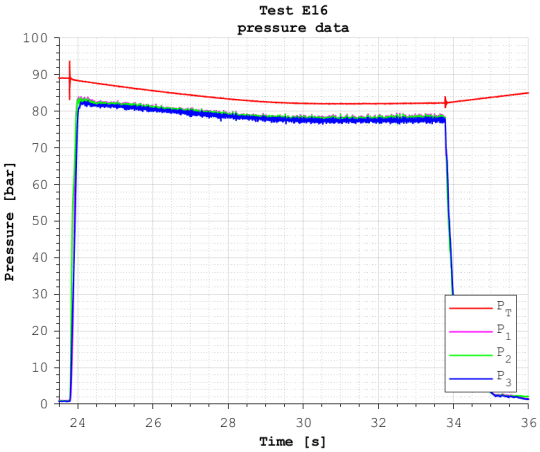

(d) Pressure data (Test E16)

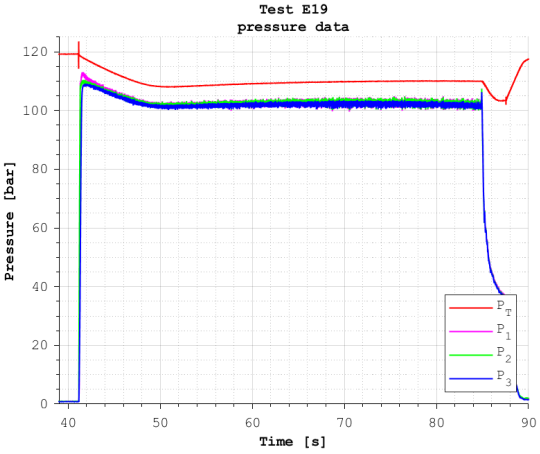

(e) Pressure data (Test E19)

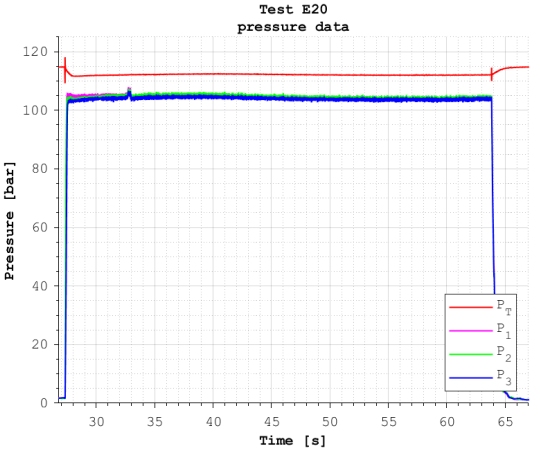

(f) Pressure data (Test E20)

Figure 5.2: Pressure data recorded from experiments

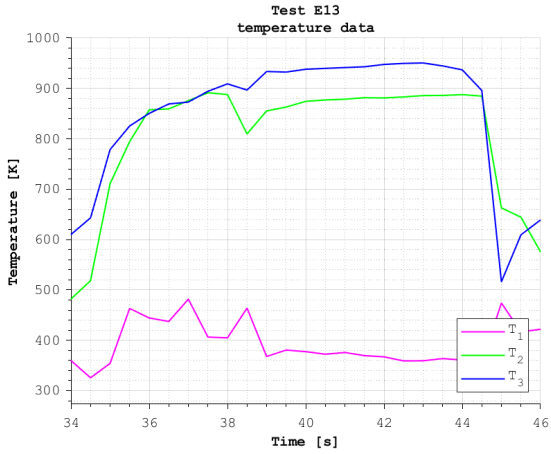

(a) Temperature data (Test E13)

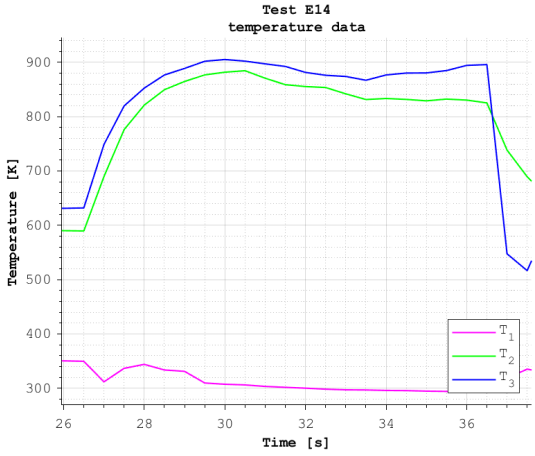

(b) Temperature data (Test E14)

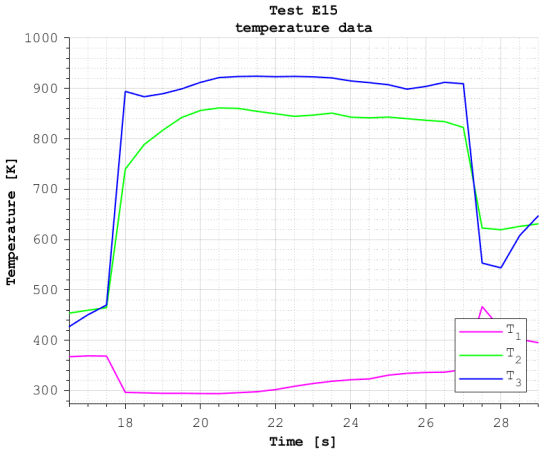

(c) Temperature data (Test E15)

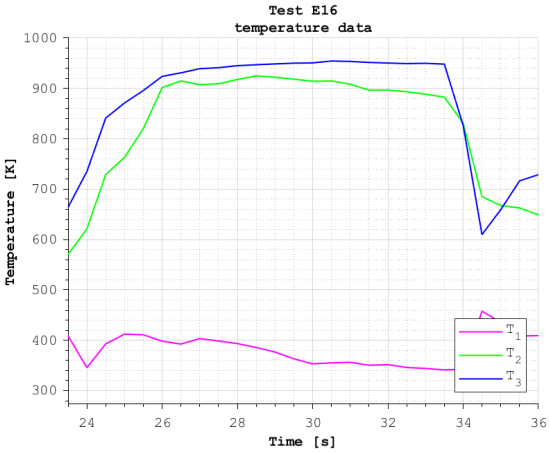

(d) Temperature data (Test E16)

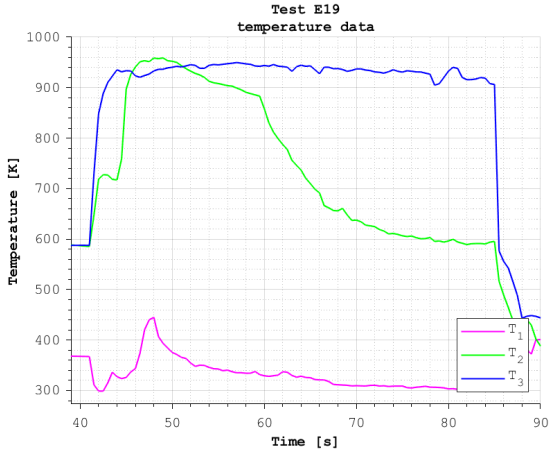

(e) Temperature data (Test E19)

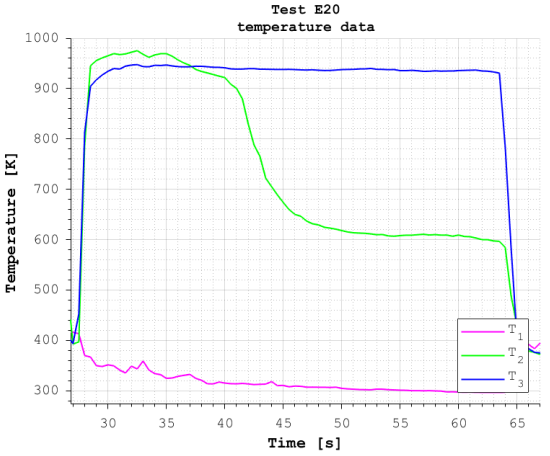

(f) Temperature data (Test E20)

Figure 5.3: Temperature data recorded from experiments

5.2. EXPERIMENT DATA DISCUSSION

The pressure data of the six test shows variation of pressure at the beginning of the test. This is due to sudden expulsion of pressurant tank as the main valve is opened. Depending the fill level of the pressurant tank and the duration of the test operation, the pressure settles to show a flattening HTP tank pressure P_T. The flattening tank pressure settles the massflow rate. In test E19, the fill level of pursuant tank is low and a sudden pressure transient can be seen in P_T at the start of the test in Figure 5.2f. Test E20 was performed with a new pressurant tank (full), showing a relatively still feed pressure.

Test E13 was performed for a duration of 10 seconds, with HTP tank pressure set to 59 [bar]. The test commenced at 34 second mark for 10 seconds, by opening main valve and shutting it. Figure 5.4 depicts pressure data of test E13, the tank feed pressure denoted by P_t and 3 other pressure sensors P_1, P_2 & P_3 reads the flow pressure in the catalyst in the direction of the flow from entry to exit of the catalyst bed. At the start, immediately after the pressure has risen in the location of pressure sensor P_1 at 34.3 [s] a sudden pressure spike was observed, the cause this single spike was related to decomposition of Hydrogen Peroxide in the connecting tube between the chamber and the catalyst. From 35.5 to 38 [s] a slight higher pressure roughness is visible, the cause of this roughness was investigated with a spectrograms given in Figures 5.5 & 5.6. The spectrogram Figures 5.5 capture the excitement due to valve opening and closing during the start and end of the test. The Figures 5.6 show a very slight excitement in low frequency. The pressure drop over the injector is below 5% of the operational pressure, it is probable that the excitement is caused by an slight injector coupled instability at a low range of the operated pressures. Similar pressure spike was observed in the repeated test E14, when pressure data was correlated with the spectrogram shown in Figure C.2, there is low frequency excitement visible ($\approx$ 40Hz). Tests (E15 to E20) that were performed with higher pressures the operation pressures shows no low frequency excitements and the pressure roughness is reduced.

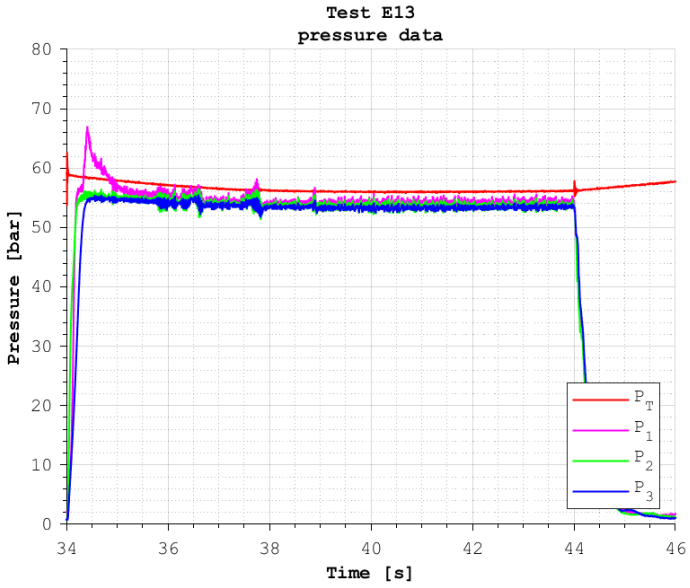

Figure 5.4: Pressure data (Test E13)

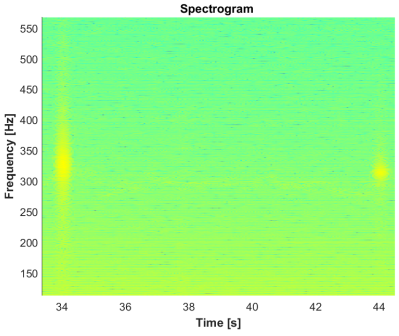

Figure 5.5: Spectrogram on tank pressure data (Test E13)

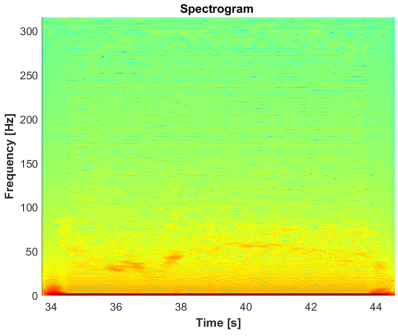

Figure 5.6: Spectrogram on P3 pressure data (Test E13)

In all tests the three thermocouples capture the temperature of front, mid and end regions of the catalyst pack. In all cases it can be the front regions remain cold as the reaction progress is little to none. Depending on the operation conditions such as flow rate and pressure, the temperature measured settles in. In tests E19 and E20 performed at high pressure, it can be seen in Figures 5.3e & 5.3f that the initial temperature recorded with the mid region T_2 thermocouple shows higher temperature than T_3 and with time fades to a lower temperature region showing possible local degradation of the catalyst. However, the outlet temperature remains stable. The Figure 5.7 shows the temperature

measured in Test E13. The thermocouple T_1, T_2 and T_3 shows the flow temperature in the direction from inlet to outlet. At the start of the test the catalyst bed was warm from previous firings. The thermocouple T_1 shows that at the beginning a slight dip, due to the incoming HTP to the catalyst bed. It is probable that pressure roughness experience between 34-38 seconds, causes massflow variations in measure flow temperature. Comparing the three thermocouples it can be seen that temperature shifts and settles in at about 39 [s]. Hence it is important to gather the temperature in settled region than transient, as this enables comparison with simulated data.

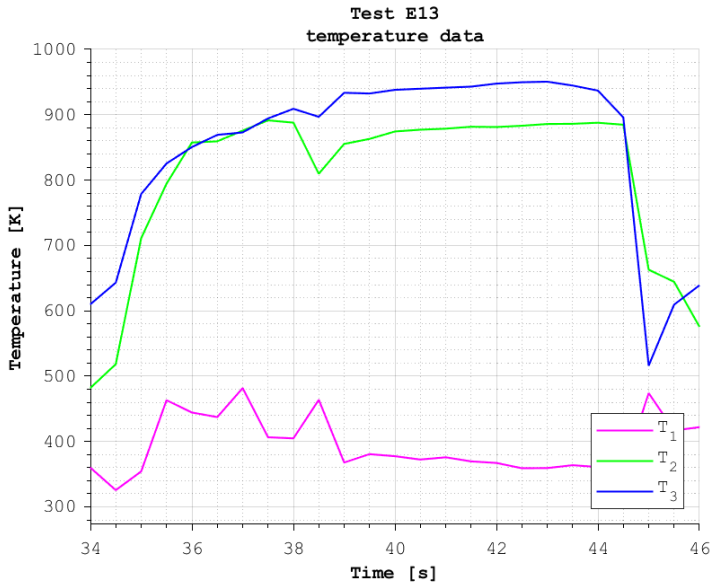

Figure 5.7: Temperature data (Test E13)

5.3. DATA SAMPLING

The purpose of the experimental data is to be used to validate the developed model in the work of this thesis. Hence the experimental results will be compared to the model and difference quantified in chapter 6. In order to obtain model input parameters, stable operative regions of the experimental results needs to be sampled. This is to avoid any pressure transients in the test data (due to tank expulsion or rise time to build up catalyst bed pressure). Pressure transients would lead to variation in the massflow in to the catalyst bed. The pressure rise time at the start of the test $\approx$ 300 [ms]. However, the pressure variation due expulsion of pressurant into the HTP tank requires more time to settle. The temperature transient at the beginning of each test shows that the flow temperature requires to stabilise and reach an equilibrium. In addition to regions with abnormalities such as pressure spikes recorded at the beginning of test 13 and 14 are not acceptable in the sampling width. This would lead to inconsistencies in the validation of the model

When selecting the data sampling region with test E16, it can be seen from temperature data shown in Figure 5.3d with sensors T_2 & T_3 that thermal transient is visible at the start of the test for 2.3 seconds (till time stamp of 26 is reached). Hence the primary driver for initial transient is the time take for temperature to establish, rather than pressure build up Once this is established from temperature data, the pressure data is considered for the final sampling width.From the pressure data on Figure 5.8 it can be seen that feed pressure varied from 89 bar at start to 82 bar at the end of the test. Hence the sample width is select based on region where a relative pressure plateau is seen, depicted in Figure 5.9. In the case of test E16, the sample width is chosen from 29 s to 33.5 s.

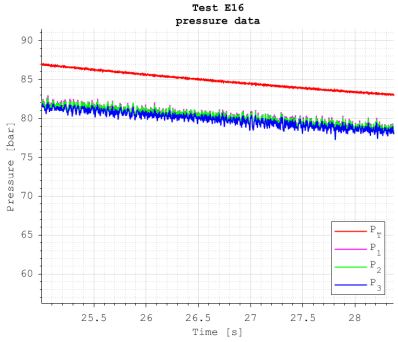

Figure 5.8: sectioned pressure data (Test E16) showing a pressure transient

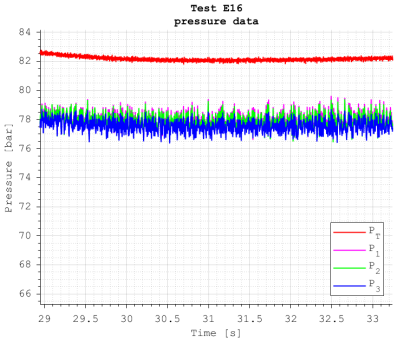

Figure 5.9: sectioned pressure data (Test E16) showing stable region

The massflow rate through injector can be derived by the pressure drop over the injector[42]. The expression used to determine the massflow is given by equation 5.1. Where C_d is the coefficient of discharge and A_i is the injector element(s) cross section area ($A_i \times C_d = 1.8096 \times 10^-7$).

$$\dot{m} = C_d A_i \sqrt{2\rho\Delta P} \tag{5.1}$$

Using the sampled data, the pressure drop over the injector is calculated and the mass flow is predicted based on the using equation 5.1. The feed pressure (P_t) data along with pressure data from front of the injector (P_1) is used to determine the massflow. The massflow is shown in figure C.1 for test E16, using the mass flow data a moving average massflow with window of 100 samples is shown. The predicted massflow is shown in the of with the average flow rate is shown in Figure 5.10. The average massflow of tests performed are determined using equation 5.2 and tabulated in the Table 5.2. Where in n_s the number of data points in the sample width (sensor frequency of 2000Hz) and m_s is the sample measured massflow.

$$\dot{m}_{avg} = \frac{\sum m_s}{\sum n_s} \tag{5.2}$$

$$\sigma_{SD} = \sqrt{\frac{(\sum \dot{m}_s - \dot{m}_{avg})^2}{\sum n_s - 1}} \tag{5.3}$$

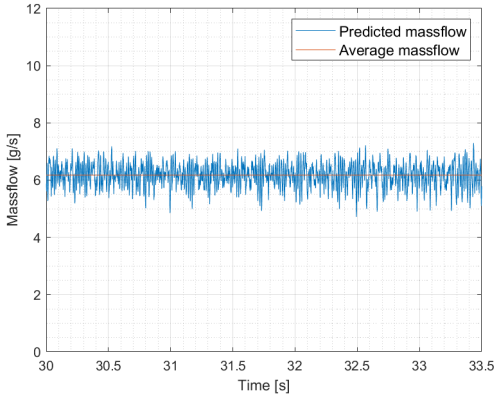

Figure 5.10: Predicted massflow of test E16

The table 5.2 summaries the selected sample width and the predicted massflow of the sampling regions for all test conducted.

Test	**Sample Width** [s]	**Sampling region** [s]	**Massflow** [gs^{-1}]	**Standard deviation** [gs^{-1}]
E13	3	40 - 43	4.60	0.5765
E14	2.5	29.5 - 32	4.61	0.7191
E15	3.5	23 - 26.5	6.12	0.3921
E16	4.5	29 - 33.5	6.10	0.3983
E19	10	70 - 80	8.18	0.3842
E20	6	20 - 86	8.11	0.1671

Table 5.2: Sample data from the test

6

MODEL VALIDATION

In this chapter the model is validated by comparing it with experimental results. First the model settings are given and the sensitivity for the massflow measure was shown. Afterwards the model was compared to six experimental cases, comparing flow temperatures and pressure. The differences between the simulated results and measured results are quantified. Finally an overview of the findings are stated concluding on the accuracy of the model.

6.1. VALIDATION SETTINGS

The model is validated by comparing the simulated result with experimental results. The temperatures and pressures are compared to identify the deviation of simulation results from the experimental results. To increase the reliability of the test data, each test condition was repeated and both sets of data are used in the validation process. All the experimental cases used in the validation process are summarised in the Table 6.1. The experiments can be categorised as repeats of each inlet pressure condition. The flow rate is calculated using Equation 5.1. The model input conditions derived from the test data are given in Table 6.1

Parameter	Units	Case 13V	Case 14V	Case 15V	Case 16V	Case 19V	Case 29V
Pressure	[bar]	54.08	54.06	77.73	77.9	102.6	104.72
Massflow	[gs^{-1}]	4.60	4.61	6.12	6.10	8.18	8.11
Feed temperature	[K]	296.15	296.15	296.15	296.15	296.15	296.15
HTP	[-]	88%	88%	88%	88%	88%	88%

Table 6.1: Validation cases and model inputs

The properties of the catalyst used in simulation tabulated in table 6.2. The same pa-

rameters employed in the works of Jung et al [17] with Mn_xO_y catalyst.

Parameter	Value	Units
E_{f2}	15000	[J mol^{-1}]
K	0.001	[m mol^{-3}]
N_s	1000	[m^{-1}]
$A_{specific}$	22	[-]

Table 6.2: Kinetic parameters used for model setting

In order to use experimental results for validation each case is sampled, the sampling width chosen based on pressure and temperature data achieving steady state or near steady state, the sample window of each experiment case is given in Table 5.2. The purpose of sampling is to identify a stable data range where the flow rate is expected to be constant. This is required as simulations are performed with constant flow rate.The flow temperature distributions along the catalyst bed and the pressure distributions over the catalyst bed are simulated and the data are compared with the experimental results.

In order to address the sensitivity due to variation of massflow, simulations were performed. Considering the massflow of the experimental cases reported in Table 5.2, the simulation were performed for Case 16V with massflow standard deviation ± 0.4. The deviation of temperature distribution over the catalyst is shown in Figure 6.1. With the standard deviation of the massflow incorporated to the simulation, it can be seen that the measured temperatures are will within the bounds of the massflow deviations. However, considering the model is developed to simulate for a single massflow input at a time and sensitivity shown is not inherent to the model but due to measured massflow deviations, it is chosen to validate the model with the experimental average massflow.

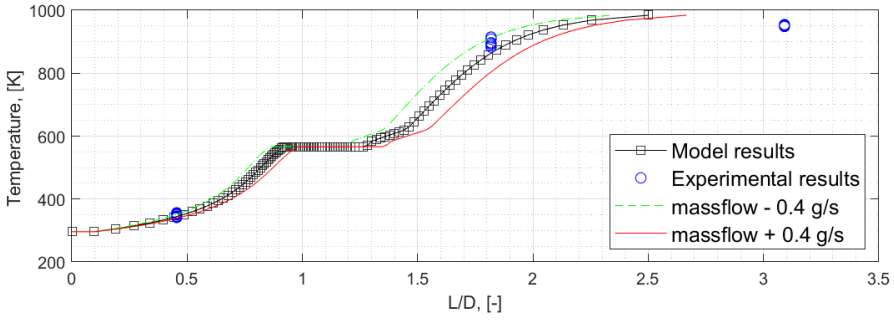

Figure 6.1: Pressure distribution over the catalyst bed with measured results (case 16V)

6.2. MODEL COMPARISON

In comparison between the model results and experimental results, Case 13V is discussed in detail in this section. All other cases are discussed int the same manner is

given in Appendix D. The flow temperatures comparisons of all cases are given in Figures 6.5 & 6.6. The flow pressures comparisons of all cases are given in Figures 6.14 & 6.9 depicting simulated results and the average of the measured pressures. However the actual measured pressures are depicted in Figure 6.4 for case 13V, for all other cases can be found in Appendix D.

In case 13V the data is sampled between 40 and 43 seconds of the test. This sampling width for experimental data is chosen considering as any abnormal pressure deviation and any transient of pressure and temperature data. From the pressure data it can be seen that tank pressure has a transient from 59 to 56 bar from time stamp 34 s to 39 s, after which the pressure remains relative constant at 56 bar. Considering the roughness of the pressure data, the sample mean is computed for 3 pressure sensor data and used in validation process. case 13V is simulated with the conditions listed in table 6.1. The temperature data of case 13V is plotted along with results of the simulation. The range of temperature measured by each thermocouple is listed with in Table 6.3 along with the range of pressures experienced at 3 location of the catalyst bed.

	L/D	Simulated	Measured range	Measured sample Mean
Flow temperature	0.455	383 [K]	359 - 377 [K]	367 [K]
Flow temperature	1.818	914 [K]	874 - 885 [K]	880 [K]
Flow temperature	3.091	-	938 - 950 [K]	944 [K]
Pressure	0.455	54.08	52.5070 55.8050 [bar]	54.08 [bar]
Pressure	1.818	53.98	52.1340 55.1220 [bar]	53.52 [bar]
Pressure	3.091	53.79	52.3800 54.2230 [bar]	53.33 [bar]

Table 6.3: Measured and Simulated parameters at varying L/D of the catalyst bed

The simulated cases are compared with experimental results in figures 6.2 & 6.3. These results include the temperature distribution over the catalytic bed in Figure 6.2 and the pressure distribution over the catalytic bed in Figure 6.3. The measured parameters are tabulated in Table 6.3.

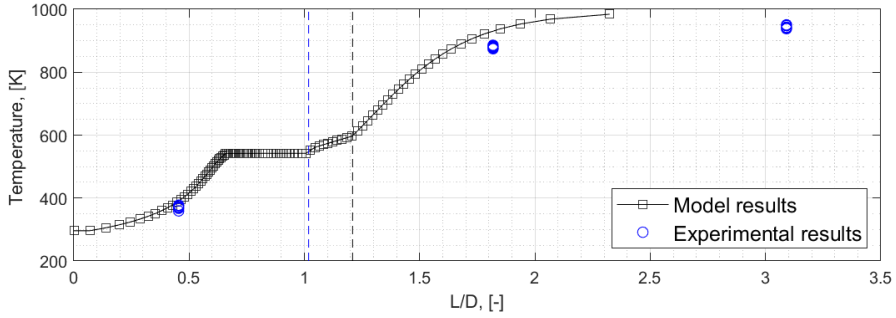

Figure 6.2: Simulated flow temperature distribution over the catalyst bed and experimental results (case 13V)

The temperature profile along the catalytic bed show that experimental data captures pre-boiling region of the temperature profile, prior to the flow reaching saturation conditions. The saturation conditions of H_2O is met at a L/D of 0.685. The blue vertical dashed line indicates the dry out location of water and the black vertical dashed line indicates the dry out location of Hydrogen peroxide (at L/D 1.05 and 1.25 respectively). The second thermocouple at a L/D of 1.8 shows the temperature of the flow to be in gas phase with temperature range between 874[K] and 885[K], the simulation reaches these temperature at L/D range of 1.70 - 1.73. The measured temperatures corresponds to 88.80 % - 89.92% of the adiabatic temperature reached by the model and reaction progression between 93% and 94%. The third thermocouple shows that the temperature higher than the second thermocouple, but still below that of the adiabatic temperature reached by the model. The temperature range reached by thermocouple is in the range between 938[K] and 950[K] this corresponds to 95.31 % - 96.53% of the adiabatic temperature reached by the model. This temperature corresponds to reaction progression between 97% and 98%. By correlating the experiment data and the model data, it is possible to see that the temperature does increase between 2nd and 3rd thermocouple and the maximum temperature lies in between the two. According to the simulated data the adiabatic temperature is reached at L/D of 2.32.

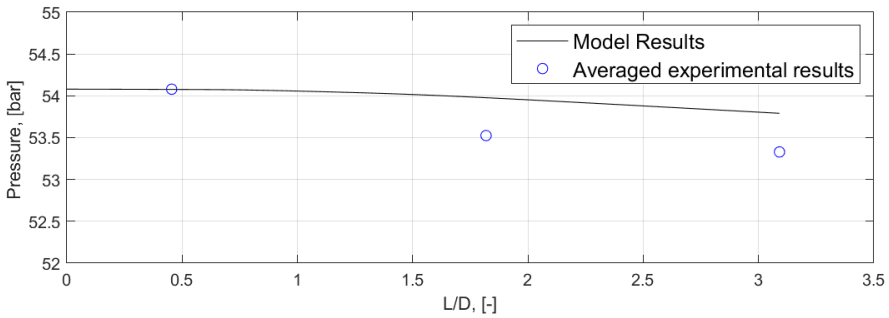

Figure 6.3: Pressure distribution over the catalyst bed (case 13V)

The Pressure data in Figure 6.3 shows the pressure losses experienced by the flow. The experimental data shown in the plot is the average value of the pressure measured. Figure 6.4 displays the actual pressure measured. The even with measured pressure roughness it is visible at higher L/D pressure losses increase as expected. In order to quantify the pressure losses the overall pressure drop compared with respect to the measured mean pressure at the end of the catalyst bed denoted by $P_{3_{avg}}$, this relation is given with equation 6.1. The pressure at varying L/D are tabulated in the table 6.3.

$$Pl = \frac{\Delta P}{P_{3_{avg}}} \times 100 \qquad [\%] \tag{6.1}$$

The overall pressure loss in the catalyst bed is given is shown in 6.3, the simulated pres-

sure drop of 0.289 [bar] and the experimental average 0.749 [bar]. The press loss percentage calculated using equation 6.1, the simulated case pressure loss percentage 0.542% and the experimental pressure loss percentage is calculated to be 1.40%. With the results it can be seen that simulated pressure losses are smaller than actually measured. However this remains similar to the pressure distribution case 3 where the impact of friction factor between the Tallmadge equation and Ergun equation were discussed, which showed consistently a lower pressure drop with the use of Tallmadge equations. Similar observations were made between simulated and experimental data in the verification process with cases 4 to 11, where the measured pressure loss were higher than that simulated.

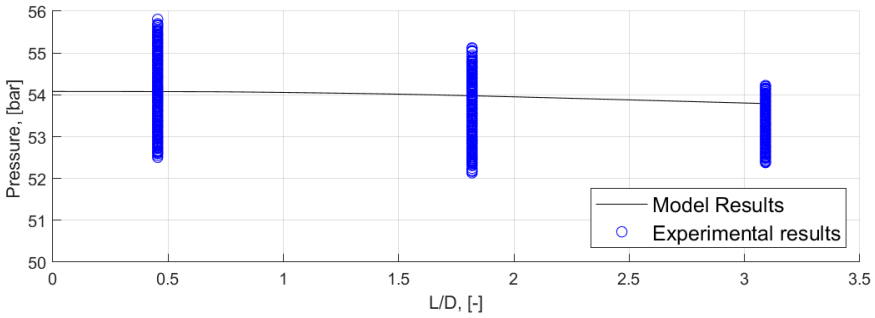

Figure 6.4: Pressure distribution over the catalyst bed with measured results (case 13v)

The pressure roughness of the experimental data in as shown in Figure 6.4 shows that pressures in the sampling region of the data used, the pressure roughness of the data is calculated to be 6.10%, 5.58% and 3.46% in the order of increasing L/D. The experimental pressure loss percentage is factor 2.59 lager than simulated pressure loss. However, considering the absolute pressure drop in the simulated (0.289 [bar]) and the experimental average (0.749 [bar]) with respect to the operative pressure, the pressure loss percentage of the flow is relative small in both cases with a difference of less than 1%. Considering the measured range of pressure roughness, with the lowest being 3.46%, which is much greater than deviation of the pressure loss percentage between the simulated and experimental case (0.542% & 1.40%). Hence as seen shown in the Figure 6.4 the simulated pressure distribution is within bounds of the range of experimentally measured results. Hence it can be consider that the simulation shows good agreement with the experimental results.

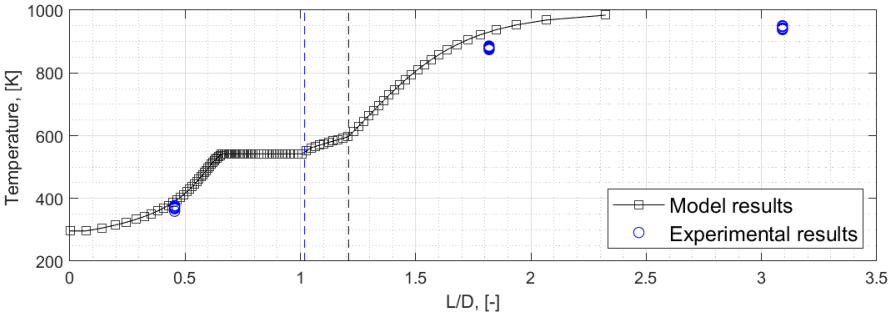

(a) Simulated flow temperature distribution over the catalyst bed and experimental results (case 13V)

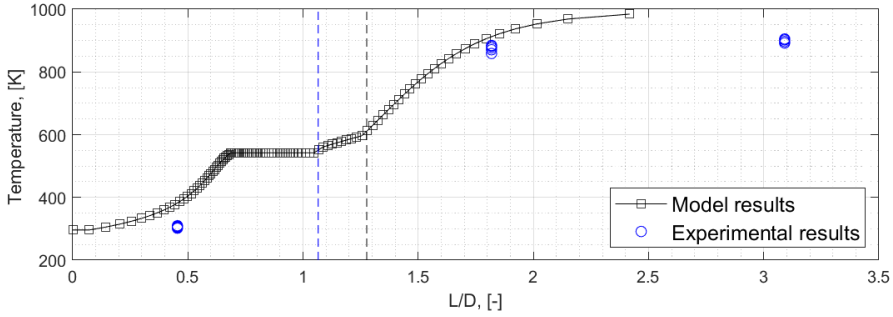

(b) Flow temperature over the catalyst bed with measured experimental results (Case 14V)

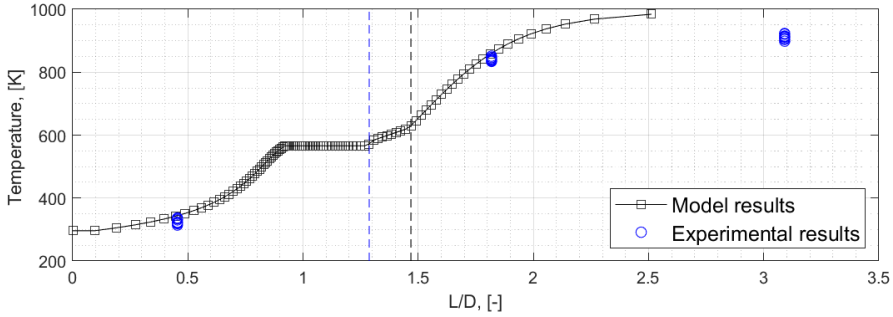

(c) Flow temperature over the catalyst bed with measured results (case 15V)

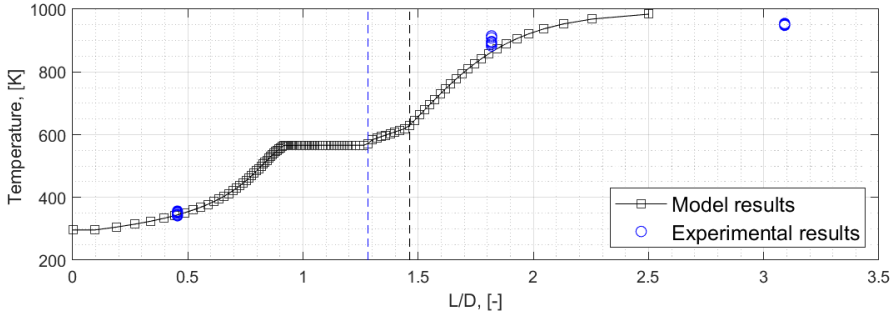

(d) Simulated flow temperature over the catalyst bed and experimental results (case 16V)

Figure 6.5: Flow temperatures over the catalyst bed for cases 13V to 16V

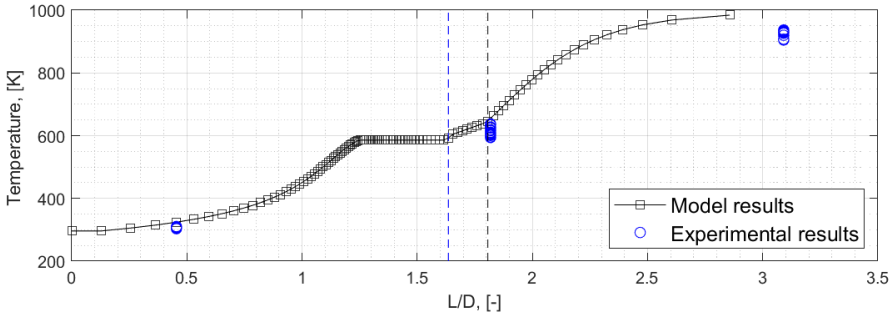

(a) Simulated flow temperature over the catalyst bed and experimental results (case 19V)

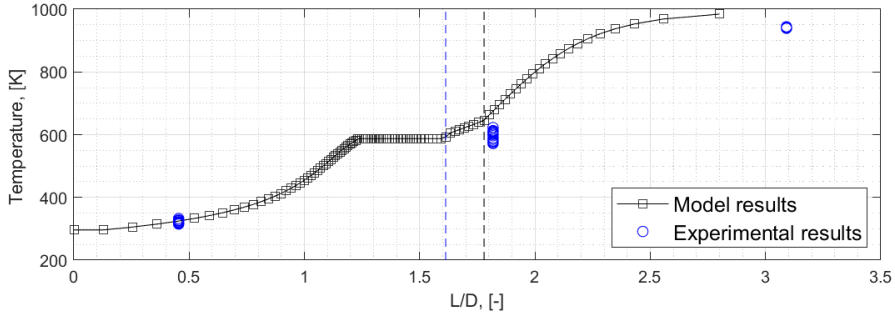

(b) Simulated flow temperature over the catalyst bed and experimental results (case 20V)

Figure 6.6: Flow temperatures over the catalyst bed for case 19V & 20V

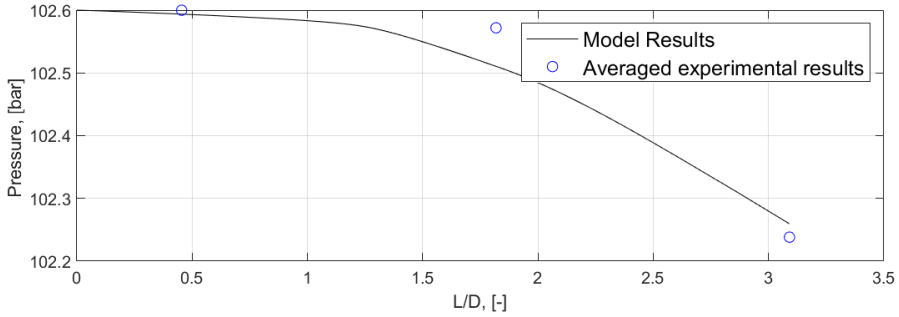

Figure 6.7: Pressure distribution over the catalyst bed and averaged experimental results (case 19V)

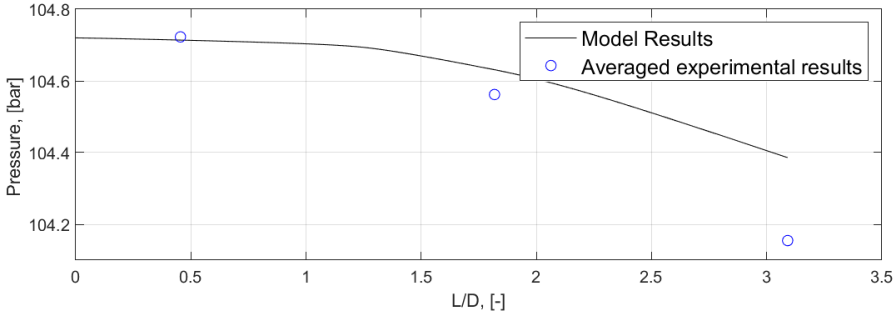

Figure 6.8: Pressure distribution over the catalyst bed and averaged experimental results (case 20V)

Figure 6.9: Flow pressure distribution over the catalyst bed for case 19V & 20V

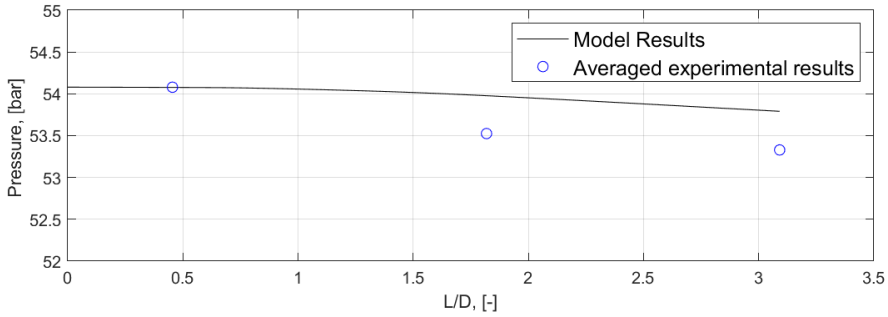

Figure 6.10: Pressure distribution over the catalyst bed (case 13V)

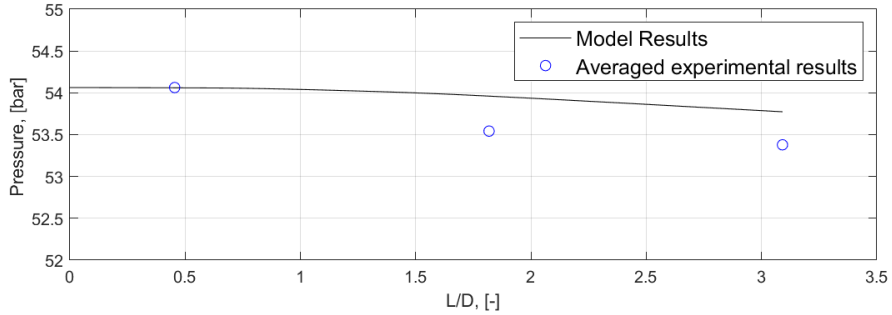

Figure 6.11: Pressure distribution over the catalyst bed with averaged experimental results (Case 14V)

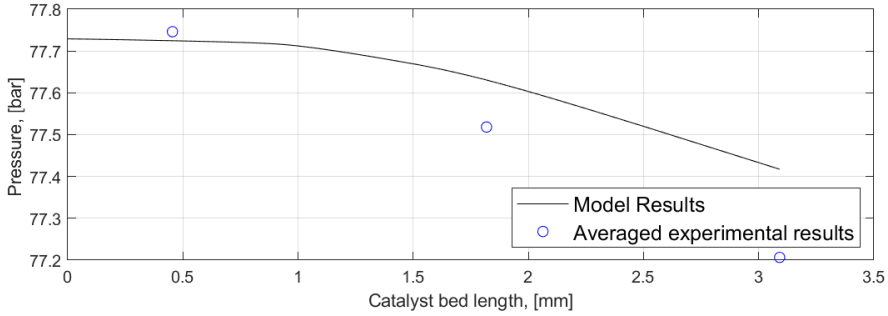

Figure 6.12: Pressure distribution over the catalyst bed with averaged experimental results (case 15V)

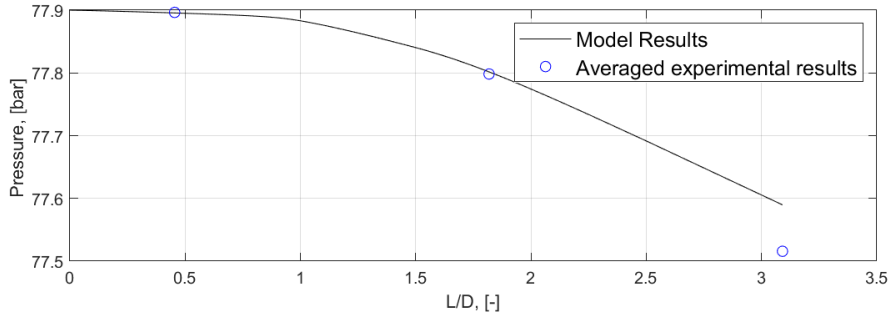

Figure 6.13: Pressure distribution over the catalyst bed and averaged experimental results (case 16V)

Figure 6.14: Flow pressures distribution over the catalyst bed for case 13V to 16V

6.3. VALIDATION OVERVIEW

The test conditions were simulated and the simulation results were compared with 6 test cases. This comparison consisted of flow temperatures and pressures at three different locations of the catalyst bed. In all cases above, the temperatures measured at L/D 0.459 & 1.818 were directly compared to the model results. However, in all cases simulated the flow reached 98 % reaction progression or higher, before L/D of 3.091. In all cases that were compared, the flow temperature measured at $L/D = 3.091$ was lower than adiabatic temperature reached by the model. In all cases 98% decomposition and 100% decomposition occurred at L/D below 3.091. Hence it is possible that measured temperature at L/D 3.091 is with loss of heat to the surrounding after reaction is complete. Figure 6.16 shows series of images from test video footage taken in the night correspond to data used in the validation case 16V (test case 16). These series of images show a red hot glow on the decomposition chamber originating between the sensor placements L/D 1.818 and 3.091. Few seconds in to test, the red hot glow propagates to the end of the decomposition chamber. This series of image from the test footage further validates finding from the model, that maximum temperature of the flow is reached before L/D of 3.091.

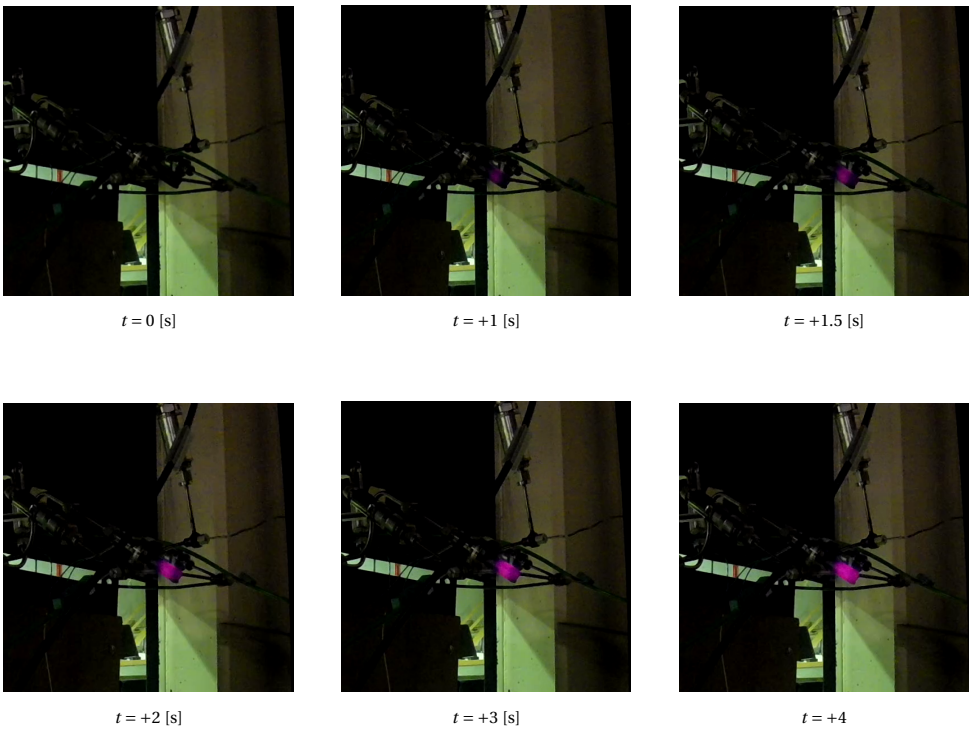

Figure 6.16: Decomposition during 10 second test

An overview simulated temperature and experimentally measured temperature and their deviations at the respective L/D of all cases are shown in the table 6.4. Measurement er-

rors due to sensor inaccuracy is considered small and not accounted for in the validation process. Sensors error maximum applicable is ± 1.5 [K] for temperatures between −40 to 375 [°C] given in Table 4.1. This sensor inaccuracy corresponds to in accuracy of ± 0.30% of the adiabatic temperature. However for higher ranges (+375 to 1000 [°C])the sensor error is 0.004% measure temperature. It can be seen that the error between the simulated and experimental data is the highest recorded to be 11.43% (this correspond to 6.91% of adiabatic temperature) in case 20, this can possibly be attributed to the local catalyst exhaustion. Hence the measured mean temperature is lower than that computed by the simulation. In all most all readings of the validation cases of the flow temperature (except for 16V) it can seen that the model predicts with a positive deviation to the sample mean. The average temperature deviation with respect to sample mean is 4.01% and 2.00% with respect to the adiabatic temperature. If the maximum sensor inaccuracy is consider then the average temperature deviation would result in 2.00% ± 0.3% with respect to the adiabatic temperature

	L/D	**Simulated**	**Measured sample mean**	**Deviation WRT sample mean**	**ΔT WRT T_{ad}**
	[-]	[kelvin]	[K]	[%]	[%]
Case 13V	0.459	383	367	4.36	1.63
Case 14V	0.459	325	306	6.21	1.93
Case 15V	0.459	344	326	5.52	1.83
Case 16V	0.459	345	340	1.47	0.51
Case 19V	0.459	324	308	5.19	1.63
Case 20V	0.459	325	321	1.24	0.41
Case 13V	1.818	914	880	3.86	3.45
Case 14V	1.818	912	874	4.35	3.86
Case 15V	1.818	860	840	2.38	2.03
Case 16V	1.818	853	899	-5.12	-4.67
Case 19V	1.818	655	611	7.20	4.47
Case 20V	1.818	663	595	11.43	6.91
Case 13V	3.091	-	944	-	-
Case 14V	3.091	-	900	-	-
Case 15V	3.091	-	912	-	-
Case 16V	3.091	-	951	-	-
Case 19V	3.091	-	929	-	-
Case 20V	3.091	-	942	-	-

Table 6.4: Overview of the flow temperature and the respective differences

The pressure comparison results between the model and experimental results are summarised in Table 6.5. The absolute pressure loss of the flow predicted by the model was compared with the experimental results and the sample mean, however the pressure losses in the system was smaller in magnitude comparative the roughness of the pressure measured. The difference in ΔP of the simulated data and experiment sample mean

results in a lower pressure loss in the simulated cases. However, the deviation is less than 1% of the flow pressure between the simulated and the experimental data. As the impact of modelled equations were discussed in the chapter 3, any variation in mass-flow of the experimental setup may add to the deviation of the modelled pressure losses. The massflow used in the model is determined based on experimental pressures of the HTP feed tank and catalyst bed inlet. In order to improve the accuracy the a massflow meter should be implemented, as this would eliminate any uncertainty of the flow rate. Considering the pressure roughness (ranging from 1.84 to 6.10%), this limits the scope to validate the pressure model. Hence to validate the accuracy pressure model the pressure roughness of the system relative to the pressure drop should be smaller.

To further validate accuracy of the pressure model, changes to the experimental setup are required. This can be achieved with increasing factors that contribute to a higher pressure drop, such that pressure losses are higher than the roughness experience by the catalyst bed. These factors include increasing the catalyst bed length, reducing the pellet diameter, shape of the catalyst bed [18] and the operating bed loading. From the analysis of all the cases and the summarised Table 6.5, it is visible that the flow pressure modelled are within the range of the measured experimental pressures, hence it can be used to approximate the pressure losses of the system. Considering the pressure model solely gives flow pressure and pressure losses along the catalyst bed and impacts of any other local affect that can results in pressure roughness. The roughness of the experimental pressure data in the experiments is possibly due to effects such as non homogeneous catalyst surface conditions (such as variation of active sites or activity of site) or possibly due to rapid phase change from liquid to gas.

Case	**ΔP Simulated** [bar]	**ΔP Experimental** [bar]	**Simulated pressure loss %** [%]	**Experimental pressure loss %** [%]	**Pressure roughness** [%]
Case 13V	0.289	0.749	0.542	1.40	[6.10, 5.58, 3.46]
Case 14V	0.290	0.685	0.543	1.283	[6.83, 6.96, 3.65]
Case 15V	0.312	0.539	0.404	0.677	[4.97, 4.35, 3.15]
Case 16V	0.310	0.380	0.40	0.49	[4.11, 4.85, 3.04]
Case 19V	0.34	0.36	0.33	0.35	[5.14, 4.52, 3.06]
Case 20V	0.33	0.53	0.32	0.55	[2.02, 2.26, 1.84]

Table 6.5: Overview of flow pressure losses of the simulated and experimental results and pressure roughness

In the validation process six sets of experimental data were compared with simulated results. The data consisted of pressure and temperature at three locations of the catalyst bed. From the comparison of simulated results with the experimental results it was found that model was able to predict temperature deviations ranging 0.41 to 1.93% of the adiabatic temperature at L/D 0.459. This results in an average deviation of 1.32% of the adiabatic temperature reached by the model (for 6 cases at L/D0.459). At L/D 1.818 temperature deviations ranged -4.67% to 6.91% of the adiabatic temperature with an average

of 2.68% for 6 tests. In all cases the model results showed that reaction was completed or exceeded 98% prior to reach L/D 3.091. This was validated with test video footage, showing the hottest region of the decomposition chamber was prior to L/D 3.091. The pressure data was compared with simulated results, the outcome show that pressure losses were small. However deviations were found to be less than 1% of the flow pressure between the simulated and the test data. Considering the overall pressure roughness measured and actual flow pressure drop in the catalyst bed, the flow pressure simulated in all cases are within the bounds of the measured data. However improvements to the pressure validation is evident, and some suggestions were discussed to increase the quality of test data for validation .

7

Simulation Results

The model developed was used to simulate the results for many cases to investigate the effects of each of the variables identified in the thesis questions. In order to perform the simulations, catalytic parameter based on Manganese Oxides are used from table 3.3. First the model results are presented and explained, afterwards simulations are compared to determine the impact of operational variables. The impact due change of pressure, feed concentration and massflow are discussed accordingly

7.1. Simulation Baseline Results

In order to show the model response to the inputs, a simulation case with certain parameters is chosen solely to explain the model outputs. The chosen parameters resemble the case 4 given in Table 3.4 in terms of massflow and pellet diameter Simulations were performed at standard feed temperature 298.15 [K] and a feed pressure of 30 [bar] with 87.5% HTP. The massflow was set to 67 [$g s^{-1}$] with a catalyst bed diameter of 29 [mm]. The selected massflow and catalyst bed diameter results in a bed loading of 101.44 [$kg m^{-2} s^{-1}$]. Pellet diameter of 1.59 [mm] and the catalyst bed chamber diameter is used to compute the void fraction of 0.3936. For future reference, the baseline inputs for simulation resulting from the aforementioned parameters will be regarded as 'Case 1R'.

First the model uses the input flow rate and concentration to establish the flow composition at each point of reaction progression going from 0% to 100%. The variation of the species due to reaction progression is shown in Figures 7.1 & 7.2 with respect to species molar flow rate and mass flow rate in the catalyst bed.

Parameter	Case 1	Units
Pressure	30	bar
Massflow	67	gs^{-1}
Inlet Temperature	296.15	[K]
HTP	87.5%	% [w/w]
Pellet Diameter	1.59	[mm]

Table 7.1: Case 1R model input conditions

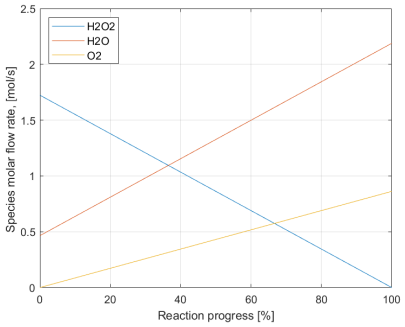

Figure 7.1: Variation of species by moles during the reaction of 87.5% HTP at a 67 gs^{-1} flow rate

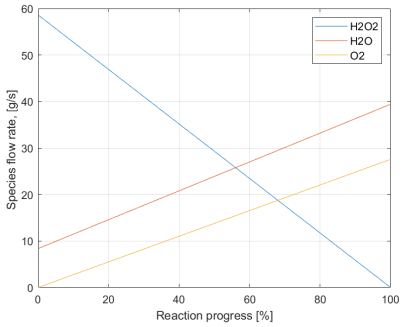

Figure 7.2: Variation of species by mass during the reaction of 87.5% HTP at a 67 gs^{-1} flow rate

7

The reaction progression along the catalyst bed gives insight to completion of the reaction with reference to the initial number of moles of H_2O_2 in the flow. The reaction progression distribution plot shows the completion of the reaction at each location of the bed, this is depicted in Figure 7.3. For a reacting HTP flow, the flow temperature along with the gas fraction profiles for H_2O & H_2O_2 are given in Figures 7.5 & 7.7. A superimposed Figure of the gas profiles and temperature profiles given in Appendix B Figure B.1. The reaction progressions distribution of the flow along the catalyst bed given in Figure 7.3 shows by the gradient the rate at which the react progress along the catalyst bed. Hence at the start the gradient increase steeply, due to the rise in temperature of the flow and the high initial concentration of the H_2O_2 in the flow. As the liquid H_2O begins to evaporate rapidly, the reduces the curve steepness (gradient) of reaction progression along the catalyst bed is seen. The increasing flow gas fractions reduce the H_2O_2 concentration, resulting a reduction of the curve steepness. The increase of the evaporation of H_2O_2 along with the loss of concentration of H_2O_2 in the flow once again slows the reaction progress along the catalyst bed. Finally as the two phase flow becomes completely gaseous (in Case 1R at about 3.21 [mm]) the reaction progression further reduces. The reaction progressions distribution plot given in Figure 7.3 and temperature progression plot given in Figure 7.5 can be translated flow temperature distribution. The simulation results are interpreted with distribution of flow temperature along the catalyst bed is given in Figure 7.6.

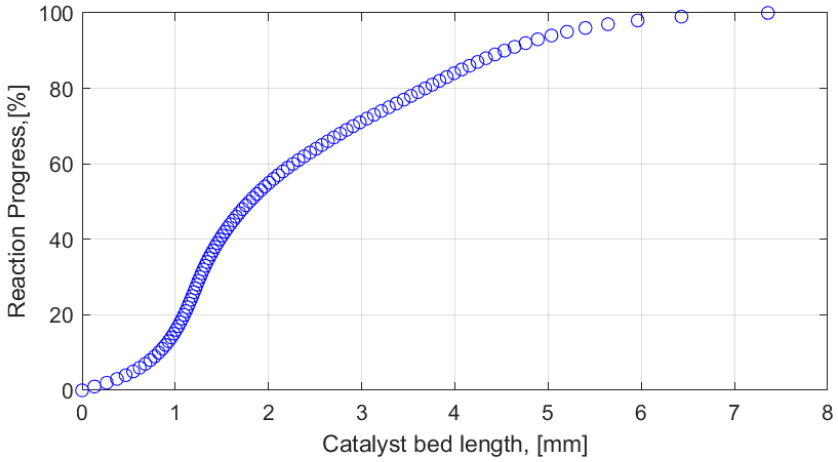

Figure 7.3: Reaction progress along the catalyst bed length (simulation Case 1R)

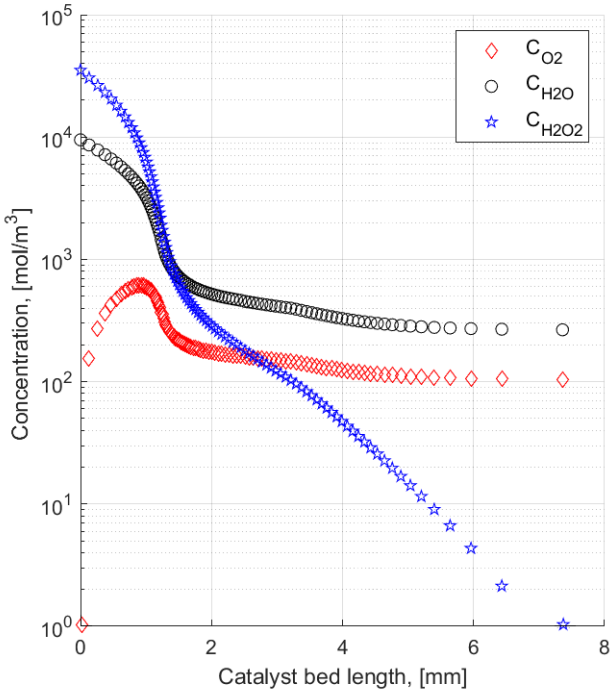

Figure 7.4: Molar concentration of flow species along the catalyst bed length (simulation Case 1R)

The flow specie concentrations along the catalyst bed length shown in Figure 7.4. It can be seen that the concentration of all species drop along the bed. For H_2O_2 the molar concentration reduces at a faster rate as its the reactant and undergoes decomposition. The molar flow rate of the reaction products O_2 and H_2O increases as the reactions progress as shown in figure 7.1, however as temperature increases and the species state change from liquid to gas the volumetric flow rate increases resulting in declining concentration. Initially O_2 increases due to evolving oxygen from the reaction, however as the flow phase changes and temperature increase the O_2 concentration drops.

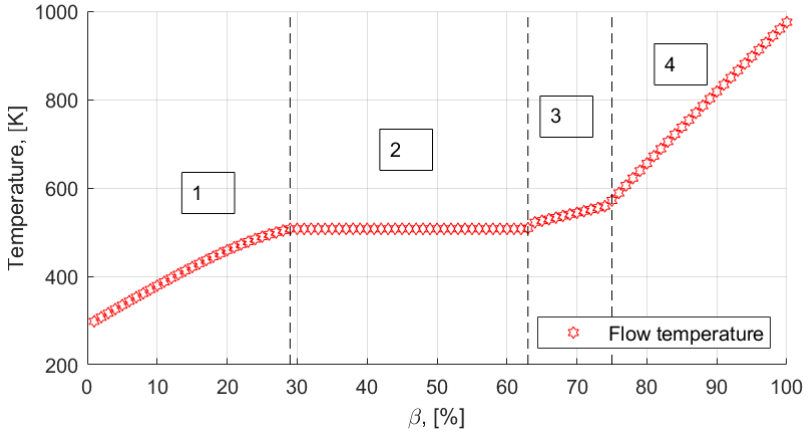

Figure 7.5: Flow temperature resulting from 87.5% HTP decomposition (simulation Case 1R)

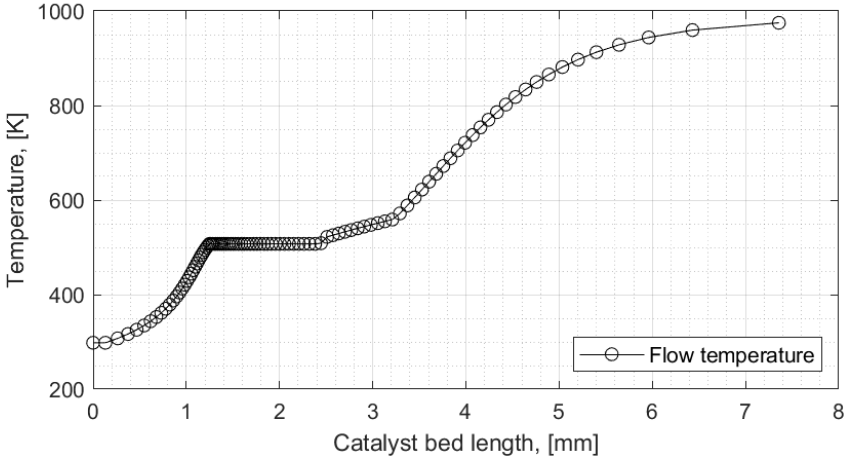

Figure 7.6: Flow temperature resulting from 87.5% HTP decomposition (simulation Case 1R)

The temperature profile can be sectioned to four stages, depending on the flow composition and condition, depicted in the Figure 7.5. At initial stage of the flow reaction raises temperature and the gas fraction, this is shown in stage 1. The reacting flow increases in temperature, this can be seen in 7.6. At start a rapid increase of temperature can be seen, this is due to high initial concentration of H_2O_2 species. The flow through the catalyst bed reaches saturation conditions of H_2O at about 1.25 mm into the catalyst bed. At 30 bar of pressure the saturation temperature of water is 507.4 K is reached at 29 % of the flow is decomposed. At stage 2 the quasi isothermal vaporisation due to H_2O is depicted, where species of H_2O & H_2O_2 transit for liquid to gas, a rapid phase change occurs for H_2O in the flow and can be seen in Figure 7.8. As the reaction progress to 63 % the water has completely evaporated and majority of H_2o_2 have decomposed (63% of H_2O_2 has decomposed). Hence, the H_2O dry out point corresponds to 3.29 mm in the catalyst bed, this can be seen as gas fraction of H_2O goes to 1 in Figure 7.8. There on, at stage 3 the flow temperature rises, evaporation of H_2O_2 is increase due to local flow conditions (partial pressures and temperature). At 75 % of the reaction progression, the flow is completely in gas phase. Stage 4 begins at bed length of 3.29 mm. The complete gas phase is depicted in stage 4 where flow is all in gas phase shows a asymptotic rise in temperature as H_2O_2 decomposes.

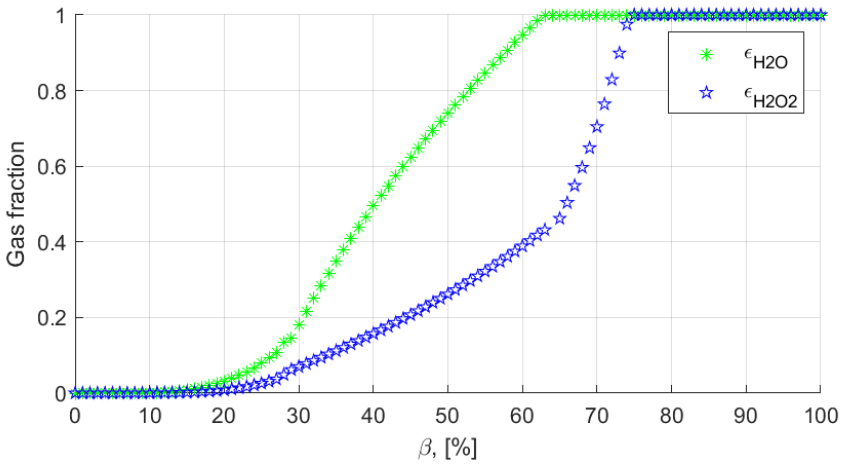

Figure 7.7: Fraction of gaseous flow species at 20 bar pressure (simulation Case 1R)

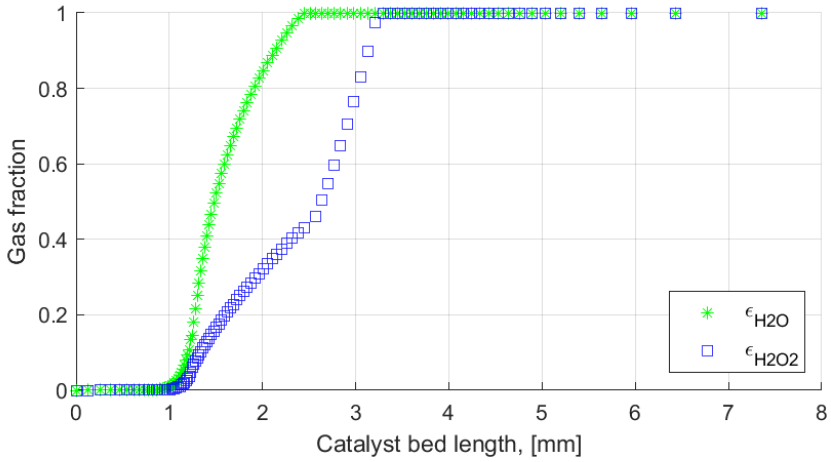

Figure 7.8: Fraction of gaseous flow species along the catalyst bed (simulation Case 1R)

The gas fraction is ratio gas state to the total number of a certain species (either H_2O or H_2O). The gas fraction of H_2O shown in the Figure 7.7 accounts for newly formed gaseous H_2O_2 in the decomposition process when saturation condition of H_2O is met. In the first stage shown in the temperature profile, the evaporation of H_2O and H_2O_2 slowly increases, this is mainly as result of the operational pressure. Hence stage 1 is prolonged till the saturation temperatures of H_2O is met, after which a rapid increase in gas fraction of H_2O can be seen in stage 2. At this stage the evaporation of H_2O_2 is not as rapid as water (due its higher saturation temperature of H_2O_2). Once all the H_2O has evaporated there is rapid evaporation of liquid H_2O_2 along with rise of flow temperature, this is stage 3 (occurs between 2.51 and 3.29 mm bed length). The end of stage 3 all H_2O_2 has evaporated and dry out condition are met. The Figure 7.8 shows the gas fraction reaching 1 at 2.51 mm of bed length for H_2O in the flow and the gas fraction for H_2O_2 reaches 1 at 3.29 mm of bed length (this corresponds to 63% and 75% of reaction progression of the flow).

The Figures 7.9 & 7.10 shows the pressure profile and pressure losses in the catalytic bed. The flow pressure losses increases along the catalyst bed as flow decomposition progress. As the flow decomposes the temperature increases, density of the flow decrease but the increase in flow velocity causes the pressure drop to rise. The pressure drop in the two phase region of the flow (up to 3.29 mm in length of the catalyst bed) is 0.054 bar and total pressure drop 0.321bar the reach. The majority of the pressure loss is contributed by the gas phase region, due to the increase in flow velocity.

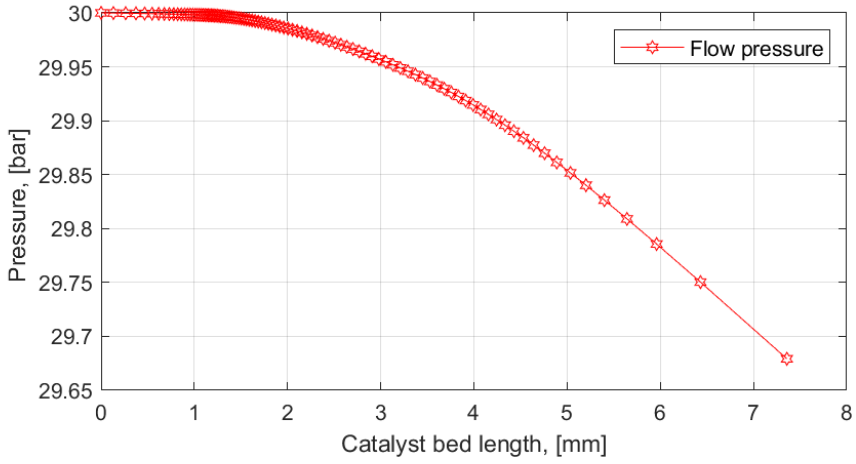

Figure 7.9: Flow pressure along the catalyst bed (simulation Case 1R)

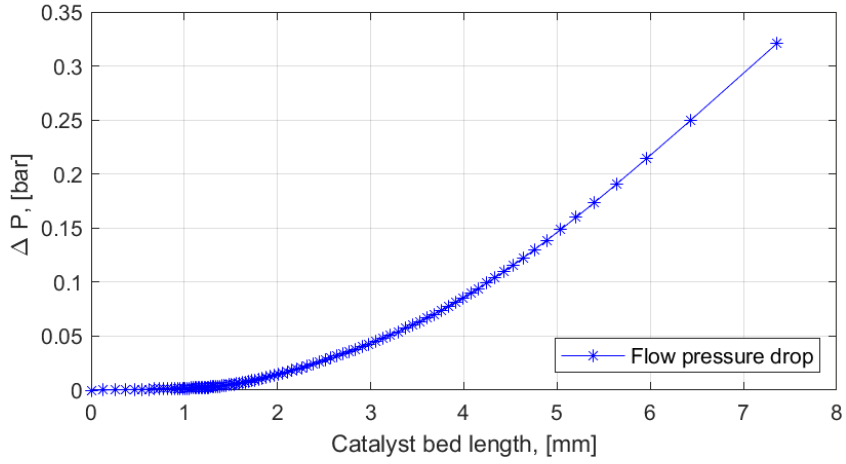

Figure 7.10: Pressure losses along the catalyst bed (simulation Case 1R)

7.2. IMPACT ON PRESSURE VARIATION

The impact of operating pressure on the HTP flow development of the catalyst bed was investigated. This was done by comparing multiple simulation results with one pressure as the only variable ranging from 10 to 100 [bar]. It is understood from the theories employed in model development that there is a direct correlation between the operating pressure and saturation conditions of the flow. Hence the evaporation profiles of H_2O_2 & H_2O has an impact of the reaction progression. Therefore it is logical that the HTP concentration have an impact on the evaporation profiles, as the H_2O_2 & H_2o have different saturation conditions. Simulations were performed with varying pressure from range of 10 [bar] to 100 [bar], along with HTP concentration to capture the affects. Simulations condition was set to 87.5% HTP with an inlet temperature 298.15 [K]. The massflow was set to 67 [gs^{-1}]. The resulting in a bed loading of 101.44 [$kgm^{-2}s^{-1}$] and a catalyst bed void fraction of 0.3936. These model operating conditions with variable pressure will be referred to as Case 2R (Pressure varying from 10 to 100 [bar]).

The effect of pressure on the catalytic bed length required to complete the reaction was investigated with case. This was done by performing simulations in the aforementioned conditions (Case 2R) and vary the operating pressure. The results show in Figure 7.11 on reaction progression distribution along the catalyst bed. The reaction progression curves show deviation from each other at between 20- 25 % progress. The deviation of reaction progression is association to the rate of gas evolution of the flow, the evaporation fraction of the reacting flow varies with temperature.

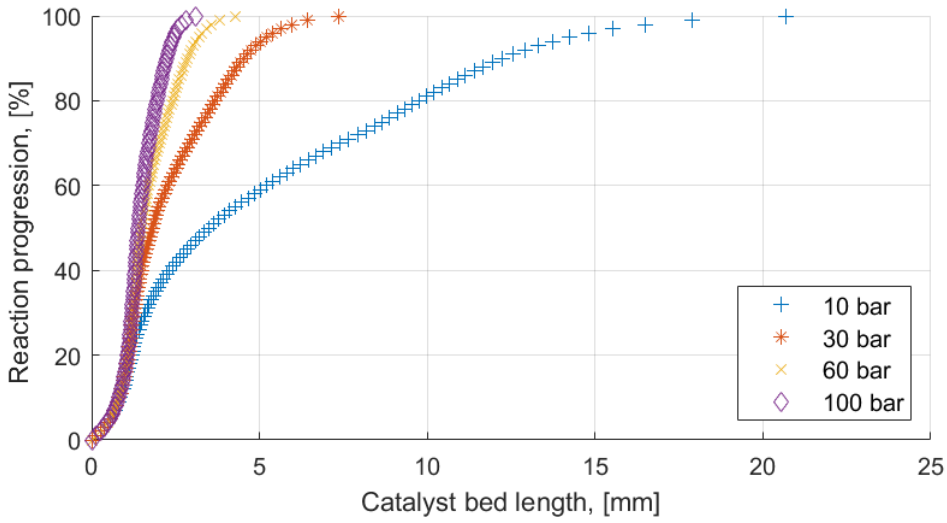

Figure 7.11: Reaction progression along the catalyst bed (simulation Case 2R with variable pressures)

The deviation of the catalytic bed length is calculated with respect to the reaction progression curve at the 10 bar. The deviation is shown as a percentile of the complete

decomposition length at 10 bar. The deviation plot clearly shows that visible deviation starts at a 20% reaction progress and increases til the phase transition is complete. This is related to the evaporation, because greater the operating pressure resulting deviation is higher in magnitude, the fraction profiles are shown in in Figure 7.14. Once the flow is in gas phase the deviation significantly increases. The rate at which the deviation increases in the gas phase are higher with pressure. This means that at higher pressures the length required for gas phase decomposition reduces. The deviation at the end reaction shows that at higher pressures a catalyst bed lengths are required. This remains true to achieve decomposition progression above 20 % (since the effect of the pressure is strongly correlated to the gas fraction in the flow). However the significance of increasing pressure on the catalyst bed design is dependent on the progression of decomposition desired and the operating pressure (eg: In the case of two identical catalyst beds, in order to have 60 % decomposition at 100 bar the catalyst bed only requires 17.85% the length than the catalyst bed operating at 10 bar of pressure).

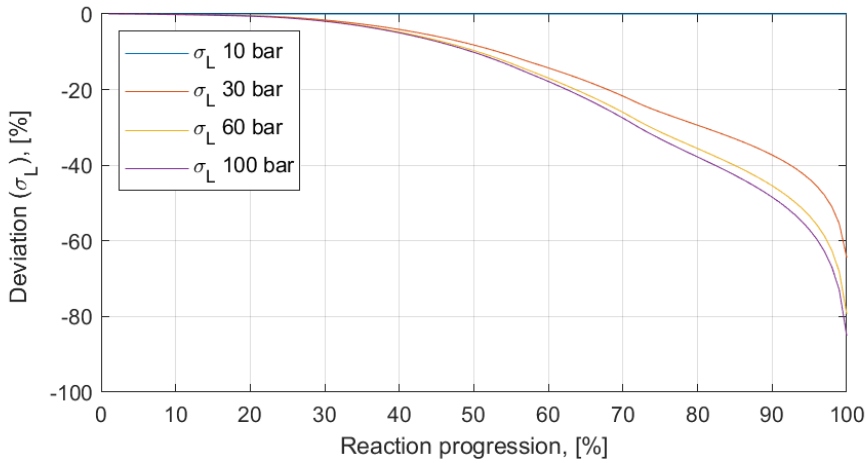

Figure 7.12: Deviation of length with respect to 10 bar reaction profile

It can be seen from the model results that pressure affects the flow development in the catalytic bed, increase of the pressure prolongs the two phase region of the catalyst bed and reduces the gas phase thereby impacting the length required for complete decomposition. The length of the catalyst bed where complete decomposition is achieved for Case 2R conditions are tabulated in Table 7.2.

Pressure	Length at β 98%	Length at β 100%
10	16.49 [mm]	20.67 [mm]
30	5.96 [mm]	7.36 [mm]
60	3.57 [mm]	4.27 [mm]
100	2.67 [mm]	3.01 [mm]

Table 7.2: Decomposition flow advancement on catalyst bed length

The gas fraction shows the that flow transition form liquid to gas is affected by the pressure as depicted in Figure 7.14. As operational pressure of the catalytic bed rises the phase transition is prolonged. The H_2O_2 dry out location of the catalyst bed is given as follows;

- 7.66 mm at 10 bar
- 3.21 mm at 30 bar
- 2.28 mm at 60 bar
- 1.92 mm at 100 bar

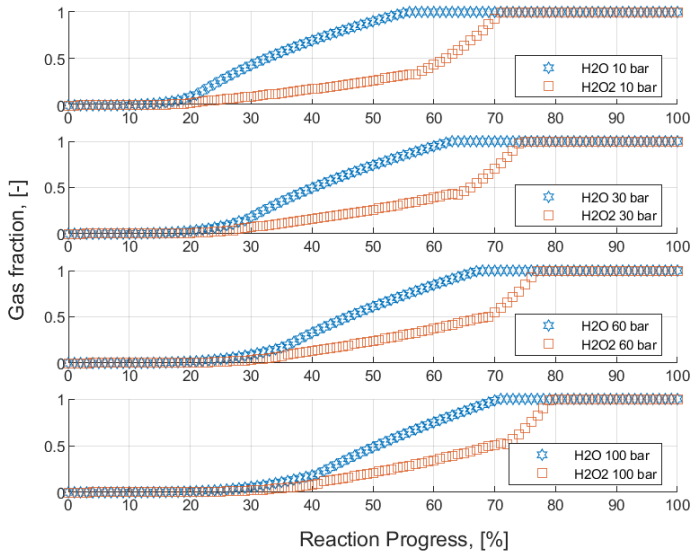

Figure 7.13: Gas fraction development with reaction progression (simulation Case 2R with variable pressures)

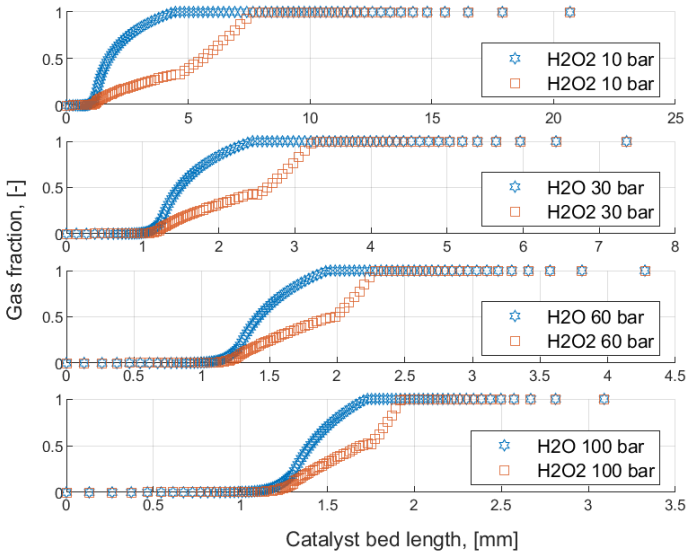

Figure 7.14: Gas fraction development along the catalytic bed (simulation Case 2R with variable pressures)

With increasing pressure the saturation temperature of liquid H_2O & H_2O_2 increases, this is captured by the equations 2.25 & 2.26 used in the model. This effect can be seen in Figure 7.14 and more clearly on Figure 7.15. It is notable that increasing pressure increases the saturation temperature and it is shown in Figure 7.13 that at low pressure the flow gas fractions of H_2O & H_2O_2 evolves more than at higher pressure at given reaction progression. Hence the dry out point of the reaction (flow is pure gaseous) is reached at greater reaction progression as pressure increases. At higher pressure the volumetric flow reduces resulting in higher flow concentration on the catalyst surface. This process also decreases the evaporation region of the catalyst bed (showing it needs less catalyst bed length to evaporate the fluid at higher pressure) due to lower volumetric flux of the flow at higher pressure.

The temperature profile along the catalyst bed shown in Figure 7.15 supports the findings on effect of pressure on catalyst. The temperature profile shows increasing temperature till saturation conditions are met, hence the impact of increasing pressure on the increase of saturation temperature is shown. These results supports the finding of Williams et al[43] on the approach to realises temperature of the reaction. Once saturation conditions are met, the phase transition happens, in the case of increase pressure the catalytic bed length for phase transition decreases. The temperature profile shows the gas phase decomposition is promoted at increasing pressure the gas. The impact of pressure is also capture in the two phase flow region, when looking at the temperature profile below saturation shown in figure 7.16, showing faster rise in temperature with the increase in pressure.

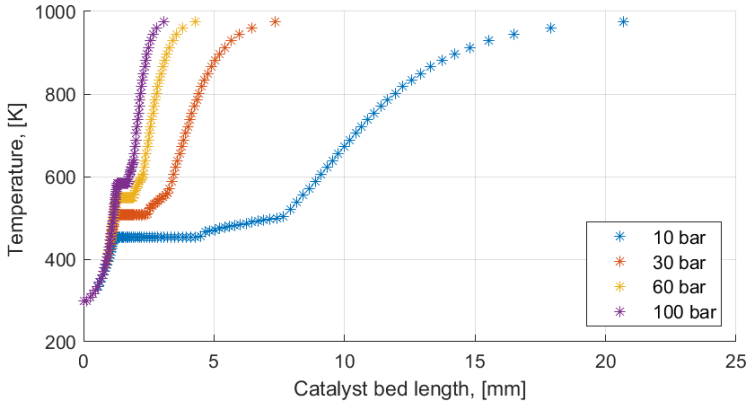

Figure 7.15: Flow temperature along the catalytic bed (simulation Case 2R with variable pressures)

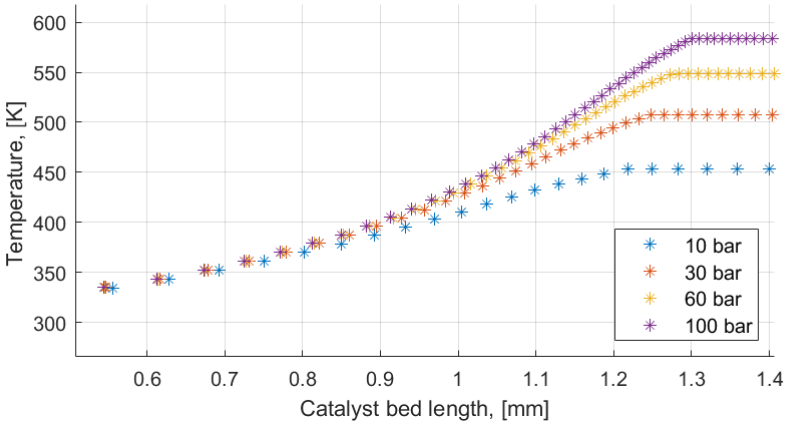

Figure 7.16: A close up of initial flow temperature along the catalytic bed (simulation Case 2R with variable pressures)

When increasing pressure, the reaction in liquid phase (predominantly liquid phase of a two phase flow) doesn't seem to show any effect on pressure. This is because increasing pressure doesn't have an effect on liquid reactions, this means that the increasing pressure does not alter the concentration of the liquid. However it plausible that an effect of liquid compressibility exists, in this work the effect of liquid compressibility is considered negligible (isothermal compressibility of HTP is typically about 26.514×10^{-12} [bar^{-1}] [29]). The gas phase decomposition in the catalytic bed is promoted by increasing pressure. With increasing pressure the probability of molecular collision on the catalytic surface increases. Hence increasing pressure increase gas phase flow concentration aiding to the reaction progression, this can be seen with Figure 7.11, the gradient of

the gas phase slope increases with pressure. Above 80% reaction progression of the flow in simulated results in Figure 7.11 are all gaseous and considerable amount of catalytic bed length variation is present in the gas phase due to variable pressures. The difference between the aforementioned bed length for complete decomposition and the dry out position of the catalyst bed gives the length of the catalyst bed occupied by pure gaseous flow. The catalyst bed length required for the pure gaseous flow to complete decomposition are shown listed below ;

- 13.01 [mm] at 10 [bar] pressure
- 4.15 [mm] at 30 [bar] pressure
- 1.99 [mm] at 60 [bar] pressure
- 1.08 [mm] at 100 [bar] pressure

The above shows that from the majority of the catalyst bed length is required for the decomposition of gas phase H_2O_2. Increasing pressure decreases the length required for gaseous H_2O_2 decomposition, as the volumetric flow due to the pressure is reduced (gas phase H_2O_2 flow concentration increases with pressure). The overall catalytic bed length required for 98% reaction progress is shown in figure 7.17

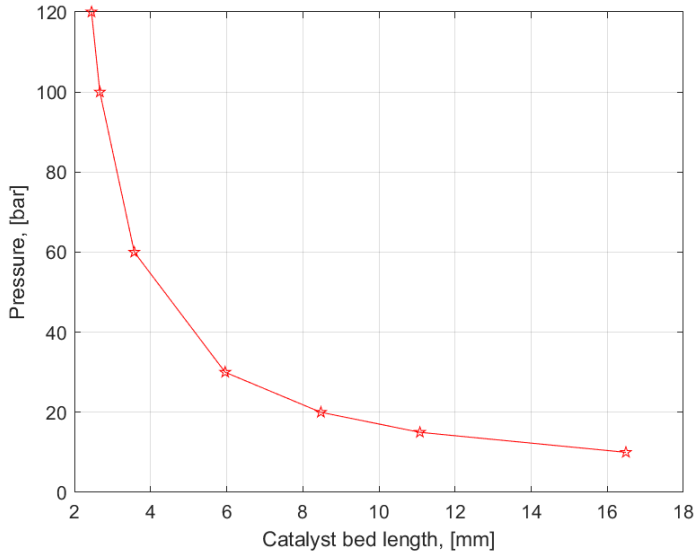

Figure 7.17: Catalyst bed length required for 98% reaction progress (simulation Case 2R with variable pressures)

The impact on operating pressure on a catalyst bed on a given set of conditions defined by Case 2R was assessed. The catalytic bed length required for decomposition is depen-

dent on the pressure. Increase in operational pressure delays the flow phase change with respect to the reaction progression, the volumetric flow rate decrease (due to gaseous flow) with increasing pressure. Thereby, the local flow concentration on the catalyst is higher promoting decomposition resulting in shorter catalyst bed length to complete the reaction of the flow.

7.3. EFFECTS OF FEED CONCENTRATION

The simulations were performed with Case 1R input parameters, with an inlet temperature 298.15 [K]. The massflow was set to 67 [gs^{-1}]. The resulting in a bed loading of 101.44 [$kgm^{-2}s^{-1}$] and a catalyst bed void fraction of 0.3936. These model operating pressure was set to 30 bar. The feed concentration was varied from 80%, 87.5%, 90%, 95% & 100% HTP. The impact was assessed at a single operating pressure of 30 bar and feed temperature of 298.15 K. With increasing in the concentration of HTP the adiabatic decomposition temperature reached at the end of the reaction is tabulated in Table 7.3.

HTP [w/w]	Adiabatic temperature
100 %	1282 K
95 %	1159 K
90 %	1036 K
87.5 %	975 K
80 %	790.61 K

Table 7.3: Adiabatic decomposition temperature $T_{in} = 298.15K, P = 30bar$

The impact of changing the concentration was analysed on the reaction progress on the catalytic bed length required . This was done by vary the input flow concentration. The results shown in Figure 7.18 on reaction progression distribution along the catalyst bed. With the increase of HTP concentration, the rate of reaction progression is promoted. A considerable difference can be see over 70% of reaction progress, this is due to the decreasing of concentration of H_2O_2 the volumetric flow.
The difference of the gas fraction of the flow species is shown as the reaction progress along the catalyst bed 7.19. As concentration of the feed is lowered (from 100% to 80% HTP) it is shown that the phase transition is prolonged and dry out condition of the flow is met at greater reaction progress. This effect is due to a lower flow temperature reached as a consequence of feed HTP concentration at a given level of reaction progress. The gas fraction of species generated is dependent on temperature and pressure, in this comparison the pressure is held constant and the flow temperature is a product of the reaction progress and the selected feed concentration. It is shown in Figure 7.20, as the feed concentrated increases the reaction progress faster and the required catalyst bed lengths are shorter.

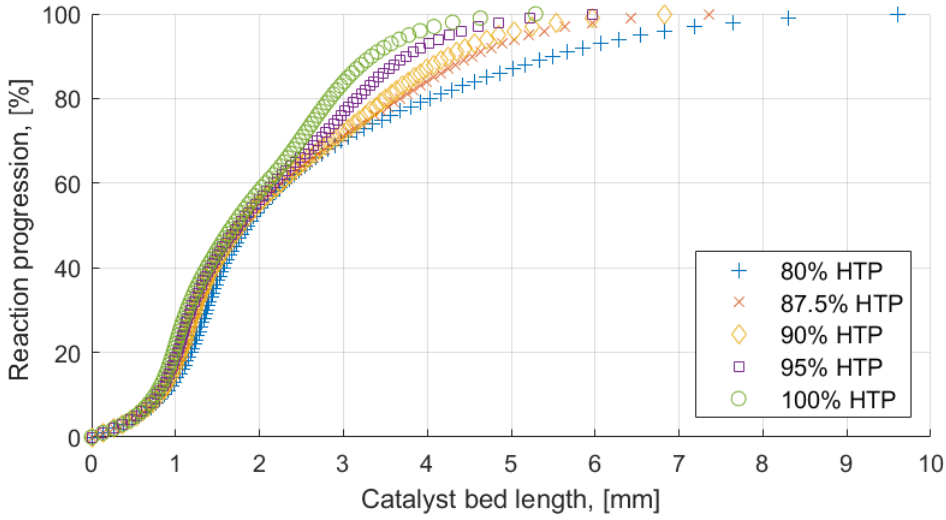

Figure 7.18: Reaction progression along the catalyst bed (simulation Case 2R with pressure of 30 bar)

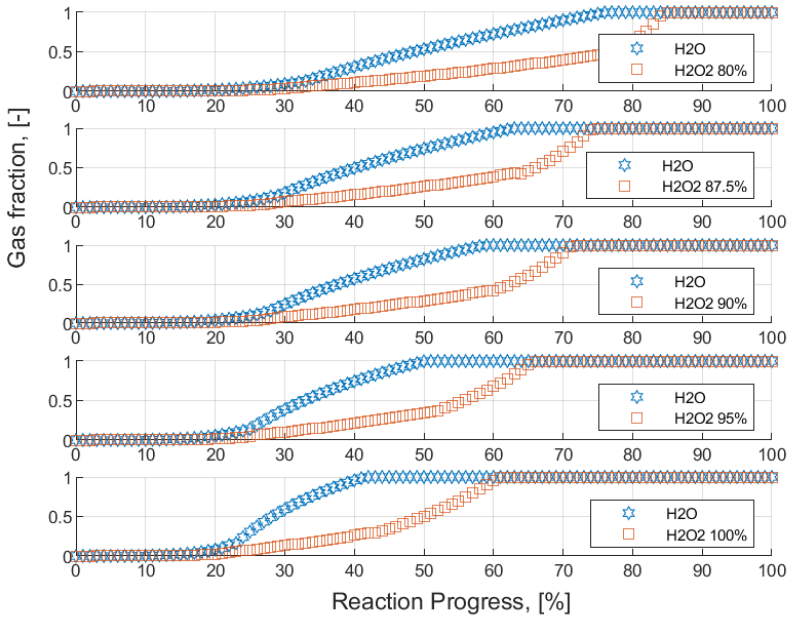

Figure 7.19: Gas fraction of H_2O & H_2O_2 as reaction progress

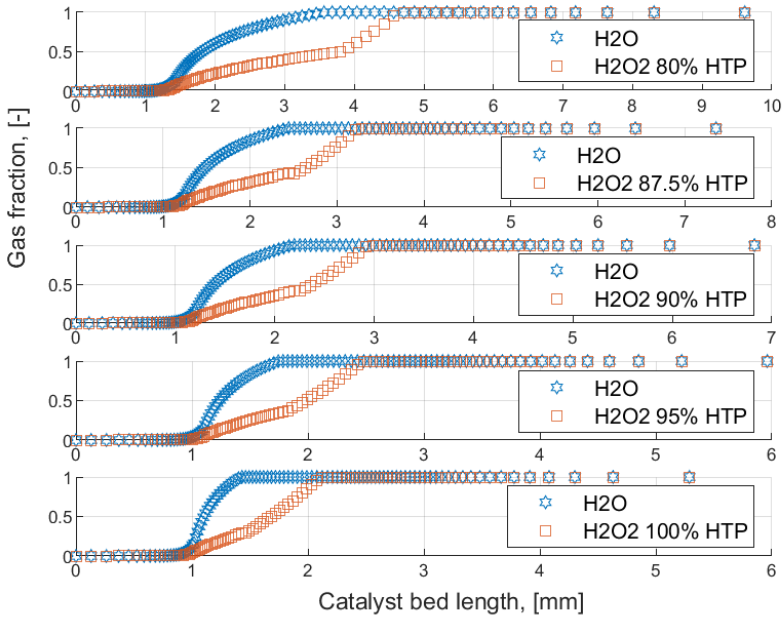

Figure 7.20: Gas fraction of H_2O & H_2O_2 along the catalyst bed

The flow temperature profiles along the catalyst bed length is shown in Figure 7.21, the variation of the HTP concentration shows an effect on the required catalyst bed length to achieve decomposition. The lower feed concentration, greater the catalyst bed length requirements, the cause of this is concentration of H_2O_2 on the catalytic surface and the temperature realised when at given progression reaction. A lower feed concentration reduce the rate of reaction, hence the reactions is less fast. Increasing the feed concentration also increases the flow temperature realised at given reaction progress yielding a higher reaction rate. The increase of flow concentration, causes the faster reaction rate, seen by the steeper gradient in Figure 7.18 & 7.21 at the start of the reaction. The dry out conditions are reached at 60% reaction progress with 100% HTP and over 80% reaction progress with 80% HTP. Even with the faster transition to a gas phase at a higher feed concentration, the increase of the temperature of the gas phase flow speeds up the reaction (seen by the steeper gradient in Figure 7.18 & 7.21). Hence the requirement of a catalyst bed length is shorter with increase feed concentration.

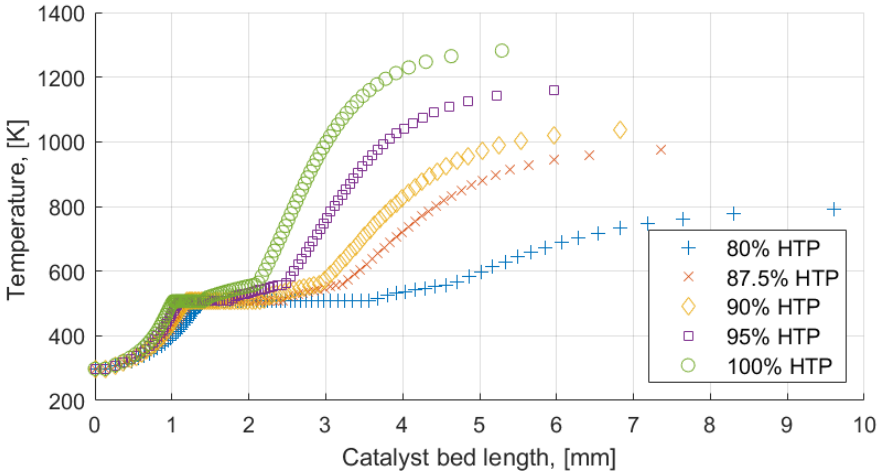

Figure 7.21: Reacting flow temperature over the catalyst of H_2O & H_2O_2 along the catalyst bed

7.4. COMBINED EFFECT OF PRESSURE AND CONCENTRATION

In sections 7.2 and 7.3 the effects of the pressure and feed concentration was discussed. The increase both these parameters has a positive effect on the reaction, the reaction is faster resulting in shorter catalyst bed length requirements. In order to identify the combined effect simulations were performed by varying both parameters. The figure 7.22 shows the reaction length required to achieve 98% decomposition.

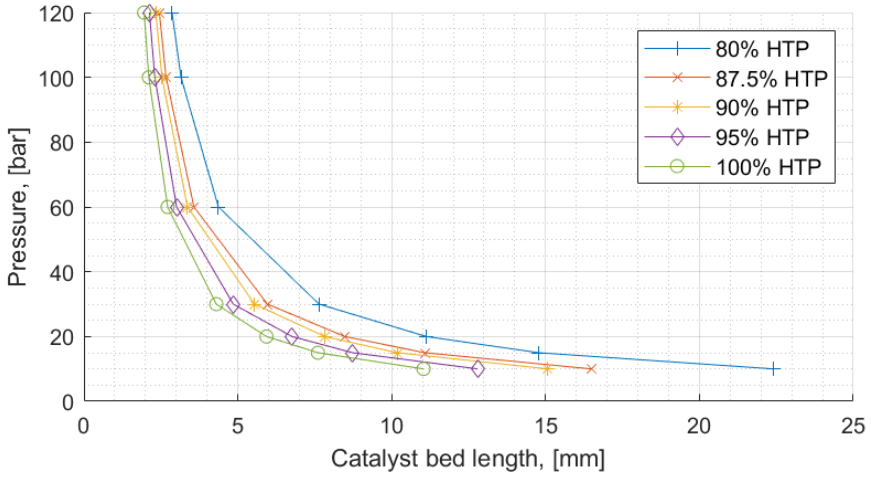

Figure 7.22: Pressure and HTP concentration impact on catalyst bed length required for 98% reaction progression

7.5. EFFECT OF INCREASING MASSFLOW

The bed loading parameter with the units [$kgs^{-1}m^2$] is dependent on the massflow rate through fixed bed (constant cross sectional area). The bed-loading parameter can be varied with the massflow or varying the cross sectional geometry of the catalyst bed. In this analysis, the massflow was varied to result in a bed loading range of 25 - 200 [$kgs^{-1}m^2$]. The impact of changing the bed loading was assessed on simulations set with fixed operational pressure of 30 bar and a set HTP feed concentration of 87.5%. The impact of bed-loading is shown in Figures 7.24 & 7.23. The increase of bed loading parameter increase the catalyst bed length required for decomposition for given catalyst. Hence varying the massflow in the simulation has an impact on the volumetric flow through the catalyst bed, thereby impacting the catalyst bed length required to progress in decomposition of the flow.

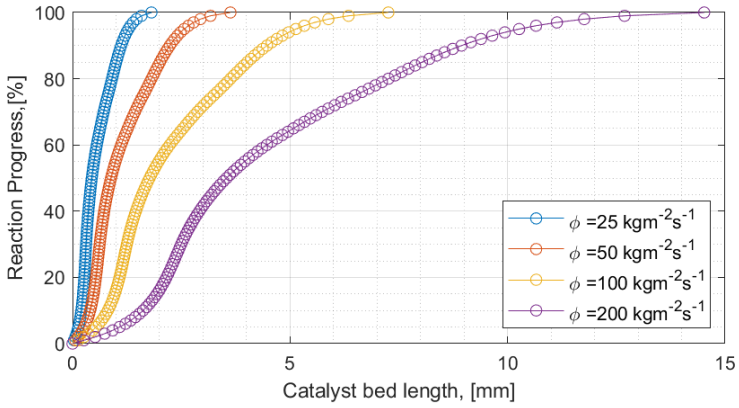

Figure 7.23: Reaction progression along the catalyst bed length for varying bed-loading

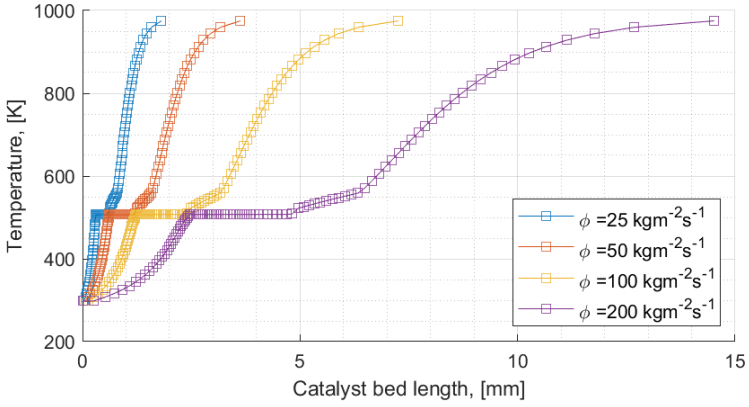

Figure 7.24: Flow temperature along the catalyst bed length for varying bed-loading

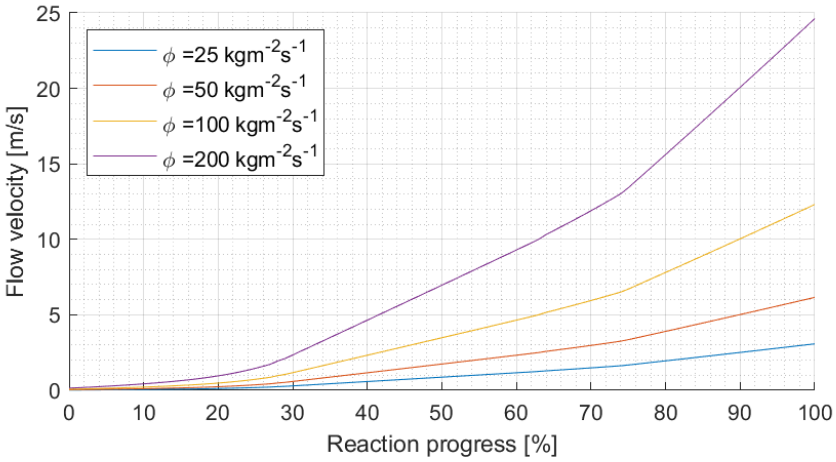

Figure 7.25: Flow velocity for varying bed-loading

The Figures 7.24 & 7.23 shows at higher bed-loading the flow penetrates quicker through the catalyst bed, this can be seen at a certain reaction progress the catalyst bed length required to realise the level progression is greater at higher bed-loading. Similarly, at low bed-loading the reaction progression is achieved at an a early catalytic bed length. This can be reasoned with the increasing flow velocity due to the increase of the bed-loading as shown in Figure 7.25. As the temperature of the flow is dependent on the reaction progress achieved by the flow. The temperature profile also shifts further in the catalyst bed at higher bed-loading. The table summarises the required bed length to reach the flow dry out condition and 98% reaction progress at varying bed-loading.

Bed-loading [kg s^{-1} m^2]	**Dry out location** [mm]	**Catalyst bed length for 98% Reaction Progress** [mm]
25	0.79	1.47
50	1.58	2.94
100	3.17	5.88
200	6.33	11.76

Table 7.4: Catalyst bed length required to reach dry out conditions and 98% reaction progress at varying bed-loading levels

Finally, in the process of assessment of the simulated data, two other parameters that were found to have an influence on the flow development in catalyst beds. These parameter include the chamber diameter and the pellet diameter. They both have their individual contribution to the flow development. However they are linked by void fraction of the catalyst bed. Hence the flow variations are mainly due to change bed void

fraction, considering the void fraction of pellet bed is coupled by the ratio of decomposition chamber diameter and pellet diameter, it is more practical (in an engineering sense) to consider the affects of these two parameters individually. Though these two parameters were not intended to be investigated in this thesis, as it was not defined in the research questions, their impacts to flow development process in the catalyst bed is relevant. Hence two figure 7.26 and 7.27 are shown to summarise the findings with Case 1R inputs (with varying pellet diameter and chamber diameter).

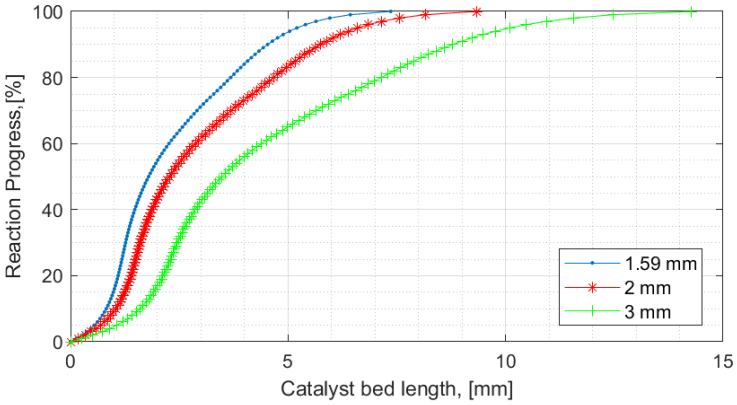

Figure 7.26: Reaction advancement at various pellet diameters

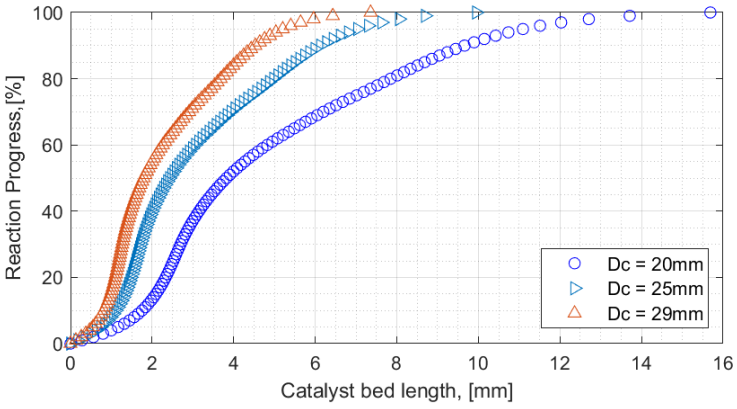

Figure 7.27: Reaction advancement at various chamber diameters

Chamber diameter	Pellet diameter	Void fraction	Length at 98% β	Bed laoding
[mm]	[mm]	[−]	[mm]	[$kgs^{-1}m^2$]
29	1.59	0.3936	5.96	101
29	2	0.3984	7.56	101
29	3	0.4102	11.56	101
20	1.59	0.4020	12.71	213
25	1.59	0.3966	8.06	136

Table 7.5: Case 1R model input conditions

Over 50 simulations were performed, the results were compared and analysed to find the affects of operational parameters on the the catalyst bed. The primary operation conditions focused in the assessment were catalyst bed operating pressure, feed HTP concentration, and massflow. The pressure and feed concentration were found to positively impact the reaction progression showing required catalyst bed length to complete the reaction to be shorter. However, increasing massflow to the catalyst bed showed that the required bed length for reaction to be greater. During this investigation other parameters that were found to have an impact on flow development in catalyst beds, these were pellet diameter and decomposition chamber diameter. They are both considered design variables and not operational variables. It was found the varying these parameters would results in changes to the flow advancement, as both these parameters govern the void fraction of a pellet catalyst bed. Increasing chamber diameter, results in shorter length required for the catalyst bed. The increase of pellet diameter results in longer bed required for the same level of decomposition.

8

Conclusion & Recommendations

The purpose of this research was to 'Make recommendations on pellet based catalytic bed length for high test peroxide decomposition chambers by means of a High Test Peroxide decomposition model to determine the flow development in the catalyst bed'.

The goal of this thesis was met in this study. A numerical model was developed to simulate HTP decomposition in catalyst beds. The model is capable of determining the flow properties including flow temperatures and pressures in the catalyst bed. The simulated results from the model demonstrated the ability to determine the impacts of operational variables, such as massflow rate, pressure and HTP concentration on the catalyst bed length. The model was found to be capable of predicting flow distributions up to 98% of the reaction progress.

An increasing massflow rate has the same impact as increasing the bed loading on a fixed diameter catalyst bed. Hence higher bed loading or massflow rates requires a longer catalyst bed for decomposition. Another aspect is the increase of flow velocity due to increase of bed loading requires a larger catalyst bed length. Based on a Manganese Oxide catalyst, and a bed loading of 200 [$kg\,s^{-1}\,m^{-2}$] the required bed length is 11.76 [mm] and bed length of 2.94 [mm] for a bed loading of 50 [$kg\,s^{-1}\,m^{-2}$]. However excessive reduction of flow rate or bed loading could increase the risk of feed system coupled instabilities, this was observed with tests performed at low flow rates. The variation of feed concentration was investigated, with HTP of 80%, 87.5%, 90%, 95% & 100% concentrations. The increase of concentration results in a higher adiabatic temperature ranging from 791 [K] for 80% HTP to 1282 [K] for 100% HTP. The results showed an acceleration in reactivity with the use of higher concentration HTP. This was primarily due to an increase of H_2O_2 species in the flow, as the flow decomposes a higher thermal gradient is present with the increase of HTP concentration. The greater the concentration of the feed HTP,

the earlier the dry out conditions are met in the catalyst bed. The gas phase decomposition is prolonged with a low concentrated feed (due to lower flow temperature and H_2O_2 concentration). Hence for a higher the HTP concentration, a shorter catalyst bed is required. It was shown that catalyst bed length required ranged 7.64 [mm] for 80% HTP to 4.85 [mm] for 95% HTP to achieve 98% decomposition progression. The effect of variation in pressure was found to be significant on the decomposition on the gaseous flow. The effect of pressure was captured In the two phase flow and pure gaseous flow. Increasing pressure causes the local flow concentration to increase (due to gas fraction of the flow), promoting decomposition. The dry out conditions are reached much earlier in the catalyst bed. As the flow advances to gas phase in a higher pressure, the gas phase decomposition is promoted resulting in a shorter catalyst bed length. Hence an increase of pressure enables to achieve a shorted catalyst bed. It was shown that use of 10 bar pressure would require 16.5 [mm] catalyst bed length to achieve 98% decomposition in contrary a 30 [bar] operating pressure yielded a bed length of 6 [mm].

The model was verified by comparing the model to other models in literature, this showed good agreements, with differences ranging from 4% to 14% of catalyst bed length for 98% completion decomposition (the model consistently showed a shorter bed length is required than predicted by Jung et al). A test setup developed by Dawn Aerospace was used to perform experiments, the experimental data were used to validate the model. The experimental data sets consisted of flow temperatures and pressures. The flow temperature simulated shows agreements with the experimental results with deviations ranging from -4.67% to 6.71% of adiabatic decomposition temperature reached by the model. The overall average deviation was 2% of adiabatic decomposition temperature. In all cases it was validated that the reaction was completed or exceeded 98% prior to reaching a L/D 3.091. The model predicted a lower pressure loss than the experimental average, but the differences between the two reduced with higher operating pressures (as pressure roughness reduced). The deviations between the simulated pressure loss and measured pressure loss was computed to be less than 1% flow pressure. However, the pressure roughness of the system was larger than the pressure drop, and the simulated pressure was still within the bounds in all the validation cases.

Finally it can be concluded that the model is capable of translating the user input to sensible outputs such as distribution of flow pressure, temperature, concentration, gas fractions and other flow characteristics over the length of the catalyst bed. With accuracy of the model identified by validation process, it has been demonstrated that the model is reliable when producing catalyst bed length estimates. Hence this model can be applied in the development process of catalyst beds and can translate design requirements into design choices and accelerate the development process of catalyst bed

Some recommendations can be made to improve the overall accuracy of the model. It is strongly recommended to use a massflow measurement in the test setup, as this would enable to provide accurate massflow reading, inaccuracies in massflow prediction can occur particularly in transient pressure conditions. In this work, steady pressure data were sampled from test data to derive massflow rates, however incorporating a massflow meter would enable the use of test data with less stringent requirements on sampled test

data. Hence having accurate inlet flow conditions can lead to better representation of the simulated results and increase the precision of the model validity. The simulated data showed that the maximum temperature was reach prior to the end of the catalyst bed used in the test. It is highly recommended to increase the massflow rate to the catalyst bed and further perform test such that maximum temperature region is induced forward and towards the temperature sensor placement at $L/D = 3$. This would enable to record the maximum flow temperature measurements in the experiments and assess the deviation from the simulated adiabatic temperature, this would assist to quantify if the heat transfer modifications proposed below are required.

To further develop the model, a heat transfer capability should be added to the model. Heat transfer from the evolving flow to the external surface boundary such as decomposition chamber casing. Capturing this in the model would aid to simulate results with thermal losses of the flow due to heat transfer to the surroundings. In a design perspective decomposition chamber wall temperature can be approximated, with such efforts to help in material selection and sizing. Similarly adding heat transfer from the pellet bed and the flow, where heat is transferred via the substrate from the hotter regions to the cooler regions of the catalyst bed, might aid to improve the results found in this work. Finally, the modelling approach used in this thesis for HTP decomposition in catalyst beds could be further developed to other mono propellants, such as Ammonium Dinitramide based or Hydroxylammonium Nitrate based green monopropellants.

BIBLIOGRAPHY

[1] European Parliament and Council. "registration, evaluation, authorisation and restriction of chemicals framework ". https://ec.europa.eu/environment/chemicals/reach/reach_en.htm, 2019. Online; accessed 22 Nov 2020.

[2] Sungyong An, Jungkun Jin, Jeongsub Lee, Sungkwon Jo, Daejong Park, and Sejin Kwon. Chugging instability of h2o2 monopropellant thrusters with reactor aspect ratio and pressures. *Journal of Propulsion and Power*, 27(2):422–427, 2011.

[3] Sungyong An and Sejin Kwon. Catalyst bed sizing of 50 newton hydrogen peroxide monopropellant thruster. In *44th AIAA/ASME/SAE/ASEE Joint Propulsion Conference & Exhibit*, page 5109, 2008.

[4] P. Mullens E. Wernimont M. Ventura, G. Garboden. Past and present uses of rocket grade hydrogen peroxide. 1991.

[5] Mike Jetzer. "Mercury Redstone Gas Genarator by Heroicrelics.org ". https://goo.gl/qbXMN5. Online; accessed 28 Jan 2019.

[6] William E Anderson, Kathy Butler, Dave Crocket, Tim Lewis, and Curtis McNeal. Peroxide propulsion at the turn of the century. https://ntrs.nasa.gov/archive/nasa/casi.ntrs.nasa.gov/20000033615.pdf, 2000. Online; accessed 22 June 2018.

[7] ArianeGroup. "New Technologies In Green Propellants:Alternative Green Propellants for Space Propulsion". https://goo.gl/8mrTTF. Online; accessed 28 Jan 2019, ArianeGroup GmbH.

[8] "Technology for propulsion and innovation". http://www.t4innovation.com/, 2019. Online; accessed 20 Jan 2019.

[9] M Ventura and E Wernimont. Advancements in high concentration hydrogen peroxide catalyst beds. In *37th Joint Propulsion Conference and Exhibit*, page 3250, 2001.

[10] A. Pasini, L. Torre, L. Romeo, A. Cervone, and L. d'Agostino. Reduced-order model for h2o2 catalytic reactor performance analysis. *Journal of propulsion and power*, 26(3):446–453, 2010.

[11] L Chiappetta, L Spadaccini, H Huang, W Watkins, and A Crocker. Modeling a hydrogen peroxide gas generator for rockets. In *36th AIAA/ASME/SAE/ASEE Joint Propulsion Conference and Exhibit*, page 3223, 2000.

[12] Jack F Runckel, Conrad M Willis, and Leland Blackwood Salters. *Investigation of Catalyst Beds for 98-Percent-Concentration Hydrogen Peroxide*. National Aeronautics and Space Administration, 1963.

[13] S Whitaker. Flow in porous media 1: A theoretical derivation of darcy's law. *Transport in porous media*, 1(1):3–25, 1986.

[14] Jeremy Corpening, Stephen Heister, Willam Anderson, and Benjamin Austin. A model for thermal decomposition of hydrogen peroxide. In *40th AIAA/ASME/SAE/ASEE Joint Propulsion Conference and Exhibit*, page 3373, 2004.

[15] Xu Zhou and Darren Hitt. Numerical modeling of monopropellant decomposition in a micro-catalyst bed. In *35th AIAA Fluid Dynamics Conference and Exhibit*, page 5033, 2005.

[16] Stanley M Walas. *Chemical Process Equipment Selection and Design*. (USA) Inc. All rights reserved, 1990.

[17] Sangwoo Jung, Sukmin Choi, and Sejin Kwon. Design optimization of green monopropellant thruster catalyst beds using catalytic decomposition modeling. In *53rd AIAA/SAE/ASEE Joint Propulsion Conference*, page 4924, 2017.

[18] R-J Koopmans, JS Shrimpton, GT Roberts, and AJ Musker. Dependence of pellet shape and size on pressure drop in h2o2 thrusters. *Journal of Propulsion and Power*, 30(3):775–789, 2014.

[19] VV Sorokin. Calculation of two-phase adiabatic flow in a pebble bed. *High Temperature*, 46(3):432–434, 2008.

[20] JA Tallmadge. Packed bed pressure drop—an extension to higher reynolds numbers. *AIChE Journal*, 16(6):1092–1093, 1970.

[21] Nikolay Mikhailovich Kuznetsov and Sergei Mikhailovich Frolov. The calculation of liquid-vapor phase equilibrium in h 2 oh 2 o 2 two-component system. *High Temperature*, 46(6):775–781, 2008.

[22] NIST. "nist chemistry webbook, nist standard reference database ". http://webbook.nist.gov/chemistry/, 2019. Online; accessed 26 Nov 2019.

[23] AK Coker. *Ludwig's applied process design for chemical and petrochemical plants, volume 1, Gulf Professional*. Oxford: UK, 2007.

[24] AL Tsykalo and AG Tabachnikov. Density, viscosity, and bond energy of molecules in aqueous hydrogen peroxide solutions. *Theoretical and Experimental Chemistry*, 2(6):602–605, 1966.

[25] Frank E Jones and Georgia L Harris. Its-90 density of water formulation for volumetric standards calibration. *Journal of research of the National Institute of Standards and Technology*, 97(3):335, 1992.

[26] Victor A Bloomfield and RK Dewan. Viscosity of liquid mixtures. *The Journal of Physical Chemistry*, 75(20):3113–3119, 1971.

[27] Philip J Pritchard and John W Mitchell. *Fox and McDonald's introduction to fluid mechanics*. John Wiley & Sons, 2016.

[28] Thomas A Davidson. Simple and accurate method for calculating viscosity of gaseous mixtures. 1993.

[29] MT Constantine and EF Cain. Hydrogen peroxide handbook. Technical report, Rocketdyne Canoga Park CA Chemical and Material Sciences Dept, 1967.

[30] Peter William Atkins and Julio De Paula. *Physical Chemistry: Peter Atkins, Julio de Paula*. WH Freeman and Company, 2010.

[31] Robert-Jan Koopmans. *Modelling of multiphase multicomponent chemically reacting flows through packed beds*. PhD thesis, University of Southampton, 2013.

[32] RW Lockhart, RC Martinelli, et al. Proposed correlation of data for isothermal two-phase, two-component flow in pipes. *Chem. Eng. Prog*, 45(1):39–48, 1949.

[33] Duncan Chisholm. A theoretical basis for the lockhart-martinelli correlation for two-phase flow. *International Journal of Heat and Mass Transfer*, 10(12):1767–1778, 1967.

[34] Sven Crone, Christian Bergins, and Karl Strauss. Multiphase flow in homogeneous porous media with phase change. part i: Numerical modeling. *Transport in porous media*, 49(3):291–312, 2002.

[35] Oliver Bey and Gerhart Eigenberger. Fluid flow through catalyst filled tubes. *Chemical Engineering Science*, 52(8):1365–1376, 1997.

[36] Ankit Rohatgi. Webplotdigitizer. https://automeris.io/WebPlotDigitizer, 2020.

[37] Kyle M Brunner, Joshua C Duncan, Luke D Harrison, Kyle E Pratt, Robson PS Peguin, Calvin H Bartholomew, and William C Hecker. A trickle fixed-bed recycle reactor model for the fischer-tropsch synthesis. *International Journal of Chemical Reactor Engineering*, 10(1), 2012.

[38] Seonuk Heo, Sungkwon Jo, Yongtae Yun, and Sejin Kwon. Effect of dual-catalytic bed using two different catalyst sizes for hydrogen peroxide thruster. *Aerospace Science and Technology*, 78:26–32, 2018.

[39] ifm electronic gmbh. ifm PT5412 Pressure transmitter. https://www.ifm.com/de/en/product/PT5412.
Accessed: 28-12-2020.

[40] RS Components. RS PRO thermocouple data sheet DTMC8. https://docs.rs-online.com/688e/0900766b8157cd8f.pdf.
Accessed: 28-12-2020.

[41] Mark Ventura and Dick Durant. Field handling of hydrogen peroxide. In *40th AIAA/ASME/SAE/ASEE Joint Propulsion Conference and Exhibit*, page 4146, 2004.

[42] BTC Zandbergen. *Thermal Rocket Propulsion (version 2.07)*. Delft University of Technology, 2018.

[43] GC Williams, CN Satterfield, and HS Isbin. Calculation of adiabatic decomposition temperatures of aqueous hydrogen peroxide solutions. *Journal of the American Rocket Society*, 22(2):70–77, 1952.

A

APPENDIX A: ADDITIONAL FLOW PROPERTIES

Coefficient	$H_2O_{(l)}$
A	34.25667
B	1523.290
C	-3196.413
D	2474.455
E	3.855326

Table A.1: Specific heat coefficients for liquid H_2O valid for temperature range from 298 K to 1500 K

Coefficient	$H_2O_{(g)}$
A	30.09200
B	6.832514
C	6.793435
D	-2.534480
E	0.082139

Table A.2: Specific heat coefficients for gaseous H_2O valid for temperature range from 500 K to 1700 K

Coefficient	O_2 (g)
A	31.32234
B	-20.23531
C	57.86644
D	-36.50624
E	-0.007374

Table A.3: Specific heat coefficients for gaseous O_2 valid for temperature range from 100 K to 700 K

Coefficient	O_2 (g)
A	20.91111
B	10.72071
C	-2.020498
D	0.146449
E	9.245722

Table A.4: Specific heat coefficients for gaseous O_2 valid for temperature range from 700 K to 2000 K

Coefficient	H_2O_2 (g)
A	34.25667
B	55.18445
C	-35.15443
D	9.087440
E	-0.422157

Table A.5: Specific heat coefficients for gaseous H_2O_2

Coefficient	H_2O_2 (l)
A	–15.248
B	0.67693
C	-1.4948×10^{-3}
D	1.2018×10^{-6}

Table A.6: Specific heat coefficients for liquid H_2O_2 valid for temperature range from 273 K to 694 K

The Specific heat coefficient used in the Shomate equation for gaseous and liquid species of the flow is given in tables A.1 to A.5 obtained from NIST[1]. The Specific heat coefficient for liquid H_2O_2 is given in table A.6 valid for temperature range 273 K to 694 K [2].

	Specific heat capacity, Cp [J mol^{-1} K^{-1}]		
Temperature, [K]	$O_2(g)$	$HO_2(g)$	$H_2O_2(g)$
579.52	31.73	35.90	54.47
596.00	31.90	36.08	54.94
612.40	32.07	36.27	55.39
628.73	32.23	36.46	55.83
644.99	32.38	36.65	56.25
661.18	32.53	36.84	56.65
677.30	32.67	37.03	57.04
693.36	32.80	37.23	57.41
709.36	32.93	37.42	57.77
725.30	33.06	37.62	58.12
741.18	33.19	37.81	58.45
757.00	33.31	38.01	58.78
772.76	33.44	38.20	59.09
788.47	33.55	38.40	59.39
804.12	33.66	38.59	59.69
819.73	33.77	38.79	59.97
835.27	33.87	38.98	60.25
850.77	33.97	39.18	60.51
866.22	34.07	39.37	60.77
881.62	34.16	39.57	61.02
896.97	34.25	39.76	61.27
912.28	34.34	39.96	61.51

Table A.8: Specific heat capacities of gases at high temperatures

Flow type Liquid	**Flow type Gas**	**Chisholm Constant**
Viscous	Viscous	5
Turbulent	Viscous	10
Viscous	Turbulent	12
Turbulent	Turbulent	20

Table A.7: Flow type and Chisholm constant

Table summarises the type of flows based on the Chisholm constant [3] & [4]

B

APPENDIX B:ADDITIONAL MODEL VERIFICATION DATA

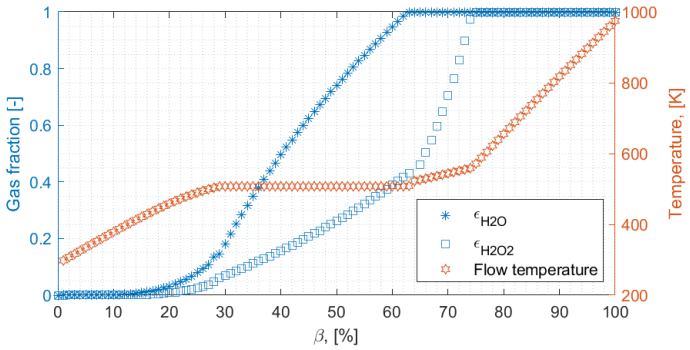

Figure B.1: Flow characteristics of decomposing 87.5 HTP at 30 bar Pressure (Case 1)

The Figure B.3 obtained from literature [5], shows model generated result of the reaction progression from 0-100 % over catalytic bed length given in [m]. This Figure B.3 was used in order to perform comparison of the model in chapter 3 by digitising to create Figure 3.4

The Figure B.4 obtained from literature [5], shows model generated result of the pressure distribution in [Pa] over catalytic bed length given in [m]. This Figure B.4 was used in order to perform comparison of the model in chapter 3 by digitising to create Figure 3.7

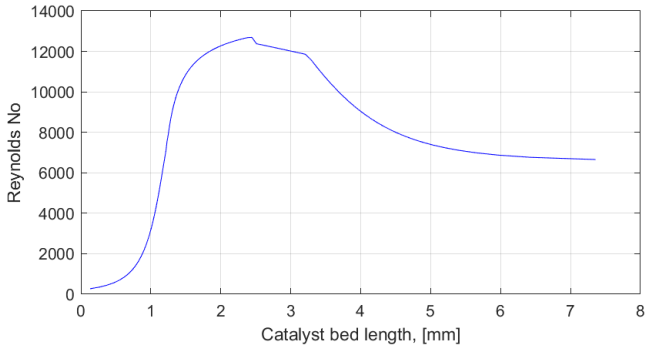

Figure B.2: Flow Reynolds number along the catalyst bed (Case 1)

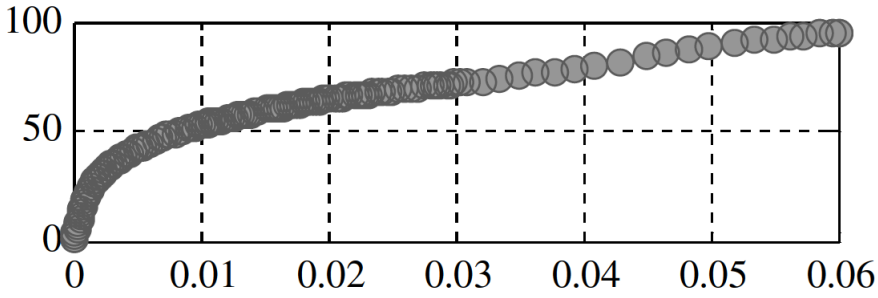

Figure B.3: Simulated reaction progression over the s catalyst bed length [5]

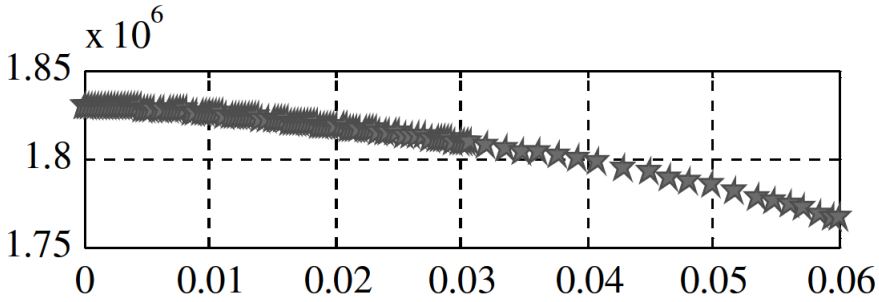

Figure B.4: Simulated pressure distribution over the catalyst bed [5]

The Figure B.5 obtained from literature [5], shows model generated result of the temperature distribution given in [K] % over catalytic bed length given in [m]. The Figure B.5 was used in order to perform comparison of the model in chapter 3 by digitising to create Figure 3.6

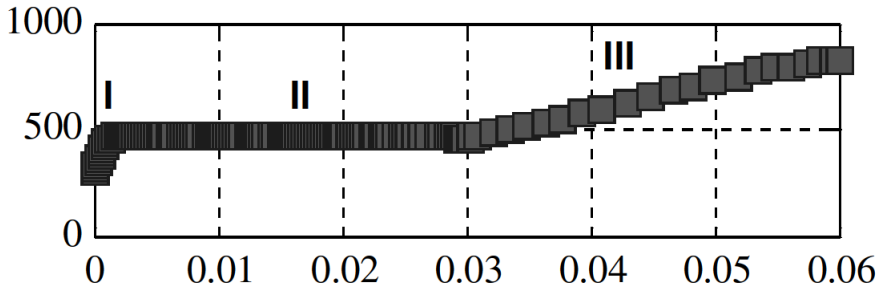

Figure B.5: Simulated flow temperature distribution over the catalyst bed [5]

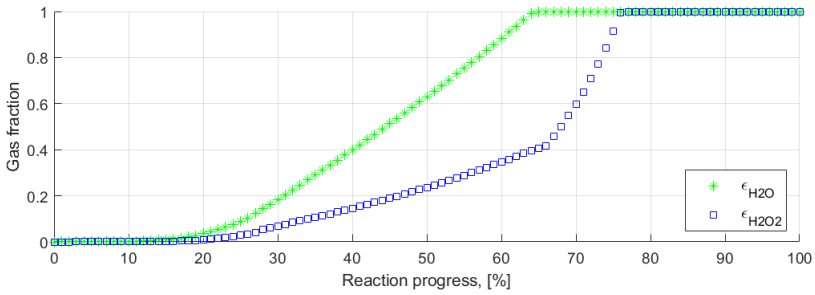

Figure B.6: Gas fraction profiles of simulation case 3

The Figure B.6 shows the gas fraction profiles of % H_2O_2 & H_2O at each point of reaction progression. The profiles are results of simulating case 3.

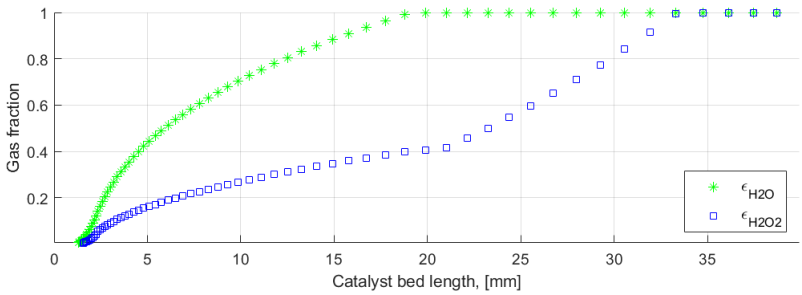

Figure B.7: Gas fraction profiles along the catalyst bed length of simulation case 3

The Figure B.7 shows the gas fraction profiles of % H_2O_2 & H_2O over catalytic bed length given in [m]. The profiles are results of simulating case 3 .

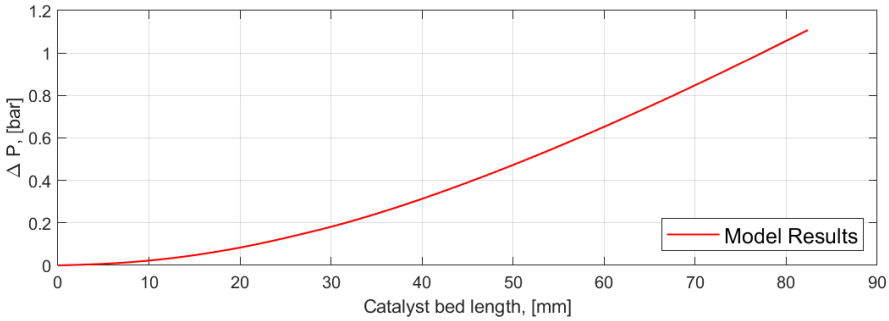

Figure B.8: Pressure losses over the catalyst bed length (case 3)

		Δ P [bar]	Deviation wrt R1, [%]	Deviation wrt R2, [%]
	Model Result (case 3)	0.647	+2.70%	−0.467%
R1	**Pasini et al Model Result [5]**	0.63	0	−3.08%
R2	**Experimental Result [5]**	0.65	3.17%	0

Table B.1: Comparison of pressure losses and respective deviations

The Table B.1 shows comparison of model simulated pressure difference to that of Pasini et al[5].

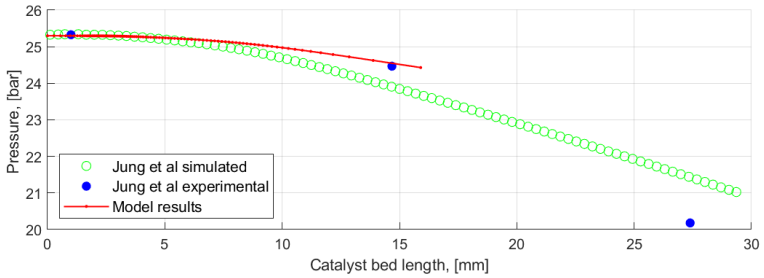

(a) Pressure distribution over the catalyst bed (case 4)

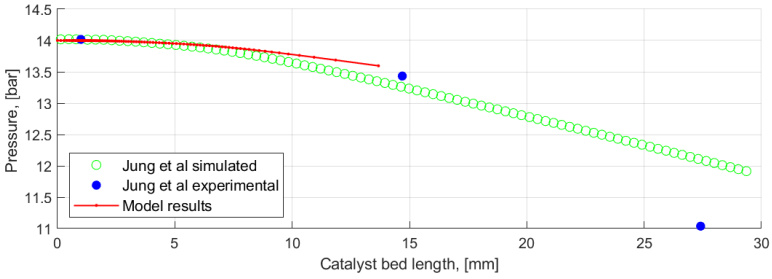

(b) Pressure distribution over the catalyst bed (case 5)

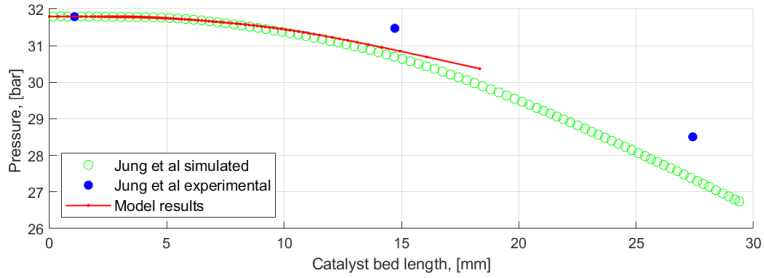

(c) Pressure distribution over the catalyst bed (case 6)

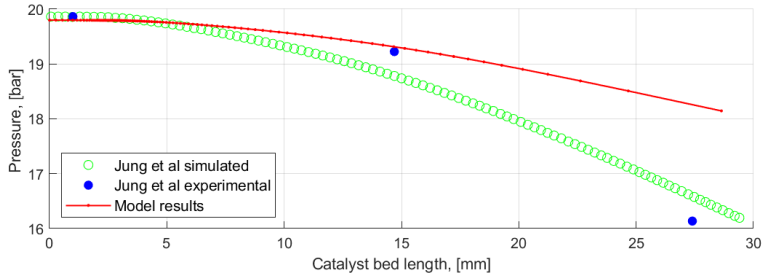

(d) Pressure distribution over the catalyst bed (case 7)

Figure B.9: Pressure distribution over the catalyst bed for case 4 to 7

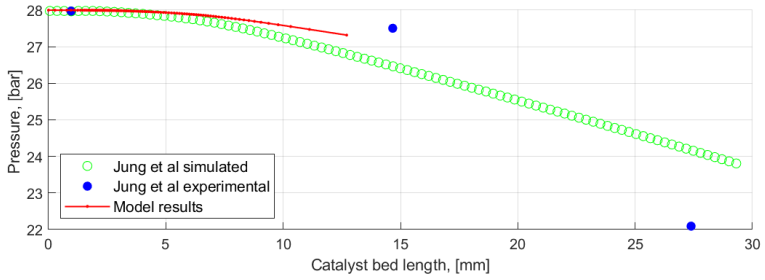

(a) Pressure distribution over the catalyst bed (case 8)

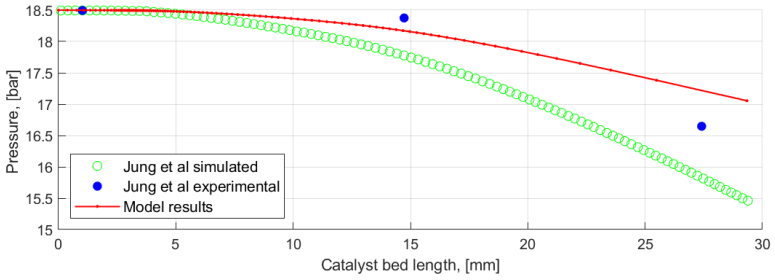

(b) Pressure distribution over the catalyst bed (case 9)

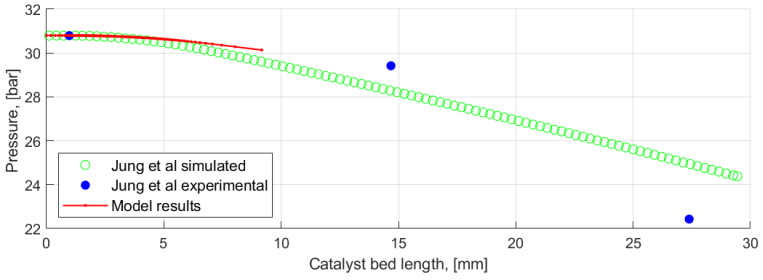

(c) Pressure distribution over the catalyst bed (case 10)

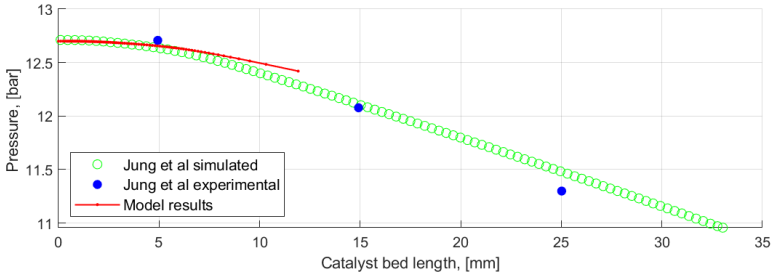

(d) Pressure distribution over the catalyst bed (case 11)

Figure B.10: Pressure distribution the catalyst bed for case 8 to 11

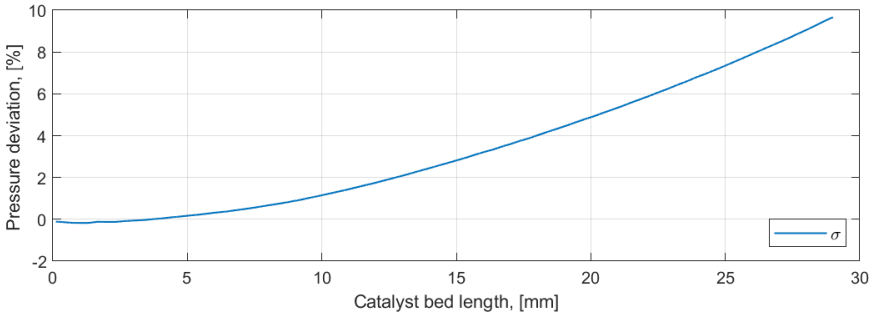

Figure B.11: Pressure deviation between model results and Jung et al simulated results (case 4 extended to catalyst bed length of 29 [mm])

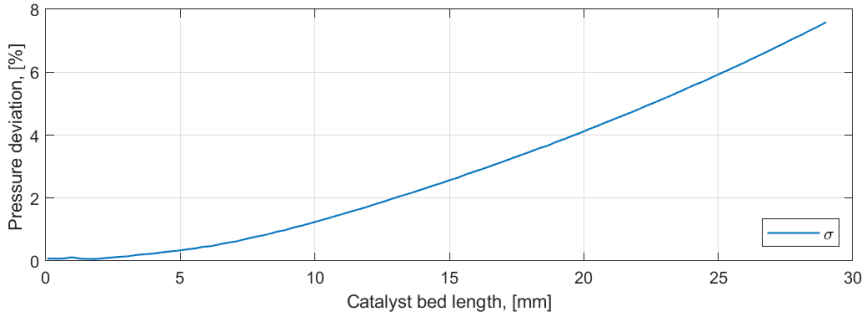

Figure B.12: Pressure deviation between model results and Jung et al simulated results (case 5 extended to catalyst bed length of 29 [mm])

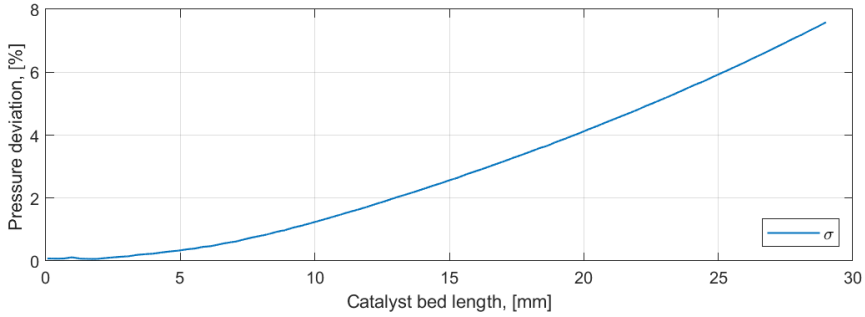

Figure B.13: Pressure deviation between model results and Jung et al simulated results (case 5 extended to catalyst bed length of 29 [mm])

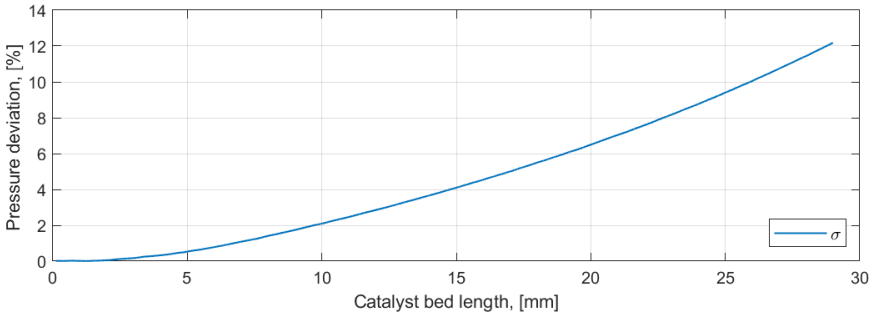

Figure B.14: Pressure deviation between model results and Jung et al simulated results (case 7 extended to catalyst bed length of 29 [mm])

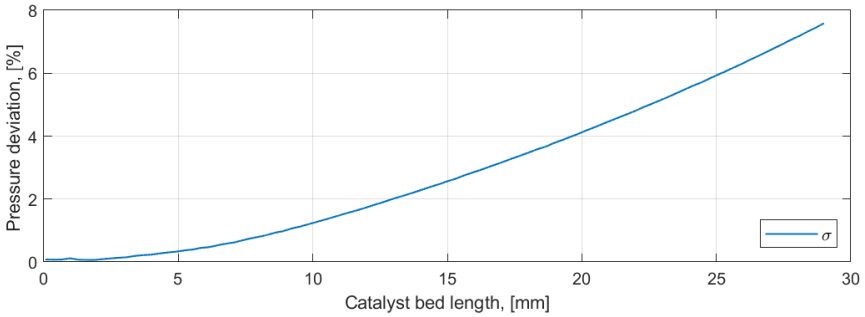

Figure B.15: Pressure deviation between model results and Jung et al simulated results (case 8 extended to catalyst bed length of 29 [mm])

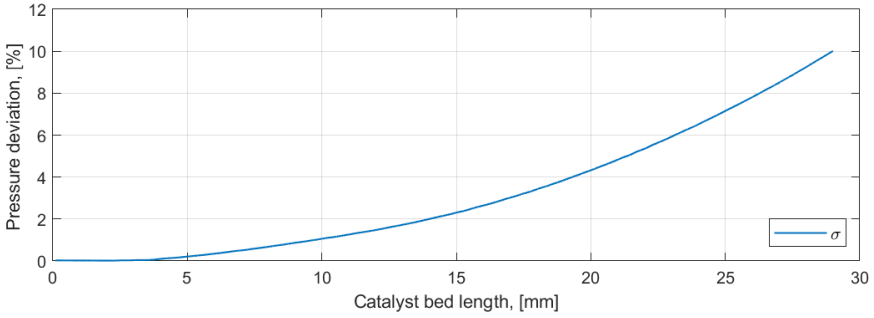

Figure B.16: Pressure deviation between model results and Jung et al simulated results (case 9)

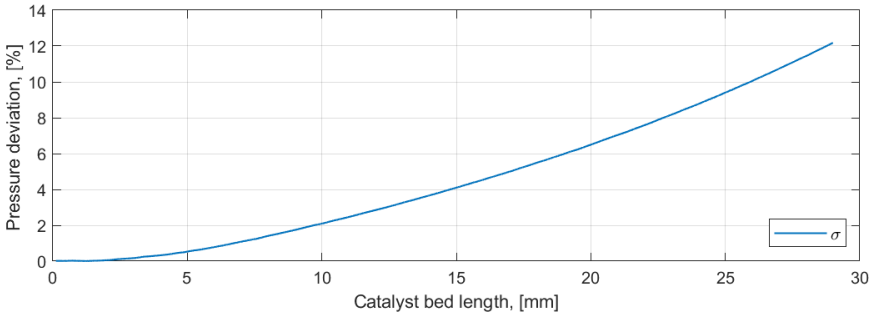

Figure B.17: Pressure deviation between model results and Jung et al simulated results (case 10 extended)

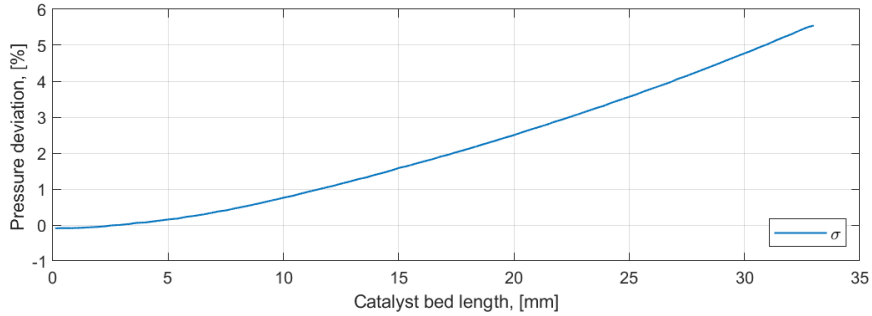

Figure B.18: Pressure deviation between model results and Jung et al simulated results (case 11)

Catalyst bed Location [mm]	**Model** [bar]	**Jung et al simulated** [bar]	**Jung et al experimental** [bar]
1.13	25.3	25.34	25.33
14.68	24.55	23.91	24.47
27.4	23.29	21.44	20.18
29	23.13 (Extened)	21.09	-

Table B.2: Key pressure values (case 4)

Catalyst bed location [mm]	**Model** [bar]	**Jung et al simulated** [bar]	**Jung et al experimental** [bar]
0.99	14	14.02	14.02
14.68	13.53	13.26	13.43
27.4	12.9 (Extended)	12.10	11.0
29	12.81 (Extended)	11.95	-

Table B.3: Key pressure values (case 5)

Catalyst bed Location [mm]	**Model** [bar]	**Jung et al simulated** [bar]	**Jung et al experimental** [bar]
1.16	31.8	31.8	31.8
14.72	13.3	30.7	31.48
27.4	29.69	27.36	28.51
29	-	21	-

Table B.4: Key pressure values (case 6 tuned)

Catalyst bed location [mm]	**Model** [bar]	**Jung et al simulated** [bar]	**Jung et al experimental** [bar]
1.16	19.86	19.86	19.86
14.72	19.37	18.78	19.23
27.4	18.38	16.58	16.14
29	-	16.2	-

Table B.5: Key pressure values (case 7))

Catalayst bed Location [mm]	**Model** [bar]	**Jung et al simulated** [bar]	**Jung et al experimental** [bar]
0.95	28	28	28
14.67	27.14 (extended)	26.46	27.5
27.38	25.8 (extended)	24.15	22.09
29	25.68 (extended)	23.86	-

Table B.6: Key pressure values (case 8)

Catalyst bed location [mm]	**Model** [bar]	**Jung et al simulated** [bar]	**Jung et al experimental** [bar]
1.01	18.5	18.5	18.5
14.73	18.16	17.78	18.37
27.41	17.22	15.83	16.65
29	17.08	15.53	-

Table B.7: Key pressure values (case 9)

Catalyst bed location [mm]	**Model** [bar]	**Jung et al simulated** [bar]	**Jung et al experimental** [bar]
0.97	30.8	30.8	30.8
14.68	29.40	28.29	29.42
27.39	27.7	24.95	22.3
29	27.48	24.52	-

Table B.8: Key pressure values (case10)

Catalyst bed location [mm]	**Model** [bar]	**Jung et al simulated** [bar]	**Jung et al experimental** [bar]
4.93	12.66	12.64	12.71
14.92	12.12	12.29	12.08
25.02	11.88	11.48	11.3
33	11.57	10.96	-

Table B.9: Key pressure values (case11)

C

APPENDIX C:

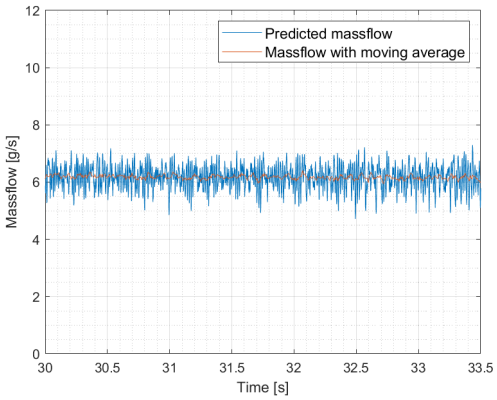

Figure C.1: Predicted massflow of test E16

The figure C.1 shows the predicted massflow, using relation 5.1 and a moving average with a window of 100 samples on the predicted flow rate.

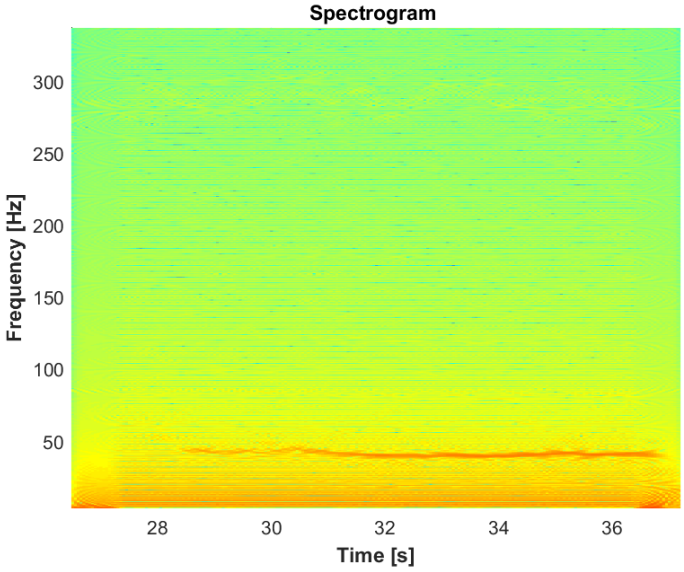

Figure C.2: Spectogram (Test E14)

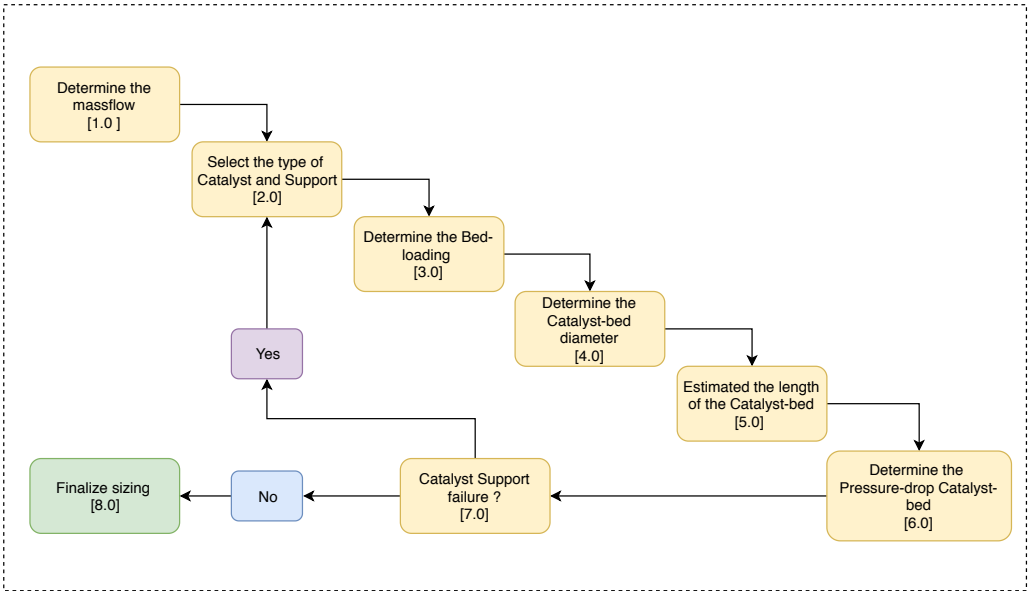

Figure C.3: Design process showing the steps need to be taken to size a catalyst-bed

Ref	HTP	ID	$\dot{m}$	L	D	L/D	Area	Volume	G	D_p
	$[w/w]$	-	$[g/s]$	$[mm]$	$[mm]$	$[-]$	$[mm^2]$	$[mm^3]$	$[kg/sm^2]$	$[mm]$
[6]	90%	K 50N	34.8	30	40	0.75	1256	37699	27.69	-
[7]	90%	K 50N T 1 p1	25.6	16	31.2	0.51	764	12232	33.48	1.18-2
[7]	90%	K 50N T 1 p1	37.8	16	31.2	0.51	764	12232	49.44	1.18-2
[7]	90%	K 50N T 1 p1	53.8	16	31.2	0.51	764	12232	70.37	1.18-2
[7]	90%	K 50N T 1 p2	21.7	16	31.2	0.51	764	12232	28.38	1.18-2
[7]	90%	K 50N T 1 p2	35.3	16	31.2	0.51	764	12232	46.17	0,85-1.18
[7]	90%	K 50N T 1 p2	55.2	16	31.2	0.51	764	12232	72.20	0,85-1.18
[7]	90%	K 50N T 2 p1	17.7	25	25	1	490.87	12271	36.06	1.18-2
[7]	90%	K 50N T 2 p1	30.6	25	25	1	490.87	12271	62.34	1.18-2
[7]	90%	K 50N T 2 p1	44.2	25	25	1	490.87	12271	90.04	1.18-2
[7]	90%	K 50N T 2 p1	54.5	25	25	1	490.87	12271	111.02	1.18-2
[7]	90%	K 50N T 2 p2	17.5	25	25	1	490.87	12271	35.65	0,85-1.18
[7]	90%	K 50N T 2 p2	30.3	25	25	1	490.87	12271	61.73	0,85-1.18
[7]	90%	K 50N T 2 p2	44.2	25	25	1	490.87	12271	90.04	0,85-1.18
[7]	90%	K 50N T 2 p2	54.8	25	25	1	490.87	12271	111.64	0,85-1.18
[7]	90%	K 50N T 3 p1	14.7	39	20	1.95	314.16	12252	46.79	1.18-2
[7]	90%	K 50N T 3 p1	24.8	39	20	1.95	314.16	12252	78.94	1.18-2
[7]	90%	K 50N T 3 p1	35.3	39	20	1.95	314.16	12252	112.36	1.18-2
[7]	90%	K 50N T 3 p1	48.3	39	20	1.95	314.16	12252	153.74	1.18-2
[7]	90%	K 50N T 3 p2	13.3	39	20	1.95	314.16	12252	42.34	0.85-1.18
[7]	90%	K 50N T 3 p2	21.5	39	20	1.95	314.16	12252	68.44	0.85-1.18
[7]	90%	K 50N T 3 p2	30.9	39	20	1.95	314.16	12252	98.36	0.85-1.18
[7]	90%	K 50N T 3 p2	38.2	39	20	1.95	314.16	12252	121.59	0,85-1.18
[8]	90%	K T 1	18.3	16.5	33	0.5	855.30	14112	21.34	0.85–1.13
[8]	90%	K T 1	32	16.5	33	0.5	855.30	14112	37.41	0.85–1.13
[8]	90%	K T 1	50.9	16.5	33	0.5	855.30	14112	59.51	0.85–1.13
[8]	90%	K T 1	67.1	16.5	33	0.5	855.30	14112	78.45	0.85–1.13
[8]	90%	K T 2	15.6	26.5	26	1.019	530.93	14069	29.38	0.85–1.13

Ref	HTP	ID	$\dot{m}$	L	D	L/D	Area	Volume	G	D_p
[8]	90%	K T 2	30.1	26.5	26	1.019	530.93	14069	56.69	0.85–1.13
[8]	90%	K T 2	44.6	26.5	26	1.019	530.93	14069	84.0	0.85–1.13
[8]	90%	K T 2	62.9	26.5	26	1.019	530.93	14069	118.47	0.85–1.13
[8]	90%	K T 3	9.4	41	21	1.95	346.36	14200	27.14	0.85–1.13
[8]	90%	K T 3	17.9	41	21	1.95	346.36	14200	51.68	0.85–1.13
[8]	90%	K T 3	27	41	21	1.95	346.36	14200	77.95	0.85–1.13
[8]	90%	K T 3	38.8	41	21	1.95	346.36	14200	112.02	0.85–1.13
[9]	90%	K T (small)	1.82	30	10	3	78.54	2356	23.17	0.85–1.13
[9]	90%	K T (small)	2.36	30	10	3	78.54	2356	30.04	0.85–1.13
[9]	90%	K T (small)	2.72	30	10	3	78.54	2356	34.63	0.85–1.13
[9]	90%	K T (small)	2.95	30	10	3	78.54	2356	37.56	0.85–1.13
[9]	90%	K T (large)	30.9	30	30	1	706.86	21205	43.71	3,1
[9]	90%	K T (large)	37.9	30	30	1	706.86	21205	53.61	3,1
[9]	90%	KAIT T (large)	45.9	30	30	1	706.86	21205	64.93	3,1
[10]	90%	K Hydbrid pe	120	21	60	0.35	2827.43	59376	42.44	2.00 - 1.19
[11]	90%	K HYB 2.5kN	1060	105	113	0.93	10028.75	1053018	105.70	2.00 - 1.19 MnO2
[12]	90%	K HYB 1	108.4	33	45.8	0.720	1647.48	54366	65.80	-
[12]	90%	K HYB 2	108.8	33	45.8	0.720	1647.48	54366	66.04	-
[12]	90%	K HYB 3	107.1	33	45.8	0.720	1647.48	54366	65.01	-
[12]	90%	K HYB 4	106	33	45.8	0.720	1647.48	54366	64.34	-
[13]	90%	ratio 0	147.87	34.5	60	0.575	2827.43	97546	52.3	3,1 Mno2-Pbo
[13]	90%	ratio 0	253.90	34.5	60	0.575	2827.43	97546	89.8	3,1 Mno2-Pbo
[13]	90%	ratio 0	328.27	34.5	60	0.575	2827.43	97546	116.1	3,1 Mno2-Pbo
[13]	90%	2 pellets 0	410.26	34.5	60	0.575	2827.43	97546	145.1	3,1 Mno2-Pbo
[13]	90%	2 pellets 0,183	147.87	34.5	60	0.575	2827.43	97546	52.3	3,1 & 1.18-2
[13]	90%	2 pellets 0,183	254.47	34.5	60	0.575	2827.43	97546	90	3,1 & 1.18-2
[13]	90%	2 pellets 0,183	329.11	34.5	60	0.575	2827.43	97546	116.4	3,1 & 1.18-2
[13]	90%	2 pellets 0,183	409.70	34.5	60	0.575	2827.43	97546	144.9	3,1 & 1.18-2
[13]	90%	2 pellets 0,342	147.87	34.5	60	0.575	2827.43	97546	52.3	3,1 & 1.18-2

Ref	HTP	ID	$\dot{m}$	L	D	L/D	Area	Volume	G	D_p
[13]	90%	2 pellets 0,342	254.19	34.5	60	0.575	2827.43	97546	89.9	3,1 & 1.18-2
[13]	90%	2 pellets 0,342	328.55	34.5	60	0.575	2827.43	97546	116.2	3,1 & 1.18-2
[13]	90%	2 pellets 0,342	409.98	34.5	60	0.575	2827.43	97546	145	3,1 & 1.18-2
[13]	90%	2 pellets 0,545	147.59	34.5	60	0.575	2827.43	97546	52.2	3,1 & 1.18-2
[13]	90%	2 pellets 0,545	254.75	34.5	60	0.575	2827.43	97546	90.1	3,1 & 1.18-2
[13]	90%	2 pellets 0,545	329.40	34.5	60	0.575	2827.43	97546	116.5	3,1 & 1.18-2
[13]	90%	2 pellets 1	146.74	34.5	60	0.575	2827.43	97546	51.9	3,1 & 1.18-2
[13]	90%	2 pellets 1	255.03	34.5	60	0.575	2827.43	97546	90.2	3,1 & 1.18-2
[13]	90%	2 pellets 1	330.81	34.5	60	0.575	2827.43	97546	117	3,1 & 1.18-2
[14]	90%	K 50 N case 1	32.08	39	20	1.95	314.16	12252	102.11	10-16 mesh MnO2
[14]	90%	K 50 N case 2	32.08	39	20	1.95	314.16	12252	102.11	10-16 mesh mno2 pbo
[14]	90%	K 50 N case 3	32.08	39	20	1.95	314.16	12252	102.11	10-16 mesh mno2
[14]	90%	K 50 N case 4	32.08	39	20	1.95	314.16	12252	102.115	10-16 mesh mno2 pbo
[15]	90%	K Retro prop	310	50	85	0.588	5674.50	283725	54.63	3,1 MnO2 & Al203
[15]	90%	K Retro prop	310	50	85	0.588	5674.50	283725	54.63	3,1 MnO2 & Al203
[15]	90%	K Retro prop	310	50	85	0.588	5674.50	283725	54.63	3,1 MnO2 & Al203
[15]	90%	K Retro prop	310	50	85	0.588	5674.50	283725	54.63	3,1 MnO2 & Al203
[15]	90%	K Retro prop	310	50	85	0.588	5674.50	283725	54.63	3,1 MnO2 & Al203
[15]	90%	K Retro prop	310	50	85	0.588	5674.50	283725	54.63	3,1 MnO2 & Al203
[15]	90%	K Retro prop	310	50	85	0.588	5674.50	283725	54.63	3,1 MnO2 & Al203
[16]	90%	IOT	133.2	53.1	58.9	0.902	2724.71	144682	48.89	-
[17]	90%	K 2.5 kn bi prop	751.11	37	80	0.4625	5026.55	185982	149.43	daul reactor
[17]	90%	K 2.5 kn bi prop	720.49	37	80	0.4625	5026.55	185982	143.33	-
[17]	90%	K 2.5 kn bi prop	713.13	37	80	0.4625	5026.55	185982	141.871	-
[17]	90%	K 2.5 kn bi prop	721.48	37	80	0.4625	5026.55	185982	143.54	-
[17]	90%	K 2.5 kn bi prop	743.80	37	80	0.4625	5026.56	185982	147.97	-
[18]	90%	K 800 N bi-prop	241.6	35	60	0.583	2827.43	98960	85.45	MnO2
[18]	90%	K 800 N bi prop	243.4	35	60	0.583	2827.43	98960	86.085	- MnO2
[19]	90%	K 50 N	39.1	40	27	1.481	572.56	22902	68.29	-

Ref	HTP	ID	$\dot{m}$	L	D	L/D	Area	Volume	G	D_p
[19]	90%	K 50 N	39.1	40	27	1.481	572.56	22902	68.29	-
[20]	90%	L1I1	45	40	30	1.33	706.86	28274	63.66	3,1
[20]	90%	L1I2	45	40	30	1.33	706.86	28274	63.66	3,1 & 0.85–1.13
[20]	90%	L2I1	45	20	30	0.67	706.86	14137	63.66	0.85–1.13
[21]	90%	LR-III-97	5.8	60	25	2.4	490.87	29452	11.82	0,6 Platinum
[21]	90%	LR-III-106	5.9	60	25	2.4	490.87	29452	12.02	0,6 Platinum
[21]	90%	LR-IV-11	5.8	60	25	2.4	490.87	29452	11.82	0,6 Platinum
[21]	90%	CZ-11-600	5.8	60	25	2.4	490.87	29452	11.82	0,6 Pt/Al2O3
[21]	70%	LR 59	3.85	32	8	4	50.27	1608	76.59	0,6 Al2O3
[21]	87.50%	LR 57	3.68	32	8	4	50.27	1608	73.21	0,6 Al2O3
[21]	87.50%	LR 59	3.68	32	8	4	50.27	1608	73.21	0,6 Al2O3
[21]	87.50%	silver	3.62	32	8	4	50.266	1608	72.02	- Silver mesh
[22]	85%	silver	-	-	-	-	-	-	250	- Silver mesh
[23]	85%	silver	1961.46	50.8	88.9	0.571	6207.17	315324	316	- Silver mesh
[23]	85%	silver	1091.02	25.4	88.9	0.286	6207.17	157662	175.76	- Silver mesh
[24]	91%	silver	48126.06		330.2	-	85633.56	-	562	- Silver mesh
[25]	90%	A-silver	90.84	35.052	25.4	1.38	506.71	17761.11	179	- Silver mesh
[25]	90%	B -silver	115.68	31	38.01	0.815	1134.71	35162.45	101	- Silver mesh
[25]	90%	C -silver	78.06	38.1	25	1.503	504.68	19228.41	154	- Silver mesh
[26]	90%	Silver	0.118	63.5	25.4	2.5	506.71	32175.92	232	- Silver mesh

Table C.1: Data from experimental catalyst beds and their operational condition

D

APPENDIX D: ADDITIONAL MODEL VALIDATION DATA

CASE 14V

Case 14V the data is sampled between 29.5 and 32 seconds of the test. This sampling width for experimental data is chosen considering any transient of pressure and temperature data. In the sampling window chosen the tank pressure is relatively constant. From the pressure data it can be seen that tank pressure has a transient from and a relative stable at 56.3 at bar. Considering the roughness of the pressure data, the sample mean is computed for 3 pressure sensor data and used in validation process. Similarly the average massflow is determined for the sampling region to be an average of 4.61 [gs^{-1}]. Case 14V is simulated with the conditions listed in table D.1.

Parameter	Value	Units
Pressure	54.06	[bar]
Mass flow	4.61	[gs^{-1}]
Inlet temperature	296.15	[K]
HTP concentration	88 %	[w/w]

Table D.1: Case 14V model input conditions

The temperature profile of the flow is shown in Figure D.1, with the simulated model results and experimental result. The saturation conditions of water is met at a L/D of 0.68 with a temperature of 541.2 kelvin. The dry out locations results for H_2O is at L/D of 1.07 and H_2O is at 1.27. The experimental data captures the flow temperature in the pre-boiling region and the gas phase. At a L/D of 0.455 the measure temperature range 302 [K] - 310 [K] the simulation predicts a temperature of 382 [K]. The gas phase flow

temperature at L/D 1.818 is measure in the range of 859[K] to 885[K] this corresponds to a reaction progression of 92% to 93.7% of the model. This temperature range is reached between L/D of 1.66 and 1.73 in the simulated results. According to the simulated results 98% of the reaction progression is reached at L/D 2.02 with a temperature of 952 [K]. The third thermocouple located at L/D 3.091 measured temperature range of 892 [K] to 903 [K]. The adiabatic decomposition temperature calculated by the model results with a temperature of 984.2[K], this is realised at a L/D of 2.418.

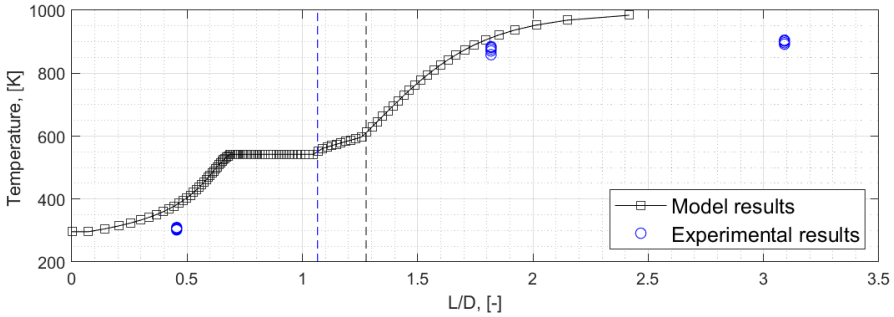

Figure D.1: Flow temperature over the catalyst bed with measured experimental results (Case 14V)

The Pressure data in Figure D.3 shows the pressure losses experienced by the flow. The experimental data shown in the plot is the average value of the pressure measured. Figure D.2 displays the actual pressure measured.

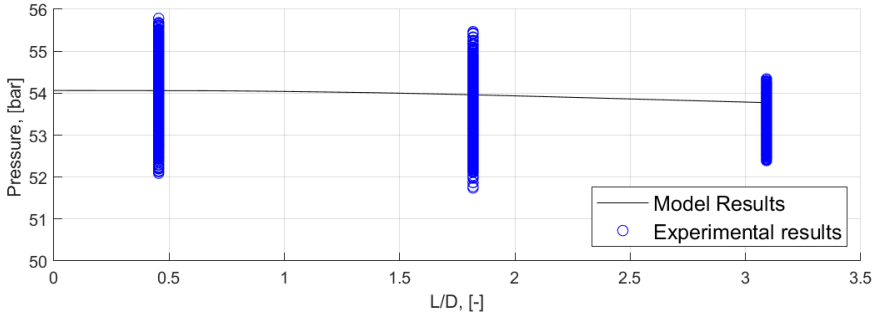

Figure D.2: Pressure distribution over the catalyst bed with measured experimental results (Case 14V)

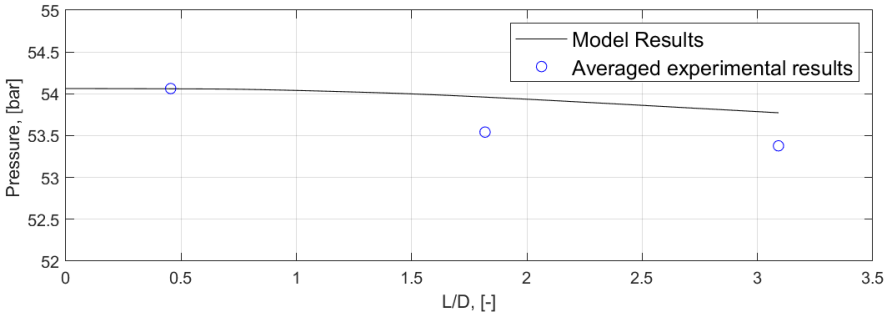

Figure D.3: Pressure distribution over the catalyst bed with averaged experimental results (Case 14V)

	L/D	Simulated	Measured range	Measured sample Mean
Flow temperature	0.459	325[K]	302 - 310 [K]	306 [K]
Flow temperature	2.018	912 [K]	859 - 884 [K]	874 [K]
Flow temperature	3.119	-	892 - 905 [K]	900 [K]
Pressure	0.459	54.06 [bar]	52.0910 - 55.7820 [bar]	54.06 [bar]
Pressure	2.018	53.96 [bar]	51.7410 - 55.4660 [bar]	54.54 [bar]
Pressure	3.119	53.77 [bar]	52.3930 - 54.3410[bar]	53.38 [bar]

Table D.2: Measured and simulated parameters of Case 14V

The pressure overall loss of the simulation results in 0.290 [bar] and the pressure loss calculated using the average of experimental data results a loss of 0.685 [bar]. The overall pressure loss percentage from the simulation is calculated as 0.543% and the experimental pressure loss percentage is calculated to be 1.283%. With the results it can be seen that simulated pressure losses are smaller than actually measured, however the results shown figure D.2 shown good agreement as the prediction by the model is within the given measured ranges of pressure at each location. The pressure roughness of the data depicted in Figure D.2 shows that the pressures in the sampling region of the data used. The simulated pressure data shows to be within the bounds of the pressure roughness of the measure data. The pressure roughness of the threes sensors are calculated as 6.83%, 6.96% & 3.65% in the increasing order of L/D. The absolute pressure drop of the flow in the simulated (0.290 [bar]) and the average of the measures pressure (0.685 [bar]). Considering the range of pressure roughness, the pressure losses are significantly small. The simulated pressure of the flow are within the bounds of the measured pressure sensors roughness as shown in D.2.

Case 15

Case 15 the data is sampled between 23 and 26.5 seconds of the test. This sampling width for experimental data is chosen considering as any transient of pressure and temperature data in and sampling window is chosen in region when tank pressure is relatively

constant. From the pressure data it can be seen that tank pressure has a transient from and a relative stable plateau between 23 and 26.5 seconds, in this region the pressure remains relative constant at 82.3bar. Considering the roughness of the pressure data, the sample mean is computed for 3 pressure sensor data and used in validation process. Similarly the average massflow is determined for the sampling region, the massflow is derived by the pressure drop over the injector to be an average of 6.10 [gs^{-1}]. Case 15 is simulated with the conditions listed in table D.3.

Parameter	Value	Units
Pressure	77.9	[bar]
Mass flow	6.12	[gs^{-1}]
Inlet temperature	296.15	[K]
HTP concentration	88 %	[w/w]

Table D.3: Case 15 model input conditions

The temperature profile of the flow is shown in Figure D.4, with the simulated model results and experimental results. As expected it can be seen in comparison to case 14, the saturation conditions occur at higher temperature as the operating pressure are higher. The saturation conditions of water is met at a L/D of 0.92 with a temperature of 565.9 kelvin. The dry out locations results in higher L/D compared to the case 14, dry out locations for H_2O is at L/D of 1.29 and H_2O is at 1.47. The experimental data captures the flow temperature in the pre-boiling region and the gas phase, the data shows good alignment with the model results. At a L/D of 0.455 the measure temperature range 314 [K] - 337 [K] the simulation predicts a temperature of 344 [K]. The gas phase flow temperature at L/D 1.818 is measure in the range of 834[K] to 851[K] this corresponds to a reaction progression of 90.5% to 91.5% of the model. This temperature range is reached between L/D of 1.767 and 1.80 in the simulated results. According to the simulated results 98% of the reaction progression is reached at L/D 2.140 with a temperature of 952 [K]. The third thermocouple located at L/D 3.091 measured temperature range of 899 [K] to 923 [K]. The adiabatic decomposition temperature calculated by the model results with a temperature of 984.2[K], this is realised at a L/D of 2.513.

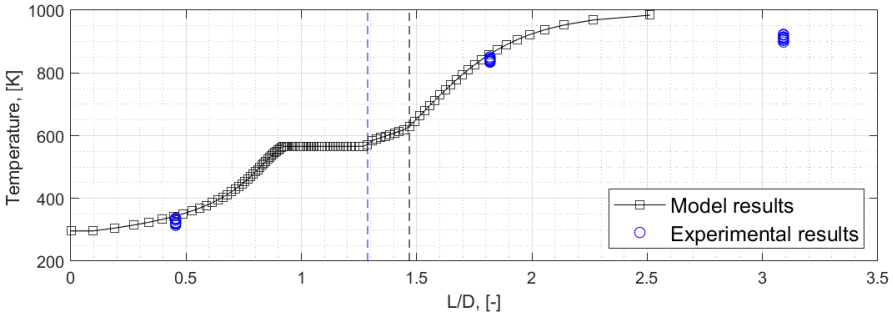

Figure D.4: Flow temperature over the catalyst bed with measured results (case 15)

The Pressure data in Figure D.6 shows the pressure losses experienced by the flow. The experimental data shown in the plot is the average value of the pressure measured. Figure D.5 displays the actual pressure measured.

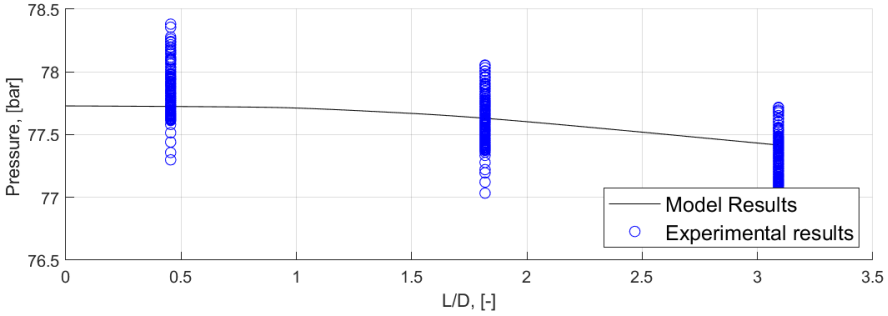

Figure D.5: Pressure distribution over the catalyst bed with measured results (case 15)

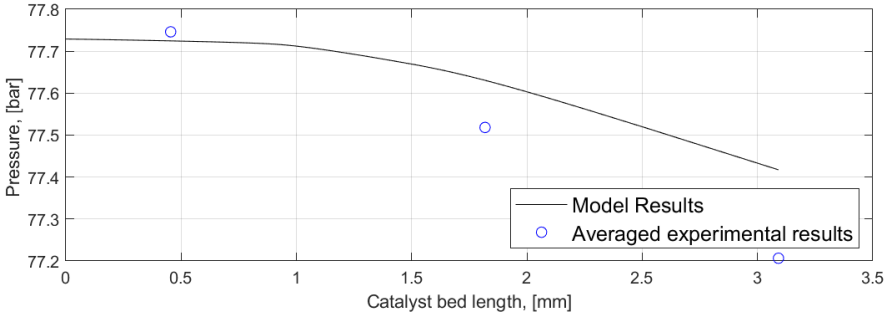

Figure D.6: Pressure distribution over the catalyst bed with averaged experimental results (case 15)

	L/D	Simulated	Measured range	Measured sample Mean
Flow temperature	0.459	344 [K]	314 - 337 [K]	326 [K]
Flow temperature	1.818	860 [K]	834 - 851 [K]	842[K]
Flow temperature	3.091	-	899 - 923 [K]	912 [K]
Pressure	0.459	77.72	75.9160 - 79.7780 [bar]	77.73[bar]
Pressure	1.818	77.63	75.9420 - 79.3130 [bar]	77.50 [bar]
Pressure	3.091	77.42	76.0470 - 78.480 [bar]	77.19 [bar]

Table D.4: Measured and simulated parameters of Case 15V

The pressure overall loss of the simulation results in 0.312 [bar] and the pressure loss calculated using the average of experimental data results a loss of 0.539 [bar]. The overall pressure loss percentage is calculated as 0.404% and the experimental pressure loss percentage is calculated to be 0.677%. With the results it can be seen that simulated pressure losses are smaller than actually measured, however the results shown figure D.5 shown good agreement as the prediction by the model is within the given measured ranges of pressure at each location. The pressure roughness of the data depicted in Figure D.5 shows that the pressures in the sampling region of the data used. The simulated pressure data shows to be within the bounds of the pressure roughness of the measure data. The pressure roughness of the threes sensors are calculated as 4.97%, 4.35% & 3.15% in the increasing order of L/D. The absolute pressure drop of the flow in the simulated (0.312 [bar]) and the average of the measures pressure (0.539 [bar]). Considering the range of pressure roughness, the pressure losses are significantly small. Hence the simulated pressure of the flow are within the bounds of the measured pressure sensors.

CASE 16

Case 16 the data is sampled between 29 and 33.5 seconds of the test. This sampling width for experimental data is chosen considering as any transient of pressure and temperature data in and sampling window is chosen in region when tank pressure is relatively constant. From the pressure data it can be seen that tank pressure has a transient from and a relative stable plateau between in the chosen time sampling range, in this region the pressure remains relative constant at 82 bar. Similar to the other cases the sample mean is computed for 3 pressure sensor data and used in validation process. Similarly the average massflow is determined for the sampling region, the massflow is derived by the pressure drop over the injector to be an average of 6.10 [gs^{-1}]. Case 16 is simulated with the conditions listed in table D.5.

Parameter	Value	Units
Pressure	77.9	[bar]
Mass flow	6.10	[gs^{-1}]
Inlet temperature	296.15	[K]
HTP concentration	88 %	[w/w]

Table D.5: Case 16 model input conditions

The temperature profile of the flow is shown in Figure D.7, with the simulated model results and experimental results. The saturation conditions of water is met at a L/D of 0.92 with a temperature of 566.3 kelvin. The dry out locations for H_2O is at L/D of 1.282 and H_2O is at 1.46. The experimental data captures the flow temperature in the pre-boiling region and the gas phase, the data shows good alignment with the model results. At a L/D of 0.455 the measure temperature range 341 [K] - 356 [K] the simulation predicts a temperature of 345 [K]. The gas phase flow temperature at L/D 1.818 is measure in the range of 883[K] to 915[K] this corresponds to a reaction progression of 93.6% to 95.6% of the model. This temperature range is reached between L/D of 1.88 and 1.98 in the simulated results. 98% of the reaction progression is reached at L/D 2.155 with a temperature of 953 [K]. The third thermocouple located at L/D 3.091 measured temperature range of 948 [K] to 954 [K], this is 3.68% to 3.07% lower than the adiabatic temperature. The adiabatic decomposition temperature calculated by the model results with a temperature of 984.2[K] at a L/D of 2.513.

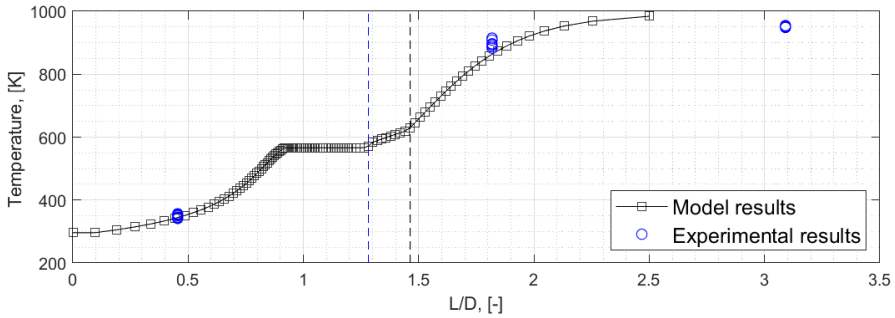

Figure D.7: Simulated flow temperature over the catalyst bed and experimental results (case 16)

The Pressure data in Figure D.8 shows the pressure losses experienced by the flow, the measured experimental data is depicted at each sensor locations. The experimental data shown in the plot is the average value of the pressure measured. Figure D.9 displays the actual pressure measured.

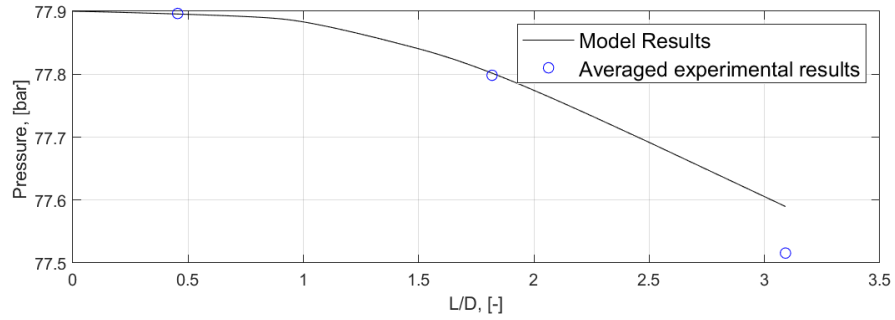

Figure D.8: Pressure distribution over the catalyst bed and averaged experimental results (case 16)

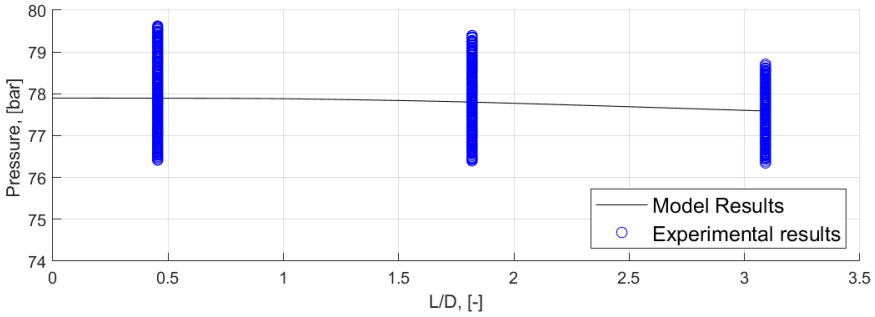

Figure D.9: Pressure distribution over the catalyst bed and experimental results (case 16)

	L/D	Simulated	Measured range	Measured sample Mean
Flow temperature	0.459	345 [K]	341 - 356 [K]	340 [K]
Flow temperature	1.818	853 [K]	883 - 915 [K]	899 [K]
Flow temperature	3.091	-	948 - 955 [K]	951[K]
Pressure	0.459	77.89	76.4140 - 79.6200 [bar]	77.89[bar]
Pressure	1.818	77.80	76.3970 - 79.3940[bar]	77.80 [bar]
Pressure	3.091	77.59	76.3480 - 78.7060 [bar]	77.52[bar]

Table D.6: Measured and simulated parameters of Case 16V

The pressure loss over the catalyst bed of the simulation results in 0.310 [bar] and the pressure loss calculated using the average of experimental data results a loss of 0.38 [bar]. The overall pressure loss percentage of simulation is calculated to be 0.40% and the experimental pressure loss percentage is calculated to be 0.49%. With the results it can be seen that simulated pressure losses are smaller than actually measured, however the results shown figure D.9 shown good agreement as the prediction by the model is within the given measured ranges of pressure at each location. The pressure roughness of the data depicted in Figure D.9 shows that the pressures in the sampling region of the data used. The simulated pressure data shown is within the bounds of the pressure roughness of the measure data. The pressure roughness of the three sensors are calculated as 4.11%, 4.85% & 3.04% in the order of increasing L/D. The absolute pressure drop of the flow in the simulated (0.310 [bar]) and the average of the measured pressure (0.38 [bar]). Considering the range of pressure roughness, the pressure losses are significantly small. The simulated pressure of the flow can be has good agreement and within the bounds of the experimentally measured pressures, shown in Figure D.9.

CASE 19

Case 19 the data is sampled between 60 and 80 seconds of the test. This 20 second sampling width for experimental data is chosen from near steady pressure and temperature data. In the sampling window tank pressure is relatively constant, hence the pressure

drop on the injector and the massflow on the catalytic bed is assumed to be constant. This enables to use an average flow rate determined from the data to be used for the model input. From the pressure data it can be seen that tank pressure has a transient from and a relative stable plateau between in the chosen time sampling range, in this region the pressure remains relative constant at 109.98 bar. Similar to the other cases the sample mean is computed for 3 pressure sensor data and used in validation process. Similarly the average massflow is determined for the sampling region, the massflow is derived by the pressure drop over the injector to be an average of 8.18 [gs^{-1}]. Case 16 is simulated with the conditions listed in table D.7.

Parameter	Value	Units
Pressure	102.6	[bar]
Mass flow	8.18	[gs^{-1}]
Inlet temperature	296.15	[K]
HTP concentration	88 %	[w/w]

Table D.7: Case 19 model input conditions

The temperature profile of the flow is shown in Figure D.10, with the simulated model results and experimental results. The saturation conditions of water is met at a L/D of 1.24 with a temperature of 584.9 kelvin. The dry out locations for H_2O is at L/D of 1.635 and H_2O_2 is at 1.806. The experimental data captures the flow temperature in the pre-boiling region and the gas phase, the data shows good alignment with the model results. At a L/D of 0.455 (the pre boiling region) the measure temperature range 303 [K] - 310 [K] the simulation predicts a temperature of 324 [K], the predicted temperature is 14[K] higher. The gas phase flow temperature at L/D 1.818 is measure in the range of 594[K] to 637[K] this corresponds to a reaction progression of 71.1% to 77.8% of the model. This temperature range measured captures the range H_{20} dried out and H_2O_2 dry out. The flow temperature at L/D 1.818 determined by the model is 655[K] corresponding to 79.5% of reaction progress, this is about 18[K] higher than the measured temperatures. In the simulated results 98% of the reaction progression is reached at L/D 2.477 with a temperature of 953 [K]. The third thermocouple further downstream of the catalyst bed located at L/D 3.091 measured temperature range of 905 [K] to 937 [K], this is 8.05% to 4.80% lower than adiabatic temperature. The adiabatic decomposition temperature calculated by the model results with a temperature of 984.2[K] at a L/D of 2.857.

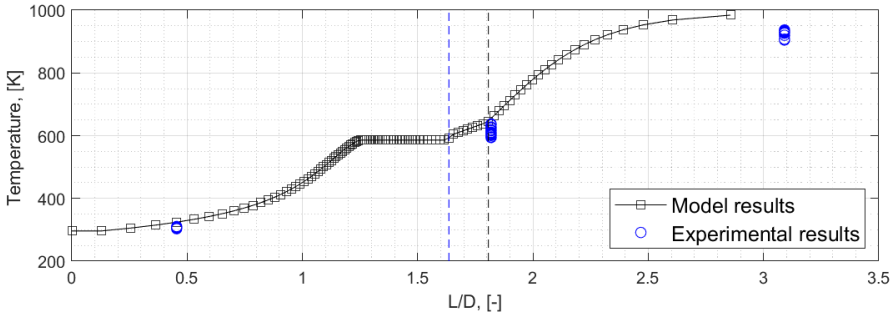

Figure D.10: Simulated flow temperature over the catalyst bed and experimental results (case 19)

The Pressure data in Figure D.8 shows the pressure losses experienced by the flow, the averaged experimental data is depicted at each sensor location. The experimental data shown in the plot is the average value of the pressure measured. Figure D.12 displays the actual pressure range measured and the simulated pressure curve.

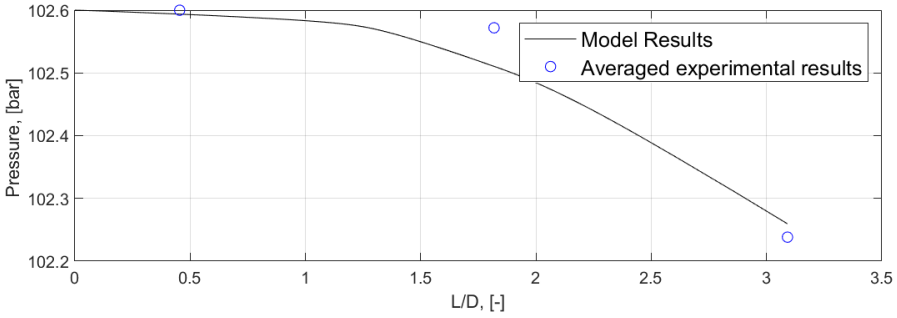

Figure D.11: Pressure distribution over the catalyst bed and averaged experimental results (case 16)

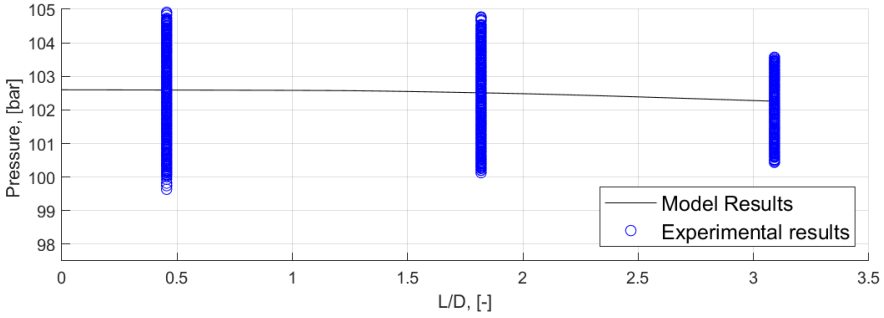

Figure D.12: Pressure distribution over the catalyst bed and experimental results (case 19)

	L/D	Simulated	Measured range	Measured sample Mean
Flow temperature	0.459	324 [K]	303 - 310 [K]	308 [K]
Flow temperature	1.818	655 [K]	594 - 637 [K]	611 [K]
Flow temperature	3.091	-	905 - 937 [K]	929 [K]
Pressure	0.459	102.594	99.6370 - 104.9100 [bar]	102.60 [bar]
Pressure	1.818	102.51	100.1300 - 104.7700 [bar]	102.57 [bar]
Pressure	3.091	102.26	100.440 - 103.570 [bar]	102.24 [bar]

Table D.8: Measured and simulated parameters of Case 19V

The pressure loss over the catalyst bed of the simulation results in 0.34 [bar] and the pressure loss calculated using the average of experimental data results a loss of 0.36 [bar]. The overall pressure loss percentage of simulation is calculated to be 0.33% and the experimental pressure loss percentage is calculated to be 0.35%. The simulated flow pressure and the averaged experimental results are shown in figure D.11. The two results show good agreement as the prediction by the model is within the given measured ranges of pressure at each location. The pressure roughness of the data depicted in Figure D.12 shows that the pressures in the sampling region of the data used. The simulated pressure data shown is within the bounds of the pressure roughness of the measure data. The pressure roughness of the three sensors are calculated as 5.14%, 4.52% & 3.06% in the order of increasing L/D.. Considering the range of pressure roughness, the pressure losses are significantly small. The simulated pressure of the flow can be has good agreement and within the bounds of the experimentally measured pressures, shown in Figure D.12.

CASE 20

Case 20 the data is sampled between 50 and 63 seconds of the test. This 13 second sampling width for experimental data is chosen from near steady pressure and temperature data. In the sampling window tank pressure is relatively constant, hence the pressure drop on the injector and the massflow on the catalytic bed is assumed to be constant. This enables to use an average flow rate determined from the data to be used for the model input. From the pressure data it can be seen that tank pressure has a transient from and a relative stable plateau between in the chosen time sampling range, in this region the pressure remains relative constant at 112 bar. Similar to the other cases the sample mean is computed for 3 pressure sensor data and used in validation process. Similarly the average massflow is determined for the sampling region, the massflow is derived by the pressure drop over the injector to be an average of 8.15 [gs^{-1}]. Case 20 is simulated with the conditions listed in table D.9.

Parameter	Value	Units
Pressure	104.72	[bar]
Mass flow	8.15	[gs^{-1}]
Inlet temperature	296.15	[K]
HTP concentration	88 %	[w/w]

Table D.9: Case 20 model input conditions

The temperature profile of the flow is shown in Figure D.13, with the simulated model results and experimental results. The saturation conditions of water is met at a L/D of 1.24 with a temperature of 587.3 kelvin. The dry out locations for H_2O is at L/D of 1.613 and H_2O_2 is at 1.779. The experimental data captures the flow temperature in the pre-boiling region and the gas phase, the data shows good alignment with the model results. At a L/D of 0.455 the measure temperature range 315 [K] - 333 [K] the simulation predicts a temperature of 325 [K], the predicted temperature is 3[K] higher than the average. The flow temperature at L/D 1.818 is measure in the range of 572[K] to 623[K], this corresponds to a rather large reaction progression of 37% to 75.3% of the model. The temperature is seen to be decline from as the test progress, this maybe associated to a local exhaustion of the catalyst or other local inhibiting phenomena. This temperature range measured captures the H_{20} saturation temperature (587[K]). The flow temperature at L/D 1.818 determined by the model is 663[K] corresponding to 80% of reaction progress, this is about 40[K] higher than the measured temperatures. In this test the temperature at L/D 1.818, the measure temperature declined over the sampling region (leading to a wide range of measured temperature), potentially indicating a local catalyst exhaustion in the performed test. This would cause the sample mean of the measured temperature to be lower than nominal. In the simulated results, 98% of the reaction progression is reached at L/D 2.432 with a temperature of 953 [K]. The third thermocouple further downstream of the catalyst bed located at L/D 3.091 measured temperature range of 939 [K] to 944 [K], this is 4.59% to 4.10% lower than adiabatic temperature. The adiabatic decomposition temperature calculated by the model results with a temperature of 984.2[K] at a L/D of 2.857.

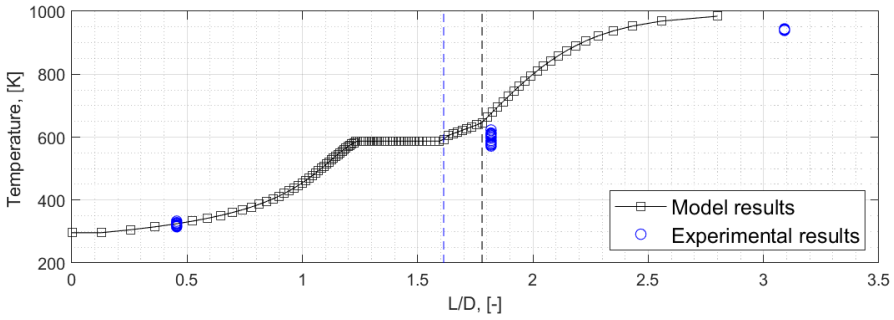

Figure D.13: Simulated flow temperature over the catalyst bed and experimental results (case 20)

The Pressure data in Figure D.14 shows the pressure losses experienced by the flow, the averaged experimental data is depicted at each sensor location. The experimental data shown in the plot is the average value of the pressure measured. Figure D.12 displays the actual pressure range measured and the simulated pressure curve.

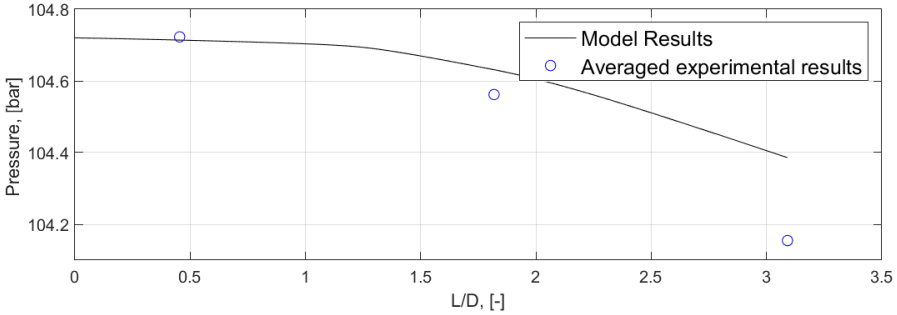

Figure D.14: Pressure distribution over the catalyst bed and averaged experimental results (case 20)

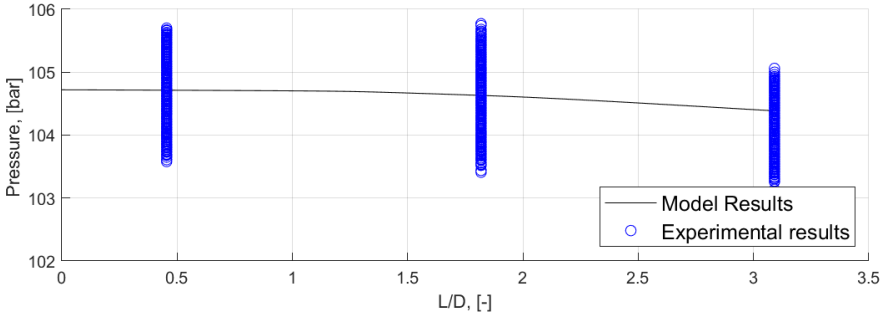

Figure D.15: Pressure distribution over the catalyst bed and experimental results (case 20)

	L/D	Simulated	Measured range	Measured sample Mean
Flow temperature	0.459	325[K]	315 - 333[K]	321 [K]
Flow temperature	1.818	663 [K]	572 - 623 [K]	595 [K]
Flow temperature	3.091	-	939 - 944 [K]	942 [K]
Pressure	0.459	104.712	103.5800 - 105.7000 [bar]	104.72 [bar]
Pressure	1.818	104.63	103.4100 - 105.7700 [bar]	104.56 [bar]
Pressure	3.091	104.39	103.1400 - 105.0600[bar]	104.15 [bar]

Table D.10: Measured and simulated parameters of Case 14V

The pressure loss over the catalyst bed of the simulation results in 0.33 [bar] and the pressure loss calculated using the average of experimental data results a loss of 0.57 [bar]. The

overall pressure loss percentage of simulation is calculated to be 0.32% and the experimental pressure loss percentage is calculated to be 0.55%. The simulated flow pressure and the averaged experimental results are shown in figure D.14. The simulated results are within the measured ranges of pressure at each location. The pressure roughness of the data depicted in Figure D.15 shows that the pressures in the sampling region of the data used. The pressure roughness of the three sensors are calculated as 2.02%, 2.26% & 1.84% in the order of increasing L/D. Even with low pressure roughness as recorded above, the pressure drop is nearly an order in magnitude smaller to be validated accurately. The simulated pressure of the flow can be has good agreement and within the bounds of the experimentally measured pressures, shown in Figure D.15.

APPENDIX: BIBLIOGRAPHY

[1] NIST. "nist chemistry webbook, nist standard reference database ". http://webbook.nist.gov/chemistry/, 2019. Online; accessed 26 Nov 2019.

[2] AK Coker. *Ludwig's applied process design for chemical and petrochemical plants, volume 1, Gulf Professional*. Oxford: UK, 2007.

[3] Duncan Chisholm. A theoretical basis for the lockhart-martinelli correlation for two-phase flow. *International Journal of Heat and Mass Transfer*, 10(12):1767–1778, 1967.

[4] Stanley M Walas. *Chemical Process Equipment Selection and Design*. (USA) Inc. All rights reserved, 1990.

[5] A. Pasini, L. Torre, L. Romeo, A. Cervone, and L. d'Agostino. Reduced-order model for h2o2 catalytic reactor performance analysis. *Journal of propulsion and power*, 26(3):446–453, 2010.

[6] Sungyong An and Sejin Kwon. Catalyst bed sizing of 50 newton hydrogen peroxide monopropellant thruster. In *44th AIAA/ASME/SAE/ASEE Joint Propulsion Conference & Exhibit*, page 5109, 2008.

[7] Sungkwon Jo, Dongwuk Jang, Sungyong An, and Sejin Kwon. Chugging instability of h2o2 monopropellant thrusters with catalyst reactivity and support sizes. *Journal of Propulsion and Power*, 27(4):920–924, 2011.

[8] Sungyong An, Jungkun Jin, Jeongsub Lee, Sungkwon Jo, Daejong Park, and Sejin Kwon. Chugging instability of h2o2 monopropellant thrusters with reactor aspect ratio and pressures. *Journal of Propulsion and Power*, 27(2):422–427, 2011.

[9] Sungyong An, Jeongsub Lee, Rachid Brahmi, Charles Kappenstein, and Sejin Kwon. Comparison of catalyst support between monolith and pellet in hydrogen peroxide thrusters. *Journal of Propulsion and Power*, 26(3):439–445, 2010.

[10] Jeongmoo Huh, Byeonguk Ahn, Youngil Kim, Hyunki Song, Hosung Yoon, Sejin Kwon, et al. Development of a university-based simplified h2o2/pe hybrid sounding rocket at kaist. *International Journal of Aeronautical and Space Sciences*, 2017.

[11] Yongtae Yun, Huh Jeongmoo, Youngil Kim, Shinjae Kang, Seonuk Heo, and Sejin Kwon. Demonstration of 2,500 n-class h2o2/hdpe hybrid rocket for lab-scale sounding rocket. In *2018 Joint Propulsion Conference*, page 4526, 2018.

[12] Byeonguk Ahn, Hongjae Kang, Eunkwang Lee, Yongtae Yun, and Sejin Kwon. Design of multiport grain with hydrogen peroxide hybrid rocket. *Journal of Propulsion and Power*, pages 1–9, 2018.

[13] Seonuk Heo, Sungkwon Jo, Yongtae Yun, and Sejin Kwon. Effect of dual-catalytic bed using two different catalyst sizes for hydrogen peroxide thruster. *Aerospace Science and Technology*, 78:26–32, 2018.

[14] Dongwook Jang, Sejin Kwon, and Sungkwon Jo. Effect of phosphate stabilizers in hydrogen peroxide decomposition on manganese-based catalysts. *Journal of Propulsion and Power*, 31(3):904–911, 2015.

[15] Sungyong An, Sungkwon Jo, Jeonghyun Wee, Hosung Yoon, and Sejin Kwon. Preliminary flight test of hydrogen peroxide retro-propulsion module. *Acta Astronautica*, 67(5-6):605–612, 2010.

[16] Kamil M Sobczak, Pawel Surmacz, Bartosz Bartkowiak, Adam Okninski, Grzegorz P Rarata, Piotr Wolanski, Dominik Kublik, and Ferran Valencia Bel. Test campaign of a green liquid bi-propellant rocket engine using catalytically decomposed 98% hydrogen peroxide as oxidizer. In *53rd AIAA/SAE/ASEE Joint Propulsion Conference*, page 4926, 2017.

[17] Seonuk Heo, Sejin Kwon, and Sangwoo Jung. Development of hydrogen peroxide/kerosene 2,500 n bipropellant thruster for long-term operation by film cooling. In *52nd AIAA/SAE/ASEE Joint Propulsion Conference*, page 5091, 2016.

[18] Dongwook Jang, Youngchul Kwak, and Sejin Kwon. Design and validation of a liquid film-cooled hydrogen peroxide/kerosene bipropellant thruster. *Journal of Propulsion and Power*, 31(2):761–765, 2015.

[19] Hongjae Kang, Dahae Lee, Shinjae Kang, and Sejin Kwon. Effect of h2o2 injection patterns on catalyst bed characteristics. *Acta Astronautica*, 130:75–83, 2017.

[20] Sungyong An, Rachid Brahmi, Charles Kappenstein, and Sejin Kwon. Transient behavior of h2o2 thruster: effect of injector type and ullage volume. *Journal of Propulsion and Power*, 25(6):1357–1360, 2009.

[21] Angelo Pasini, L Torre, L Romeo, A Cervone, and Luca D'Agostino. Performance characterization of pellet catalytic beds for hydrogen peroxide monopropellant rockets. *Journal of Propulsion and Power*, 27(2):428–436, 2011.

[22] David Andrews. Advantages of hydrogen peroxide as a rocket oxidant. *British Interplanetary Society, Journal*, 43:319–328, 1990.

[23] P Morlan, P-K Wu, D Ruttle, R Fuller, A Nejad, and W Anderson. Catalyst development for hydrogen peroxide rocket engines. In *35th Joint Propulsion Conference and Exhibit*, page 2740, 1999.

[24] Paul Kim, Annik Majamaki, Charles Papesh, Darrick Schneider, Matt Thomson, and Vladimir Weinstock. Design and development testing of the tr108-a 30klbf-thrust-class hydrogen peroxide/hydrocarbon pump-fed engine. In *41st AIAA/ASME/SAE/ASEE Joint Propulsion Conference & Exhibit*, page 3566, 2005.

[25] Jack F Runckel, Conrad M Willis, and Leland Blackwood Salters. *Investigation of Catalyst Beds for 98-Percent-Concentration Hydrogen Peroxide*. National Aeronautics and Space Administration, 1963.

[26] Conrad M Willis. *The Effect Of Catalyst-Bed Arrangement On Thrust Buildup And Decay Time For A 90 Percent Hydrogen Peroxide Control Rocket*, volume 516. National Aeronautics and Space Administration, 1960.